

Leveraging human induced pluripotent stem cells for modeling brain diseases

Bas Lendemeijer

Cover shows a co-culture of induced pluripotent stem cell derived astrocytes (green/red) and neurons (cyan)

Printing: Ridderprint B.V., Ridderkerk
Design: Le concepteur

Copyright © 2021 B. Lendemeijer

All rights reserved. No parts of this publication may be reproduced, stored in a retrieval system or transmitted in any form without permission of the author or, when appropriate, the scientific journal in which parts of this thesis have been published.

Leveraging Human Induced Pluripotent Stem Cells For Modeling Brain Diseases

Het gebruik van menselijke geïnduceerde
pluripotente stamcellen om hersenziekten
te modelleren

Thesis

*to obtain the degree of Doctor from the
Erasmus University Rotterdam
by command of the rector magnificus*

Prof. dr. A.L. Bredenoord

and in accordance with the decision of the Doctorate Board.

The public defence shall be held on
Tuesday October 5th, 2021 at 13:00 hours

by

Bas Lendemeijer

born in 's-Hertogenbosch, The Netherlands.

Erasmus University Rotterdam



Doctoral Committee

Promoters:

prof. dr. S.A. Kushner

prof. dr. W.J.G. Hoogendijk

Other members:

prof. dr. E.M. Hol

dr. N. Nadif Kasri

dr. G.M. van Woerden

Co-promotor:

dr. F.M.S. de Vrij

Table of contents

List of abbreviations	7
Preface	9
Scope of this thesis	11
Chapter 1: General introduction	12
Chapter 2: Rapid specification of human pluripotent stem cells to functional astrocytes supporting neural network activity	24
Chapter 3: <i>In vivo</i> preclinical screening of human antisense oligonucleotide therapy for Angelman Syndrome	52
Chapter 4: Candidate CSPG4 mutations and induced pluripotent stem cell modeling implicate oligodendrocyte progenitor cell dysfunction in familial schizophrenia	68
Chapter 5: Replication kinetics, cell tropism and associated immune responses in SARS-CoV-2 and H5N1 virus infected human induced pluripotent stem cell-derived neural models	110
Chapter 6: General discussion	132
Appendices	146
Summary	148
Samenvatting	149
Curriculum Vitae	150
PhD portfolio	151
List of publications	152
Acknowledgements	155
References	156

List of abbreviations

ACE2	Angiotensin-converting enzyme 2
AS	Angelman syndrome
ASO	Antisense oligonucleotide
BoC	Brain on a chip
CNS	Central nervous system
CNV	Copy number variants
CRISPR	Clustered Regularly Interspaced Palindromic Repeats
CSF	Cerebrospinal fluid
CSPG4	Chondroitin Sulfate Proteoglycan 4
Dup15q	15q11-q13 duplication syndrome
ESC	Embryonic stem cell
EB	Embryoid body
GWAS	Genome wide association study
sgRNA	Single-guide RNA
ICV	Intracerebroventricular
iPSC	Induced pluripotent stem cell
MAF	Minor allele frequency
MEA	Multi-electrode array
MEF	Mouse embryonic fibroblast
NB	Network burst
NDD	Neurodevelopmental disorder
NG2	Neural/glial 2
Ngn2	Neurogenin-2
NHEJ	Nonhomologous DNA end joining
NPC	Neural precursor cell
NRP1	Neuropilin-1
OPC	Oligodendrocyte precursor cell
OSVZ	Outer subventricular zone
PWS	Prader-Willi syndrome
SARS-CoV-2	Severe Acute Respiratory Syndrome Coronavirus-2
TMPRSS2	Transmembrane protease serine 2
WTC	Wild-type control
ZIKV	Zika virus

Preface

In 2007, Shinya Yamanaka published his seminal paper¹ describing a technique to create induced pluripotent stem cells (iPSC) from human fibroblasts. The possibility to convert terminally differentiated somatic cells into iPSCs has changed the way human disorders are studied, especially in the field of neuroscience. Primary *ex vivo* human brain tissue is very scarcely available. Generally speaking, post-mortem human brain tissue is more readily available, though still in short supply. This has been a major constraint when studying the human brain, both in a healthy and diseased state. The molecular and functional properties of human neural cells could only be studied using post-mortem or *ex-vivo* material. By using model organisms, much has been learned normal brain development and functioning. Animal models have been established for various psychiatric and neurodevelopmental disorders, and, together with postmortem human studies, have provided some insight into the etiology of these disorders. However, this increase in knowledge has not led to an improvement in treatment options. By utilizing iPSC technology, it is now possible to create patient-derived iPSC lines and study their development and maturation along defined neural cell type lineages. For the first time providing researchers with a potentially unlimited source of human neural cells to study. Early work has shown the potential of this approach for modelling psychiatric and neurodevelopmental disorders, providing novel insights and revealing important differences between mouse and human neural cells. Since the establishment of this technique, iPSC-derived neural cells have evolved from neurons that are able to fire a single action potential to brain organoids that display waves of electrical activity. The rapid evolution of this field continues to entice researches to adopt iPSC technology for their own studies in an attempt to answer fundamental questions on human biology.

Scope of this thesis

IPSC technology can be used to study the development of all cell types of the human body in health and disease, this work describes how this technique can be utilized to study human brain disorders. **Chapter 1** attempts to provide an overview of the current state of the field and how iPSCs can be leveraged to study the functioning of healthy and diseased human brain cells. **Chapter 2** describes a novel protocol to rapidly differentiate human iPSCs into functional astrocytes that have been validated to support neural maturation, a feature for which an adequate iPSC-differentiation protocol has not been reported yet. An *in vivo* model to explore a potential human specific treatment for Angelman syndrome (AS) is presented in **Chapter 3**. AS patient-derived neurons are xenografted into a mouse brain and exposed to human-specific antisense oligonucleotides in order to restore the expression of the disease-causing gene. The potential of using iPSCs to study psychiatric disorders is illustrated in **Chapter 4**, in which we demonstrate that iPSC-derived oligodendrocyte precursor cells from schizophrenia patients carrying a rare *CSPG4*^{A131T} mutation show reduced viability and impaired maturation potential towards myelinating oligodendrocytes. **Chapter 5** describes how different iPSC-derived neural culture models can be used to study the replication kinetics and cell tropism of the novel Severe Acute Respiratory Syndrome Coronavirus-2 to investigate a possible link between infection in the central nervous system and neurological symptoms observed in patients. Finally, **Chapter 6** places the work described in this thesis in a wider context, describes technical considerations when working with iPSCs and possible future directions of the field.

1

General introduction

Studying the human brain

The human mind is a mysterious concept. However, there is broad consensus that it originates from the 170 billion cells in the human brain, divided nearly equally between neuronal and non-neuronal cells². Animal models have provided insight into some features of the brain. For example, we know how location³ or visual information⁴ is processed. Unfortunately, this increase in knowledge hasn't led to improved treatment for patients suffering from psychiatric or neurodevelopmental disorders (NDD). At present, we still do not fully understand why some people develop psychiatric symptoms and others do not. The frustrating reality is that no significant progress in psychiatric drug development has been achieved during the past 50 years^{5,6,7}. For some NDDs, the causal genetic variant has been identified⁸, however for most NDDs the cellular etiology remains elusive. Generally speaking, few risk variants have been identified for psychiatric disorders. Large genome wide association studies (GWAS) have identified genetic variants associated with psychiatric disorders, these common variants contribute only slightly to the chance of developing the disorder^{9,10}. Other studies have identified rare (copy number) variants^{11,12} with a large effect on psychiatric disease risk, however, these variants explain only a small proportion of cases and most include large genomic regions with multiple genes, which can be difficult to study in non-human model systems as a result of genomic divergence. Heterogenous diagnostic criteria make it challenging to establish defined patient groups, and combined with environmental risk factors complicate the identification of genetic variants even further¹³.

Without a clear genetic or environmental causal defect, the classical approach of studying human disorders through animal models is complicated. As an alternative approach, drugs that act on neurotransmitter systems in the brain have been used to mimic psychotic symptoms in animals¹⁴, providing a platform to study specific aspects of psychiatric disorders. Even when the exact genetic cause for a NDD is known, mouse models often fail to fully recapitulate the symptoms observed in patients. Moreover, drugs that effectively rescue phenotypes in an animal model frequently fail to translate to the clinic¹⁵. Most of these models rely on a single affected gene in an inbred genetic background, of which some only show a relevant phenotype in specific mouse strains. In contrast, patients can carry multiple genetic variants¹⁶, and the phenotypic expressivity is an interplay between individual gene vulnerability and total mutational load¹⁷. Besides the genomic differences in animal models and humans, there are also fundamental species differences in neurodevelopment and pathology, especially when compared to the widely used rodent models.

The evolution of the mammalian cortex is considered to be one of the key features that enabled the development of higher cognitive functioning. Neocortical development is well studied in rodents, which share fundamental characteristics with other mammals, including cortical layering and topographic separation into functional domains. During brain development, mice and humans share many features and undergo a similar order

of developmental events¹⁸. Both species have homologous neural cell types and utilize similar cellular or molecular processes, making them an excellent model organism to study some aspects of the brain. Often these findings translate well to the human brain. However, striking differences exist in the development of the rodent and human cortex. The cortex of mice is small and smooth, whereas the human cerebral cortex shows a high amount of folding, known as gyrification¹⁹. This difference originates from the outer subventricular zone (OSVZ). During the second half of human cortical development, the OSVZ is the major neurogenic region²⁰, a region that does not exist in the mouse brain, including the resident stem cells. This subpopulation of neural stem cells in the OSVZ is essential for the development of large and gyrated brains²¹. Increases in cortical volume and surface area have been causally linked to the proliferation and migration of OSVZ cells²². This fundamental difference in cortical development and structure make mice less suitable for studying many complex features of cerebral cortex development, and consequently, higher cognitive functioning.

Besides anatomical differences, conserved cell types between species differ in their expression profile²³ and morphology²⁴. A recent study²³ examining the expression profile of individual cells in the human and mouse middle temporal gyrus found that roughly two-thirds of all genes analyzed had divergent expression in at least one of the cell types identified, with non-neuronal cells showing the highest amount of divergent expression. For example, 14% of genes analyzed in oligodendrocyte precursor cells (OPC) showed a more than 10-fold difference in gene expression when comparing human and mouse brains. The biggest cellular differences between the mouse and human brain can be found in the astrocyte lineage. Human astrocytes are larger and more complex compared to their mouse counterpart²⁴. Interestingly, a specific subtype of interlaminar astrocytes is found exclusively in higher order primates²⁵. These cells have long projections covering all layers of the cortex and are hypothesized to govern neuronal activity across cortical layers. A mutation in a gene highly expressed in interlaminar astrocytes has been associated with major depressive disorder, a uniquely human disorder²⁶.

Induced pluripotent stem cell derived neural models

The molecular, cellular and anatomical differences between mouse and human brains combined with a lack of successful translational studies in the field of neuroscience motivated researchers to look for new models to study human brain development. In an effort to understand the molecular cues involved in the formation of the human brain, early *in vitro* work made use of embryonic stem cells (ESC)²⁷ or primary neural stem cells^{28,29}. These studies were hampered by ethical concerns and the limited availability of primary *ex vivo* brain tissue. In 2007, the lab of Shinya Yamanaka published a pioneering paper¹ describing

a technique to transform terminally differentiated somatic cells into induced pluripotent stem cells (iPSCs). These cells share many of the hallmark features of ESCs, including the potential to differentiate into cells from all three germ layers. Somatic cells, usually blood or skin, are reprogrammed into iPSCs through overexpression of four transcription factors (Oct3/4, Sox2, Klf4 and L-Myc), now referred to as the “Yamanaka factors”. With the establishment of this technique, researchers now had access to a potentially unlimited source of ESC-like cells to study human developmental biology and disease. When expressed in somatic cells the Yamanaka factors induce a cascade of events, remodeling the epigenetic landscape of cells and activating genes essential for inducing and maintaining pluripotency³⁰. Since the establishment of this technique, high variability between iPSC clones due to reprogramming and quality control differences has been an issue³¹, however, the same can be said for ESCs³². A study comparing genetically matched iPSCs and ESCs found that the majority of gene expression and methylation differences could be explained by genetic background and not reprogramming method or cellular origin³³, suggesting that iPSCs are functionally identical to ESCs and a suitable tool to study the development of patient-derived cell types.

With the advent of iPSCs, it became possible to study the molecular and cellular development and maturation of human brain cell lineages in the context of the human genome. Scientists studying neuropsychiatric disorders now had access to human pluripotent stem cells harboring the genome of pathogenic variant carriers. These cell lines could be used to observe and manipulate the development of neural lineage cells cultured *in vitro*. The identification of the pathophysiology of psychiatric and neurodevelopmental disorders has historically been difficult due to a lack of suitable experimental tools and the species differences between humans and experimental animals. iPSC technology presents unique opportunities to address both of these challenges.

Numerous protocols exist to establish neural cultures from iPSCs with different cell type composition and levels of maturity. Some result in a mixed population of different neural cells, while others give rise to a homogenous culture of a single cell type or free-floating 3D brain organoids. Since most are costly and labour intensive, it is crucial to consider the differences between the resulting neural cultures before deciding whether a certain protocol is relevant for answering a particular question or hypothesis. Broadly speaking, differentiation protocols can be divided into two groups – one approach follows a more endogenous physiological differentiation process involving neural precursor cells (NPCs) differentiated from iPSCs through an embryoid body^{34,35} or dual SMAD inhibition³⁶ stage, and subsequently differentiating these NPCs into neural cultures which typically contain a diverse mixture of neural cell types. Alternatively, it is possible to establish a pure culture of a specific neural cell type through forced overexpression of lineage-specific transcription factors in iPSCs or NPCs (**Figure 1.1**). Microglia, the resident immune cells of the central nervous system (CNS), originate from the mesoderm and thus need to be differentiated through an intermediate hematopoietic progenitor stage³⁷.

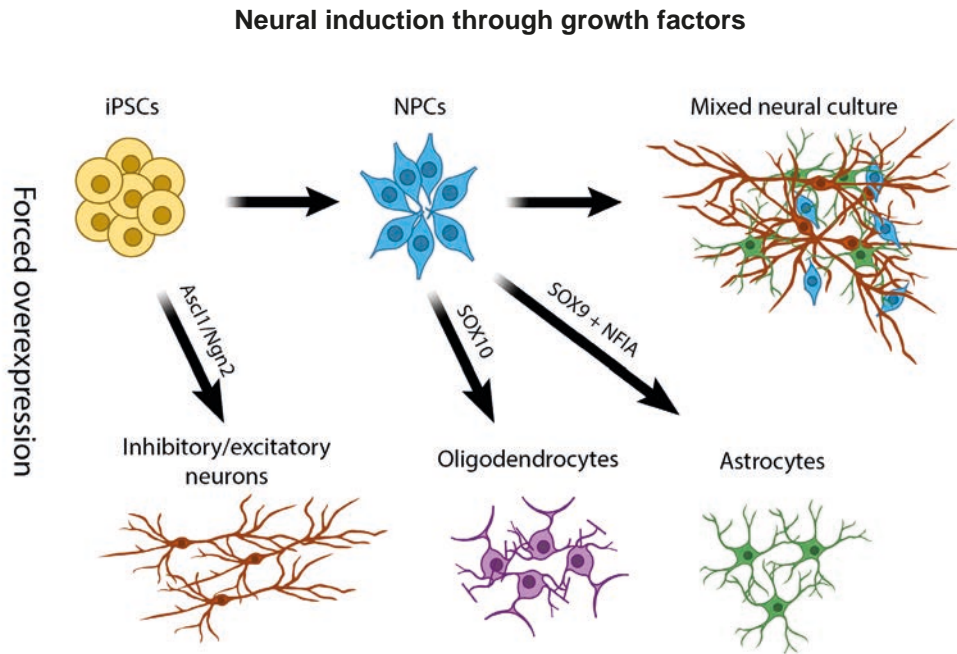


Figure 1.1: A simplified schematic of the approaches to obtain different neural cell types. Neural induction through defined cell culture media follows a more natural approach by mimicking embryonic development, depicted left to right. iPSCs are exposed to growth factors that induce the formation of cells from the ectoderm lineage, followed by NPCs and finally terminally differentiated neural cells. Depending on the desired cell type and brain region the media composition can be adjusted. Alternatively, it is possible to create a relatively homogenous population of the desired cell type through forced overexpression of certain lineage-specific transcription factors, depicted top to bottom.

Mixed neural cultures derived from NPCs have the advantage that glia and neurons develop side-by-side in the same culture in an important reciprocal balance. Neural network protocols are available to generate cultures with different regional specificities, for example, midbrain dopaminergic neurons³⁸ or forebrain glutamatergic neurons³⁵. These mixed cultures give rise to functionally mature neural networks without the need for specialized media or the supplementation of (rodent) astrocytes. Neurons in such a culture typically express the canonical neuronal markers, form functional synapses and show spontaneous network activity. However, differentiation of neural cultures from iPSCs through an NPC stage is time consuming. Protocols typically require 2-3 months before neurons are considered mature and able to fire repetitive action potentials. However, there is a distinct advantage to this approach when studying the effect of certain compounds and/or genetic background at different stages during neurodevelopment. For example, potential phenotypes at the NPC

stage might be masked when using trans-differentiation to direct iPSCs into a single desired cell type³⁹. Molecular and cellular processes that are essential during NPC differentiation are bypassed when directly differentiating iPSCs to mature neural cells.

Trans-differentiation, also known as forward programming, is a rapid method to obtain a homogenous and differentiated culture of a desired cell type from iPSCs. Through forced overexpression of specific transcription factors, iPSCs change their gene expression profile and differentiate towards a specific cell type. Established protocols exist for neurons^{40,41}, myelinating oligodendrocytes⁴² and astrocytes⁴³. With this approach, it is possible to obtain terminally differentiated cells from iPSCs or neural precursors within 3 weeks, significantly reducing the required time investment compared to traditional differentiation through an embryoid body stage. However, to fully mature the cells, a co-culture system is required. Neurons are unable to form electrically active networks in the absence of astrocytes. Oligodendrocytes will not produce myelin in the absence of axons and astrocytes only express a subset of mature markers in the presence of neurons.

Forced overexpression of Neurogenin 2 (Ngn2) in iPSCs gives rise to mature excitatory neurons when grown in a co-culture with primary rat astrocytes⁴⁴. Using multi-electrode arrays, it is possible to record the electrical activity of these Ngn2-neurons, making it possible to efficiently investigate the effect of compounds or genetic variants on the functioning of neurons at a relatively large scale. Ngn2-neurons have also been transplanted into the rodent brain⁴⁰ to study drug effects on human neurons in an *in vivo* environment. Forward programming of iPSCs to oligodendrocytes is achieved by overexpression of SOX10 in OLIG2⁺ glial precursors, giving rise to O4⁺ oligodendrocyte lineage cells that induce myelination when grown in the presence of neurons. These cells can be used to create a highly scalable platform to study the effect of pro-myelinating compounds⁴⁵. A pure astrocyte culture can be obtained through forced overexpression of SOX9 and NFIB in NPCs. This method is faster compared to traditional approaches for deriving astrocytes using growth factors and specialized media, however, these astrocytes have thus far shown limited functionality and have not been capable of supporting the development and maturation of neural networks⁴³. In an effort to address this technical limitation, **Chapter 2** describes a novel protocol to obtain a homogenous culture of iPSC-derived astrocytes that are able to promote the development and maturation of neural networks. With these techniques, scientists now have access to a pure population of all major cell types in the brain, making it possible to precisely titrate the cellular composition of human neural co-cultures.

Developing treatment for human neurodevelopmental disorders

The major advantage of studying human neural cells is the ability to investigate the effect of compounds or genetic variants in a fully human background. As mentioned earlier, some developmental and cellular aspects of the human brain are simply not present in animal models. Moreover, there is a safety aspect involved when advancing to clinical trials. The importance of this was recently highlighted when one volunteer died and four others suffered irreversible brain damage during a phase I first-in-human clinical trial for a fatty acid amide hydrolase inhibitor, BIA 10–2474⁴⁶, a compound developed to alleviate neuropathic pain. Standard safety trials preceding clinical trials showed no adverse side effects in mice, rats or dogs, while macaques exposed to a high dose showed damage in the medulla oblongata. Later it was shown using *in vitro* human models that the compound had off-target effects not detected in rodents⁴⁷. This tragic incident led to renewed consideration of preclinical testing requirements prior to regulatory approval for new drug entities and corresponding clinical trial safety standards^{46,48,49}.

An emerging treatment option for human disorders with a known genetic defect is the modality of antisense oligonucleotides (ASO), which can be designed to potentially reduce or modify translation from specific RNA transcripts^{50,51}. ASOs are short single-stranded DNA sequences that are able to bind RNA transcripts and, depending on the binding-location, induce RNA breakdown or splicing modification. Since the target for these ASOs are human transcripts, the sequence is often non-specific in mouse models. Clinical trials using ASOs have already been completed, for which the most notable successes have been for the treatment of spinal muscular atrophy⁵² and Duchenne muscular dystrophy⁵³. A recent proof-of-concept study demonstrated that ASOs designed to target a patient-specific sequence could be used to treat a rare and fatal NDD⁵⁴, such an approach is unsuitable for traditional clinical trials due to its “N-of-1” design. Despite these early successes, concerns exist about the safety of ASOs⁵⁵. Designing and testing novel ASOs is a time-consuming process, for which the efficacy of ASO sequences and chemical backbones need to be tested and screened for toxicity. Human cell culture models can be used to test the efficacy of an ASO. However, given the potential clinical therapeutic utility of ASOs, an *in vivo* preclinical model would be preferable to exclusively relying upon human cells *in vitro*. Moreover, *in vivo* delivery of ASOs for the treatment of central nervous system diseases is complicated by their very low permeability across the blood-brain-barrier, for which important successes have been achieved with intrathecal delivery of ASOs.

Angelman Syndrome (AS) is potentially suitable for treatment with ASOs. It has a well-established genetic cause through loss-of-function of the maternal copy of the *UBE3A* gene. AS patients suffer from severe neurodevelopmental delay, intellectual disability and motor problems⁵⁶. Multiple mouse models have been created to study AS, which recapitulate the

molecular and cellular phenotypes in neurons and to some extent behavioral phenotypes in similar functional domains as observed in patients⁵⁷. Reinstatement of *Ube3a* early in development can rescue behavioral phenotypes observed in an AS-mouse model⁵⁸. During development, the paternal *UBE3A* allele is silenced in mature neurons due to transcription of a long non-coding *UBE3A*-antisense transcript, which blocks *UBE3A*-sense transcription. Targeted transcriptional blockade of this paternal antisense transcript using Cas9 gene therapy successfully reactivated maternal *UBE3A* expression in cultured human neurons and a mouse model for AS⁵⁹. ASO therapy targeting the *UBE3A*-antisense transcript also restored paternal *UBE3A* expression at an early age, a modality that could potentially be used to treat children even before symptoms arise. A model mimicking a potential therapeutic approach for AS is described in **Chapter 3**, in which AS patient-derived neurons are transplanted into mouse brains, and subsequently treated by intraventricular injection with a human-specific ASO, designed to target the human *UBE3A*-antisense transcript.

Studying schizophrenia using induced pluripotent stem cells

Studying the cellular underpinnings of psychiatric disorders is challenging. Animal models fail to fully recapitulate the phenotype observed in patients. Moreover, they are limited in their ability to reveal fundamental human genetic and cellular processes. Although we have learned much from animal models, there is still a substantial amount that we do not understand about psychiatric disorders⁶⁰. The importance of studying human disorders on a human genetic background is highlighted in **Chapter 4**. A family-based genetic study identified two rare missense mutations in *Chondroitin Sulfate Proteoglycan 4 (CSPG4)*¹¹, one of which is the reference sequence in the mouse genome. *CSPG4* codes for a protein known as neural/glia 2 (NG2), one of the hallmark proteins of OPCs, also known as NG2-cells. OPCs derived from iPSCs generated from carriers of the identified *CSPG4* mutation show aberrant NG2 processing, reduced proliferation and are less likely to mature to myelinating oligodendrocytes.

Schizophrenia is a debilitating disorder affecting roughly 1% of the general population worldwide⁶¹. Symptoms include positive symptoms (i.e., hallucinations or delusions), negative symptoms (i.e., diminished emotional expression or avolition)⁶² and cognitive symptoms. Patients are often profoundly affected and require extensive care from health care professionals. The chronic nature of the disorder creates a significant burden on patients, their families and society. In the Netherlands, the yearly costs associated with all forms of psychiatry-related treatment were roughly 40.000 euros per patient between 2009 and 2012⁶³. Besides the costs associated with care, European studies report that 80-90% of patients with schizophrenia are unemployed⁶⁴. More effective treatments for schizophrenia with diminished side effect burdens would greatly improve the quality of life for patients and potentially reduce the cost for society. Currently, lifelong treatment is required, even

when a patient is not experiencing a psychotic episode⁶⁵. We do not have a satisfactory understanding of the pathophysiology of schizophrenia. Moreover, while we recognize many of the symptoms of schizophrenia, our current diagnostic classification is qualitative and descriptive, rather than quantitative and based on objective laboratory testing.

The dopamine system is believed to be involved in the pathogenesis of schizophrenia, due to the canonical mechanism of all known antipsychotics – antagonism of dopamine D2 receptors^{6,7}. Moreover, recreational drugs, such as amphetamines, act directly or indirectly as dopaminergic agonists and are known to induce psychosis in some individuals⁶⁶. People suffering from schizophrenia seem to be more susceptible to these effects⁶⁷, a finding which has been cited to support the “dopamine hypothesis” of schizophrenia⁶⁸ and sparked decades of research into neurotransmitters and brain regions potentially involved in schizophrenia and psychosis more generally. Broadly speaking, the current working hypothesis of schizophrenia postulates that dopamine is dysregulated in two different systems. Negative symptoms are attributed to hypoactive dopamine receptors in the prefrontal cortex, whereas psychotic symptoms are believed to be caused by hyperactive dopamine receptors in the limbic regions of the brain. Psychosis is thought to arise from dysregulated dopamine signaling in the striatum, leading to the improper attribution of salience to certain external stimuli⁶⁹.

The modulation and organization of neuronal networks is heavily influenced by glia. Oligodendrocytes⁷⁰ and astrocytes^{71–73} govern network activity and integrate neuronal activity in order to ensure proper synchronization between higher order brain functions. Glia have long been considered to play a part in the pathophysiology of schizophrenia^{74–76}, although their exact contribution remains unknown. RNA sequencing and GWAS findings suggest dysregulated expression of genes related to schizophrenia risk in glia.^{77–80} Specifically, these studies indicate changes in expression among schizophrenia patients during brain development, related to white-matter abnormalities, neuroinflammatory pathways and upregulation of astrocyte-specific genes.

Oligodendrocytes ensheath the axons of neurons with a dense lipid-rich membrane called myelin, together also known as the white-matter of the brain. Astrocytes influence the maturation of oligodendrocyte precursor cells into oligodendrocytes and subsequent myelination⁸¹. Proper myelin ensheathment is essential for saltatory conduction of action potentials⁸². Patients typically experience their first psychotic episode during adolescence, a time period that coincides with a peak of myelin and synapse remodeling in the brain⁸³. However, throughout life myelination is a dynamic process, exhibiting plasticity of white-matter microstructure during specific forms of learning^{84,85}. Schizophrenia patients have a reduced number of oligodendrocytes in some brain areas^{83,86} and altered mRNA expression of oligodendrocyte and myelin-related genes^{87,88}. Furthermore, white-matter abnormalities precede the clinical presentation of schizophrenia in some patients, and these abnormalities become more severe over the course of the disorder⁸⁹.

Following the onset of psychosis, schizophrenia patients exhibit reduced white-matter integrity, most notably in the frontoparietal tract⁹⁰. Patients that suffer from disorders affecting white matter integrity, such as leukodystrophies, can experience psychotic episodes⁹¹. These diseases have a diverse underlying etiology, but ultimately lead to defects in myelin development or maintenance. It is hypothesized that improper glial cell progenitor maturation leads to defects in oligodendrocyte and astrocyte functioning, and ultimately schizophrenia by disruption of synaptic connectivity, including alterations in dopaminergic signaling⁹².

Our knowledge of the neurobiology of schizophrenia has improved greatly over the past several years, however this has not led to improved treatment options for patients. There is a gap in our understanding about how the biological alterations we observe in patients give rise to their symptoms. For example, we know that schizophrenia patients have reduced white-matter integrity, but we do not know why this leads to schizophrenia or the underlying cellular mechanisms. Part of this knowledge gap can be explained by phenotypic and genetic heterogeneity among schizophrenia patients. Disease onset, progress, severity and symptoms can vary greatly among patients⁶¹. Early twin studies estimated the heritability of schizophrenia to be around 80%^{93,94}. Despite significant effort in the field, only a small portion of this heritability can be accounted for by genetic variants^{9,95}. iPSC technology aids in circumventing this problem. By creating patient-derived iPSC lines, the total genetic risk of individual patients is preserved, thereby providing a platform to study pathological cellular phenotypes originating from a patient-specific genetic background. However, without a clear hypothesis of the expected cellular phenotype, this approach can be problematic. Studying rare highly penetrant variants provides the ability to formulate hypotheses based on coding variants, which at present is more straightforward than interpretation of GWAS loci of small effect. Through modern genome editing, such as Clustered Regularly Interspaced Palindromic Repeats-associated nuclease Cas9 (CRISPR/Cas9)⁹⁶, iPSC-lines from patients can be used to investigate the biological consequences of these variants compared to reference lines with an identical genetic background.

Neural cell tropism of emerging viruses

iPSC-derived neural cells have been shown to successfully model the kinetics and cell tropism of viruses causing neurological symptoms in humans. In early 2015, zika virus (ZIKV) caused a widespread epidemic in South America. ZIKV is a mosquito-borne virus first identified in 1947. Before this recent widespread outbreak, ZIKV had rarely been associated with human disease⁹⁷. The strain responsible for the 2015 outbreak caused a range of neurological symptoms in patients, most notably, infection during the first trimester of pregnancy appeared to cause microcephaly or miscarriage⁹⁸. iPSC-derived neural cultures showed that the 2015 pathogenic strain of ZIKV predominantly infected NPCs and induced cell death⁹⁹, possibly explaining the observed microcephaly cases.

The current outbreak of the Severe Acute Respiratory Syndrome Coronavirus-2 (SARS-CoV-2) was declared a pandemic on March 11th, 2020. Early reports of patients suffering from COVID-19, the disease caused by SARS-CoV-2, primarily reported symptoms related to the respiratory system¹⁰⁰. Severe COVID-19 patients typically develop pneumonia or acute respiratory distress syndrome, with a current infection fatality rate estimated between 0.53%-0.82%¹⁰¹. However, these estimates are based on a highly heterogeneous patient groups and are likely to change as more data on the true caseload in the population becomes available.

Besides respiratory symptoms, reports from patients suffering from neurological problems during or after COVID-19 have become more frequent¹⁰². Early reports state a high prevalence of anosmia and dysgeusia^{103,104}. This does not seem to be associated with rhinorrhea as observed with rhinoviruses or other coronaviruses. In some cases, more severe neurological pathology have been reported, including cerebrovascular disease¹⁰⁵, encephalitis¹⁰⁶ and acute necrotising encephalopathy¹⁰⁷. Following the immediate onset of COVID-19 symptoms, a proportion of patients experience long-term symptoms, referred to as Long COVID or Post-Acute Sequelae of SARS-CoV-2 Infection¹⁰⁸. Patients experience a wide range of symptoms such as hair loss, muscular weakness or cognitive disturbances. However, the link between neurological symptoms and infection of the CNS is unclear. In the majority of COVID-19 fatalities, SARS-CoV-2 RNA or antigen cannot be detected in the brain¹⁰⁹. In patients actively experiencing neurological symptoms, SARS-CoV-2 is also rarely detected in the cerebrospinal fluid¹¹⁰. Animal models have shown that SARS-CoV-2 can infect and replicate in the olfactory mucosa and induce microglial recruitment, but convincing evidence of productive infection of olfactory neurons has not been found¹¹¹.

Together this suggests that SARS-CoV-2 might be able to enter the CNS through the olfactory nerve, as has been shown for other respiratory viruses¹¹², but is not able to replicate efficiently within the CNS. It remains to be seen if observed neurological symptoms in patients are due to a primary infection in the CNS, secondary due to a heightened local immune response or a combination of both. Part of this question is answered in **Chapter 5**. Different iPSC-derived neural cultures were used to investigate the kinetics, cell tropism and induced immune response of SARS-CoV-2 compared to the neurotropic virus H5N1 influenza A.

Creating better models to study the development and functioning of defined human neural cell types will improve our understanding of their contribution to typical neurodevelopment and neuropsychiatric pathophysiology. Limited availability of primary *ex vivo* brain tissue remains an issue, but currently it is possible to create a potentially limitless amount of iPSC-derived neural cells. Even though protocols have improved during the past decade, the field continues to be limited by technical challenges in directing the differentiation of brain cell lineages that recapitulate the physiology of fully mature *in vivo* cell types. Attempts to improve these models and use them to study human brain disorders are described in this thesis.

2

Rapid specification of human pluripotent stem cells to functional astrocytes supporting neural network activity

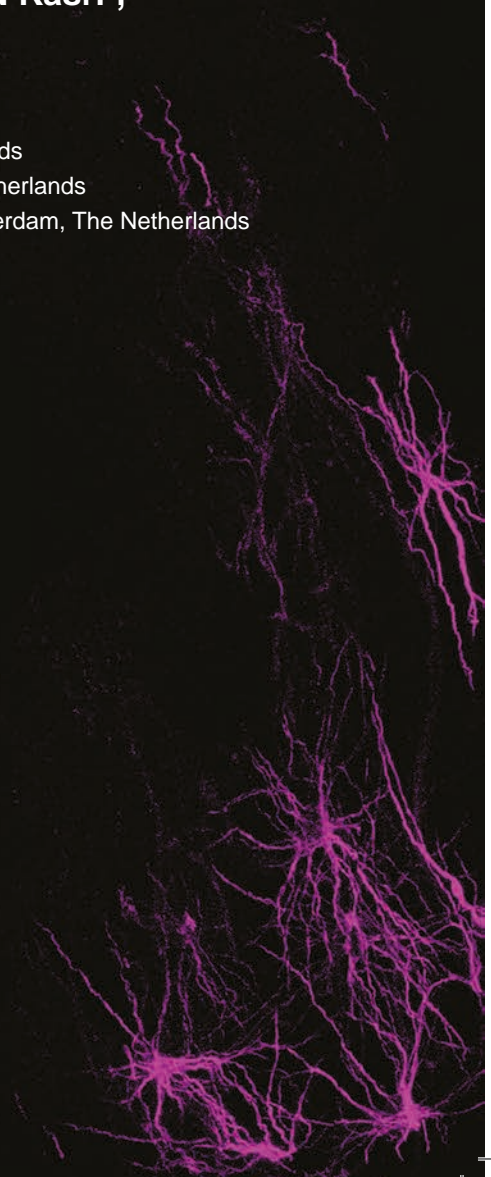
**B Lendemeijer¹, B Mossink², S Hijazi¹, SG Sampedro¹,
G Shpak¹, DE Slump¹, M Unkel¹, MCGN van den Hout³,
WFJ van IJcken³, WJG Hoogendijk¹, NN Kasri²,
FMS de Vrij¹, SA Kushner¹**

¹ Dept of Psychiatry, Erasmus MC, Rotterdam, The Netherlands

² Dept of Human Genetics, Radboudumc, Nijmegen, The Netherlands

³ Dept of Cell Biology, Center for Biomics, Erasmus MC, Rotterdam, The Netherlands

Manuscript in preparation



Abstract

Astrocytes are essential for the formation and maintenance of healthy neural networks by providing neurons with metabolites, influencing synapse formation and network activity. Astrocyte dysfunction has been implicated in a wide range of human brain diseases. However, a limiting factor in studying human astrocyte function and disease-related pathophysiology is availability of the primary tissue. Here we present a protocol to efficiently differentiate human (induced) pluripotent stem cell (iPSC)-derived neural progenitor cells to functional astrocytes in 28 days. Using this protocol, we obtain a pure astrocyte-culture positive for the canonical astrocyte markers, shown by immunofluorescence, flow-cytometry and RNA sequencing. Furthermore, these iPSC-derived astrocytes are able to buffer glutamate and support neuronal network function. Human iPSC-derived astrocytes retain their hominid characteristics when transplanted into a rodent brain. Following the 28-day differentiation protocol, astrocytes were co-cultured together with human iPSC-derived neurons on multi-electrode arrays. Network activity could be observed within 2 days of co-culture, which developed into synchronous network bursts after 6 days. Whole cell patch-clamp recordings showed an increased frequency of postsynaptic currents when comparing human versus rodent astrocyte co-cultures. Furthermore, using image-based quantification we found an increase in the number of synapses in co-cultures with human versus rodent astrocytes. Our protocol enables the establishment of entirely human neural networks, without the need for co-culture with rodent astrocytes, creating opportunities to study cell-type specific effects of human astrocytes on neuronal functioning. In conclusion, we present a novel protocol to obtain functional astrocytes from human pluripotent stem cells, providing a platform for investigating human astrocyte function.

Introduction

Astrocyte complexity is one of the distinguishing features between the human and rodent brain¹¹³. Moreover, increasing evidence has highlighted robust functional differences between rodent and human astrocytes. Human astrocytes propagate calcium waves at higher speed¹¹⁴ and more efficiently promote synaptogenesis¹¹⁵. Generally speaking, astrocytes are crucial for proper brain functioning and are no longer considered to simply provide structural support for neurons¹¹⁶. Astrocytes provide neurons with metabolites¹¹⁷, regulate blood flow¹¹⁸, maintain the blood-brain barrier¹¹⁹, are involved in synapse formation¹²⁰ and influence neuronal network activity⁷³.

Human-induced pluripotent stem cell (iPSC)-derived neural cells provide the opportunity to study the development of the human brain *in vitro*¹²¹. Currently, there are multiple protocols to differentiate human stem cells into neurons^{35,122,123}. Some yield a pure culture of neurons⁴⁰, which require co-culturing with astrocytes to ensure neuronal survival and maturation¹²⁴. Current available options for astrocyte co-culture are rodent astrocytes, the golden-standard in the field, or human stem cell-derived astrocytes. Using rodent astrocytes can be undesirable due to the genomic and functional differences between human and rodent cells. Protocols to differentiate human iPSCs into astrocytes could be improved upon. Some are hampered by contamination of other cell types¹²⁵, others are time-consuming¹²⁶ and most don't promote the electrophysiological maturation of neurons^{124,127–129}. We have previously described protocols to differentiate iPSCs to NPCs, which can survive multiple freeze/thaw cycles, and subsequently mature further into electrically active neural networks³⁵. Here, we present a novel protocol to differentiate stem cell-derived NPCs into functional cortical astrocytes that promote neuronal maturation and network formation, eliminating the need for their rodent counterparts in human neural co-culture systems. Astrocytes differentiated using our protocol express the canonical astrocytic markers, integrate into the rodent brain after transplantation, have the ability to buffer glutamate and promote neuronal maturation. These astrocytes can be used in a wide variety of assays and provide the ability to efficiently establish a pure culture of human astrocytes to study their function and development. Moreover, this protocol can be used to identify the relative contributions of neurons and astrocytes to a human disease-phenotype by creating different co-culture conditions with cells derived from iPSCs with an affected or healthy genetic background.

Results

Differentiation of iPSC-derived NPCs to astrocytes

Forebrain-patterned NPCs were generated from 3 iPSC-lines (iPS1-3) and an ESC-line as previously described³⁵. NPCs were thawed and grown in NPC medium, passaged 1:4 using accutase (Sigma, A6964) when the cells reached 80-90% confluent and grown in astrocyte medium. Four weeks after starting the astrocyte differentiation protocol a relatively homogenous and pure population of astrocytes was obtained (**Figure 2.1A**). Astrocytes were positive for the canonical markers GFAP, S100B, SOX9, CD44, and negative for NPC markers such as PAX6, and neuronal markers such as β -tubulin, NeuN and MAP2. A subset of astrocytes was found to be positive for the astrocyte marker ALDH1L1 (**Figure 2.1B-E**). Across multiple stem cell lines, flow cytometry based on GFAP, CD44 and SOX9 demonstrated that >92% of the cultures consisted of astrocytes (**Figure 2.1F-G**), similar to the purity of primary rat astrocyte cultures (**Supplementary Figure 2.2**).

RNA sequencing confirms astrocyte cell identity and high reproducibility

To characterize the transcriptome of the human PSC-derived astrocytes, we performed 3 independent differentiations of each of 4 pluripotent stem cell lines (3 iPSC and 1 ESC). Principle component analysis shows that replicates cluster together and astrocyte samples cluster away from NPC samples (**Figure 2.2A**). Interestingly, commercial lines, iPS1 and ES, cluster away from in-house lines, iPS2 and iPS3, a difference that can already be observed at the NPC-stage. Hierarchical clustering on established cell-type specific markers confirmed the separation between NPC and astrocyte samples, and the batch-to-batch reproducibility. Canonical astrocyte genes, e.g. GFAP, AQP4, and S100B, are robustly upregulated in astrocyte samples compared to NPC samples, while neuronal genes, e.g. MAP2, TUBB3 and DCX are downregulated (**Figure 2.2B**). A recent paper¹³⁰ showed distinct expression profiles of white matter, deep- and upper-layer cortical astrocytes. When looking at genes with similar expression profiles in rodent and human astrocytes, CHRD1, DDIT4L, EOGT, PAMR1 and IGFBP2, astrocytes derived using our protocol most closely resemble upper-layer astrocytes (**Figure 2.2B**). Shared up- and downregulated genes (721 down- and 1874 upregulated genes (adjusted $p < 0.01$, log2 fold change > 1)) (**Figure 2.2C**) were used to perform a Gene Ontology (GO) analysis. The top 20 enriched GO-terms are involved in extracellular matrix organization, antigen presentation, angiogenesis and short-term synaptic plasticity (**Table 2.3**), similar to observations made in other work studying iPSC-derived astrocytes.^{131, 132}

← **Figure 2.6** Multi-electrode array (MEA) recordings of (co-)cultures consisting of iCell Glutaneurons with or without astrocyte. **(A)** Experimental setup iCell Glutaneuron co-cultures, NPCs (blue) are first differentiated to astrocytes (green) and plated together with neurons (red) in a co-culture. **(B)** Representative raster plots of spontaneous electrophysiological activity of individual wells in different co-culture conditions, with human astrocytes (black) from different batches, rodent astrocytes (blue) or neurons alone (yellow). **(C)** Mean firing frequency over time. **(D), (E)** Activity of all electrodes over multiple experiments presented in frequency bins 10 **(D)** and 20 **(E)** days after plating. **(F), (G), (H)** individual bursts per minute **(F)**, duration **(G)** and frequency **(H)**. **(I), (J), (K)** Network bursts per minute **(I)** duration **(J)** are similar between rodent and human astrocyte co-cultures, firing frequency **(K)** is increased in human astrocyte co-cultures. **(L)** Experimental setup NGN2-neuron co-culture, iPSCs are plated together with astrocytes in a co-culture and NGN2 expression is forced in iPSCs using doxycycline to differentiate them to neurons. **(M), (N), (O)** Analysis of Ngn2-neurons co-cultures, mean firing frequency **(M)** and network burst rate **(N)** is increased in human astrocyte co-cultures, network burst duration is similar in both conditions **(O)**.

Discussion

Astrocytes are essential for neuronal network development, survival and electrophysiological maturation^{136,137,138}. Accordingly, there is a widely acknowledged pressing need for reproducible protocols to establish pure iPSC-derived astrocyte cultures, demonstrated by the many protocols that currently exist^{124–128,132}. Two recent studies^{139,140} show that supplementing additional iPSC-derived astrocytes to a mixed neuronal culture improves the electrophysiological properties of neurons. Protocols to differentiate iPSCs to a homogenous population of astrocytes that support neuronal maturation can be time-consuming and challenging to create. The protocol presented here shows that we are able to quickly and efficiently differentiate human (induced) pluripotent stem cells into a homogenous population of astrocytes. By making use of an intermediate stage of NPCs that can expanded and survive cryopreservation, astrocyte-cultures can rapidly be established while maintaining the genomic integrity of the iPSC-line. These astrocyte-cultures are of high purity and functionality. Astrocytes buffer glutamate, retain their hominid characteristics in a rodent brain and support the maturation and network formation of neurons. Interestingly, we observed a change in *in vitro* morphology of astrocytes becoming larger and more complex when grown in a co-culture with neurons combined with an increase in GLT-1 expression (**Supplementary Figure 2.4**). Suggesting a bidirectional interaction between neurons and astrocytes in co-culture conditions¹⁴¹.

One of the major characteristics of astrocytes is their ability to buffer glutamate from the synaptic cleft¹⁴² and consequently ensure proper signalling in the tripartite synapse. We detected GLT-1 expression in our RNA sequencing data and show GLT-1 staining in co-cultured astrocytes. Functionally, we visualised glutamate uptake using an intracellular

fluorescent probe¹⁴³ expressed in astrocytes. In a co-culture with iPSC-derived neurons we observed waves of fluorescence intensity corresponding to the timing of network bursts recorded during MEA experiments, suggesting that glutamate is indeed released by neurons and taken up by astrocytes.

A widely adopted protocol⁴⁰ that quickly yields a pure population of neurons requires the addition of primary rodent astrocytes for the neurons to mature enough to perform electrophysiological measurements¹⁴⁴. Here, we demonstrate that with our protocol it becomes possible to create a fully functional human iPSC-derived neural co-culture system. This provides the opportunity to precisely control the culture composition of a fully human population of neural cells, making it possible to study the effects of cell-type specific genotypes or targeted genetic manipulations of co-cultured astrocytes and/or neurons. The independent replication of the implementation of the human iPSC-derived astrocyte protocol and support for neuronal network maturation is encouraging for the robustness of the method and its broad adoption. Even though astrocytes derived using our protocol were used in combination with different human iPSC-derived neurons and in a different experimental setup, similar results were obtained; neurons grown with human astrocytes are able to fire at a higher frequency.

iPSC-technology has provided the opportunity to study the development of human brain cells. This is especially valuable for astrocytes, arguably the most highly dimorphic cell types between the human and rodent brain¹¹³. Compared to their rodent counterpart, human astrocytes are larger and have a more complex morphology. A specific subtype of astrocyte, interlaminar astrocytes, are found exclusively in higher order primates¹⁴⁵. It has been established that primary human astrocytes also functionally show differences with rodent astrocytes^{114, 115}. We demonstrate that astrocytes differentiated using our protocol maintain these hominid characteristics. When transplanted into a rodent brain, they are larger and more complex compared to neighbouring mouse astrocytes. Functionally, our experiments show that iPSC-derived neurons are more active and receive more synaptic input in co-culture with human versus rodent astrocytes. Taken together, our findings emphasize the need for functional human astrocytes to model human brain development. The protocol presented here provides an opportunity to efficiently derive functional astrocytes from human pluripotent stem cells that compare favourably to primary rodent astrocytes.

RNA sequencing

Total RNA was isolated from NPCs and their derived astrocytes (4 lines, n=3 per cell type) using a RNeasy mini kit (Qiagen, 74104). RNA samples were prepped using TruSeq® Stranded mRNA Library kit (Illumina, 20020594). The resulting DNA libraries were sequenced according to the Illumina TruSeq Rapid v2 protocol on an Illumina HiSeq2500 sequencer. 50 bp reads were generated, trimmed and mapped against GRCh38 using HiSat2 (version 2.1.0), gene expression values were called using htseq-count (version 0.9.1). Sequencing resulted in at least 24.3M reads per sample, with at least 18.8M counts and 23.9-25.2k expressed genes. Analysis was performed using a custom R script.

Astrocyte engraftment in neonatal Rag2^{-/-} mice

All mouse experiments were approved by the local animal welfare committee. IPSC-derived astrocyte development was investigated *in vivo* by transplanting astrocytes into immunodeficient neonatal (P1) Rag2^{-/-} BALB/c mice. Pups underwent cryoanesthesia and 5-10 x 10⁴ astrocytes were delivered in a 1 µl PBS-drop via a 1 mm-diameter pulled glass pipette into five different sites – posterior and anterior anlagen of the corpus callosum bilaterally and in the cerebellar peduncle dorsally¹⁴⁷. Mice were sacrificed at 4 and 8 weeks of age by transcardiac perfusion with saline followed by 4% PFA. Brains were removed, left in 4% PFA for 2 hours at room temperature, transferred to a 10% phosphate buffer (PB 0.1 M, pH 7.3) and stored overnight at 4°C. Brains were embedded in 12% gelatin/10% sucrose blocks, fixation was performed for 2 hours at room temperature in a 10% pFA/30% sucrose solution. Embedded brains were stored, at least overnight, at 4°C before being sliced into 40 µm slices on a freezing microtome (Leica, Wetzlar, Germany; SM 2000 R). Brain sections were pre-incubated with a blocking buffer (0.5% Triton X-100 (Sigma, T8787) and 10% normal horse serum (NHS; ThermoFisher, 16050122) in PBS) for 1 hr at room temperature. Primary antibody incubation was done for 48 hours at 4°C. Secondary antibody incubation was done for 2 hours at room temperature. Both primary and secondary antibody incubation were performed in a staining buffer (2% NHS and 0.5% Triton X-100 in PBS). Samples were mounted using Mowiol 4-88 (Sigma-Aldrich, 81381) and imaged using a Zeiss LSM 800 confocal microscope (Oberkochen, Germany).

Human brain immunocytochemistry

Middle frontal gyrus tissue blocks were postfixed for 7 days in 4% paraformaldehyde (0.1 M phosphate buffer, pH 7.3) at 4°C. Tissue was subsequently transferred to 10% sucrose (0.1 M phosphate buffer, pH 7.3) and stored overnight at 4°C. Embedding was performed in 12% gelatin/10% sucrose, with fixation in 10% paraformaldehyde/30% sucrose solution for 4 h at room temperature and overnight immersion in 30% sucrose at 4°C. Serial 40 µm sections were collected along the rostrocaudal axis using a freezing microtome (Leica, Wetzlar, Germany; SM 2000 R) and stored at -20 °C in a solution containing 37.5% ethylene

glycol (Avantor, Central Valley, PA, USA, 9300), 37.5% glycerol (VWR Chemicals, Radnor, PA, USA, 24386.298) and 25% 0.1 M phosphate buffer. Free-floating sections were washed thoroughly with PBS before being incubated in sodium citrate (10mM) at 80 °C for 45 min and rinsed with PBS. Sections were pre-incubated with a blocking PBS buffer containing 1% Triton X-100 and 5% bovine serum albumin for 1 h at room temperature.

Primary antibody labeling was performed in PBS buffer containing 1% Triton X-100 and 1% BSA for 72 h at 4 °C. Following primary antibody labeling, sections were washed with PBS and then incubated with corresponding Alexa-conjugated secondary antibodies and cyanine dyes (1:400, Braunschweig Chemicals, Amsterdam, The Netherlands) in PBS buffer containing 1% Triton X-100, 1% BSA for 4 h at room temperature. Nuclear staining was performed using DAPI (1:10000, Thermo Fisher Scientific, Waltham, MA, USA). Images were acquired using a Zeiss LSM 800 confocal microscope (Carl Zeiss, Oberkochen, Germany).

Astrocyte size quantification

Astrocytes were identified using a combination of antibodies (**Table 2.1**): (human) GFAP, STEM121 and human nucleus. Maximum projection images of 40 µm brain slices were used to determine cell size by drawing circles around typical protoplasmic astrocytes and calculating maximum diameter with Fiji (NIH ImageJ). Neighboring mouse astrocytes and transplanted human ipsc-derived astrocytes were analyzed in mice of different ages (4 - 40 weeks). Human astrocytes were analyzed in postmortem brain tissue (age 61-81).

Glutamate uptake

We set out to evaluate the ability of our stem cell-derived astrocyte to buffer glutamate by infecting astrocytes with AAV9.GFAP.iGluSnFr.WPRE.SV40 (Penn Vector, AV-9-PV2914, 1×10^{10} vg/individual 24-wells). Two weeks after infection, astrocytes were exposed to 50 µM glutamate (Sigma-Aldrich, G1251) in the culture medium, or co-cultured with iCell Glutaneurons (Cellular Dynamics, R1034) to measure their ability to take up glutamate. Fluorescence imaging was performed at 37 °C/5% CO₂ using a LSM800 confocal microscope (Zeiss) equipped with a live-imaging setup. Medium containing 50 µM glutamate was washed in after baseline recording. Co-cultures were recorded in iCell medium without addition of Glutamate. Fluorescence intensity was analyzed using Fiji (NIH ImageJ). $\Delta F/F$ was calculated for individual cells by manually drawing ROIs around fluorescent somata.

Co-culture with iCell Glutaneurons

In order to investigate to what extent astrocytes derived using our protocol are able to support neuronal network formation and maturation, human stem cell-derived astrocytes or rat astrocytes (Sciencell, SCCR1800) were grown as a co-culture with iCell Glutaneurons (Cellular Dynamics,

R1034). Astrocytes and neurons were plated in a 1:2 ratio on a 24-well Multiwell Electrode Array (MEA) plate (Multichannel Systems, 24W300-30G-288) or on coverslips, coated with Poly-L-Ornithine (Sigma-Aldrich, P4957) and 50 $\mu\text{g/ml}$ laminin (Sigma-Aldrich, L2020). Co-cultures were maintained in iCell medium (**Table 2.1**) 37°C/5%CO₂ for up to 4 weeks.

Co-culture with Ngn2-neurons

iPSCs were directly differentiated into excitatory cortical layer 2/3 neurons by forcibly overexpressing the neuronal determinant Neurogenin 2 (Ngn2)^{40,148}. To support neuronal maturation, iPSC-derived astrocytes or freshly prepared rat astrocytes were added to the culture in a 1:1 ratio. At day 3, the medium was changed to Ngn2-medium (**Table 2.2**). Cytosine b-D-arabinofuranoside (Ara-C) (2 μM ; Sigma, C1768) was added once to remove proliferating cells from the culture and ensure long-term recordings of the cultures. From day 6 onwards, half of the medium was refreshed three times per week. Medium was additionally supplemented with 2.5% FBS (Sigma, F2442) to support astrocyte viability from day 10 onwards. Neuronal cultures were kept at 37°C/5%CO₂ throughout the entire differentiation process.

MEA-recordings

Spontaneous electrophysiological activity was recorded on a multiwell-MEA-system (Multichannel Systems). Plates were kept at 37°C and maintained in an air mixture containing 5% CO₂. Plates were equilibrated to the chamber for 10 minutes and recorded for an additional 10 minutes. The signal was sampled at 10 kHz, filtered with a high-pass filter (i.e., Butterworth, 100 Hz cutoff frequency) and the noise threshold was set at ± 4.5 standard deviations. Recordings were analysed off-line using Multiwell-Analyzer (Multichannel Systems) and SPYCODE¹⁴⁹.

Electrophysiological recordings

Co-cultures were grown for 1 or 2 weeks, after which culture slides were transferred to the recording chamber and whole-cell patch-clamp recordings were performed as previously described³⁵. Briefly, cultures were equilibrated to artificial cerebrospinal fluid (ACSF). In the recording chamber, slides were continuously perfused with ACSF at 1.5-2 mL/min, saturated with 95% O₂/5% CO₂ and maintained at 20-22°C. Recordings were performed with borosilicate glass recording micropipettes (3-6 M Ω). Data were acquired at 10 kHz using an Axon Multiclamp 700B amplifier (Molecular Devices), filtered at 3 kHz, and analyzed using pClamp 10.1 (Molecular Devices). Current-clamp recordings were performed at a holding potential of -70 mV. Intrinsic membrane properties were analysed using a series of hyperpolarizing and depolarizing square wave currents (500 msec duration, 1 sec interstimulus interval) in 5 pA steps, ranging from -30 to +30 pA. Data analysis was performed using a custom-designed script in Igor Pro-8.0 (Wavemetrics). Input resistance was calculated from the first two hyperpolarizing steps. Active properties were extracted

from the first depolarizing step resulting in AP firing. AP threshold was defined by the moment at which the second derivative of the voltage exceeded the baseline. AP amplitude was measured from threshold. Neurons were categorized as “firing” if they were capable of firing 3 or more mature APs without significant accommodation during a depolarizing current step. Voltage-clamp recordings were performed at a holding potential of -80 mV. Synaptic events were detected using Mini Analysis Program (Synaptosoft, Decatur, GA). Bursting activity was defined as a period longer than 5 sec with a frequency of more than 20Hz, followed by a return to baseline.

Synapse quantification

To quantify synapse formation, (co-)cultures were imaged 1 and 2 weeks after plating in different compositions: iCell Glutaneurons alone (1 week old, n=14), co-cultured with rodent astrocytes (1 week old, n=14, 2 weeks old, n=23) or co-cultured with iPSC-derived astrocytes (1 week old, n=35, 2 weeks old, n=24). Cultures were stained for synapsin, PSD95 and MAP2 (**Table 2.2**). Multiple (3-5) images were taken per coverslip. Synapses were counted as puncta with colocalization of PSD95, synapsin and MAP2.

Statistical analysis

RNA sequencing data was analyzed using the Fisher's exact test Bonferroni corrected for multiple testing where necessary. For functional studies, statistical comparisons were performed using a two-tailed t-test or analysis of variance (ANOVA), as indicated. Data are expressed as mean \pm S.E.M., unless otherwise specified. The threshold for significance was set at $P < 0.05$ for all statistical comparisons.

Name	Reagents	Manufacturer, catalogue number
hES Medium	Advanced DMEM/F12 20% Knock-out serum replacement 1% MEM-NEAA 7 nl/ml β -mercaptoethanol 1% L-Glutamine 1% Penicillin-Streptomycin 10 ng/ml basic Fibroblast Growth Factor	ThermoFisher Scientific, 1634010 ThermoFisher Scientific, 10828028 ThermoFisher Scientific, 11140035 Sigma-Aldrich, M7522 ThermoFisher Scientific, 25030024 ThermoFisher Scientific, 15140122 Merck, GF003AF
Neural Induction Medium	Advanced DMEM/F12 1% N-2 Supplement 2 μ g/ml Heparin 1% Penicillin-Streptomycin	ThermoFisher Scientific, 1634010 ThermoFisher Scientific, 17502048 Sigma-Aldrich, H3149 ThermoFisher Scientific, 15140122
NPC Medium	Advanced DMEM/F12 1% N-2 Supplement 2% B-27 minus RA Supplement 1 μ g/ml Laminin 1% Penicillin-Streptomycin 20 ng/ml basic Fibroblast Growth Factor	ThermoFisher Scientific, 1634010 ThermoFisher Scientific, 17502048 ThermoFisher Scientific, 12587010 Sigma-Aldrich, L2020 ThermoFisher Scientific, 15140122 Merck, GF003AF
Astrocyte Medium	Advanced DMEM/F12 1% N-2 Supplement 2% B-27 minus RA Supplement 1 μ g/ml Laminin 1% Penicillin-Streptomycin 10 ng/ml Bone morphogenetic protein 4 10 ng/ml Leukemia Inhibitory Factor	ThermoFisher Scientific, 1634010 ThermoFisher Scientific, 17502048 ThermoFisher Scientific, 12587010 Sigma-Aldrich, L2020 ThermoFisher Scientific, 15140122 BioVision, 4578 PreproTech, 300-05
iCell Medium	BrainPhys Neuronal Medium 1% N-2 Supplement 1% iCell Nervous System Supplement 2% iCell Neural Supplement B 1 μ g/ml Laminin 1% Penicillin-Streptomycin	Stemcell Technologies, 05790 ThermoFisher Scientific, 17502048 Cellular Dynamics, M1031 Cellular Dynamics, M1029 Sigma-Aldrich, L2020 ThermoFisher Scientific, 15140122
Ngn2 Medium	Neurobasal Medium 2% B-27 minus RA Supplement 1% Glutamax 10 ng/ml NT3 10 ng/ml BDNF 0.1 μ g/ml primocin	ThermoFisher Scientific, 21103049 ThermoFisher Scientific, 12587012 ThermoFisher Scientific, 35050061 PeproTech, 450-03 ProSpec, CYT 207 Invivogen, ant-pm-1

Table 2.1 Overview of media and reagents used.

Antibody	Dilution	Manufacturer, catalogue number
ALDH1L1	1:100	Abnova, H00010840-M01
Beta III Tubulin	1:100	Millipore, AB9354
CD15 V450	1:100	BD Bioscience, 561584
CD24 PE-Cy7	1:250	BD Bioscience, 561646
CD44 FITC	1:100	BD Bioscience, 560977
CD184 APC	1:250	BD Bioscience, 560936
CD271 PE	1:500	BD Bioscience, 560927
CD44	1:200	Sigma-Aldrich, SAB4700188
Human GFAP	1:200	Biolegend, 837201
GFAP	1:200	Millipore, AB5804
GFP	1:200	Abcam, ab13970
GLT1	1:100	Sigma-Aldrich, AB1783
Human Nuclei	1:500	Millipore, MAB1281
MAP2	1:200	Synaptic Systems, 188004
PSD-95	1:100	ThermoFisher Scientific, MA1-046
SOX9	1:500	R&D Systems, AF3075
STEM121	1:500	Takara Bio, Y40410
Synapsin	1:200	Synaptic Systems, 106 103
S100B	1:200	Sigma-Aldrich, S2532

Table 2.2 List of antibodies used.

3

***In vivo* preclinical screening of human antisense oligonucleotide therapy for Angelman Syndrome**

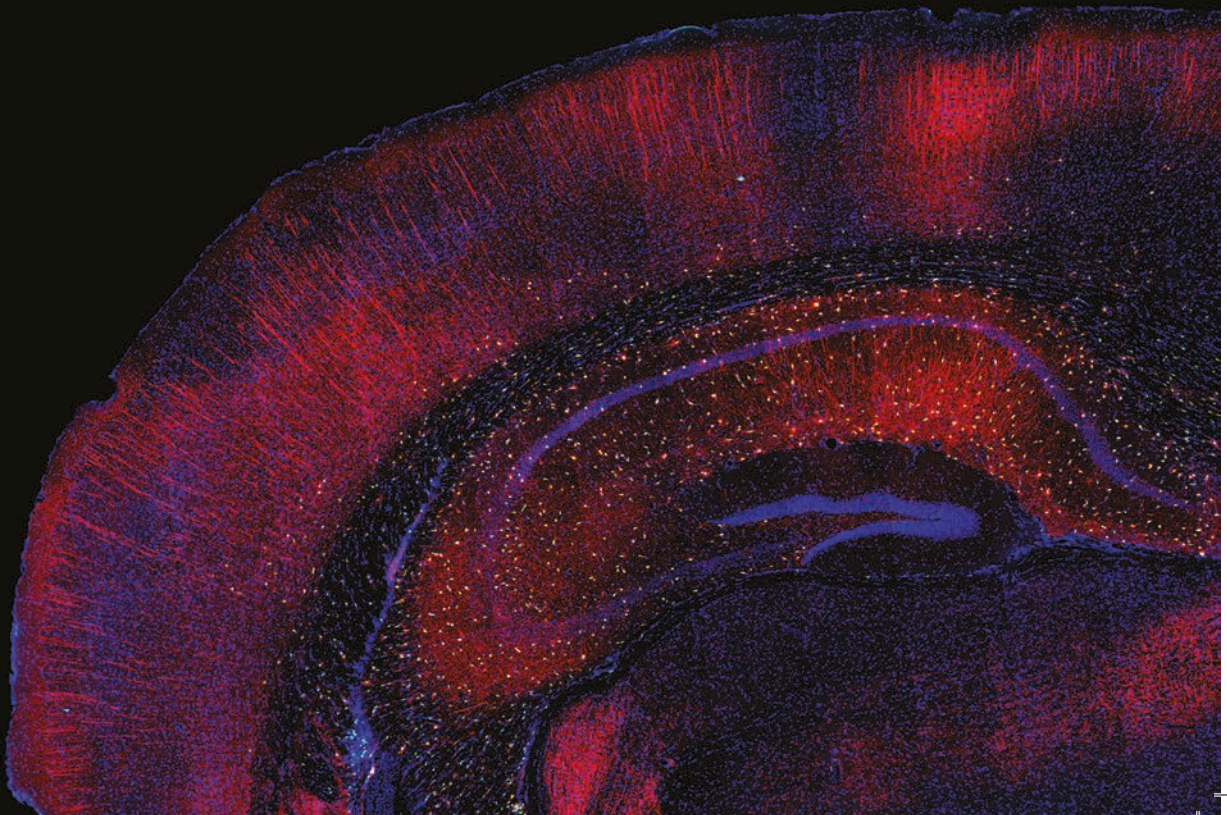
**B Lendemeijer^{1#}, M Buurma^{1#}, H Smeenk¹, DE Slump¹,
C Milazzo², E Mientjes², WJG Hoogendijk¹, Y Elgersma²,
FMS de Vrij^{#1}, SA Kushner^{#1}**

¹ Dept of Psychiatry, Erasmus MC, Rotterdam, Netherlands

² Dept of Clinical Genetics, Erasmus MC, Rotterdam, Netherlands

[#] Authors contributed equally

Manuscript in preparation



Abstract

Angelman Syndrome (AS) is a severe neurodevelopmental disorder (NDD) affecting roughly 1:15.000 children. The genetic cause for AS has been identified – loss-of-function of the maternally expressed copy of *UBE3A*. The paternal copy of *UBE3A* is silenced in neurons by a long non-coding RNA transcript, known as *UBE3A-ATS*. In an AS mouse model, it has been shown that *Ube3a* reactivation at an early age can rescue pathogenic phenotypes. Antisense oligonucleotides (ASO) are a potential treatment option for AS patients and other disorders with a clear single-protein defect. ASOs influence protein expression by binding RNA transcripts, resulting in reduced protein expression or alternative splicing. Due to their mechanism of action, ASOs are sequence-specific. Therefore, therapeutic ASOs often need to be designed based on the human genome and their effectiveness tested on human cells. By using an ASO targeting the human *UBE3A-ATS* transcript, we are able to restore *UBE3A* expression in induced pluripotent stem cell (iPSC)-derived AS neurons *in vitro*. In order to test the feasibility of this ASO in the clinic, we designed a platform to evaluate the effectiveness of this ASO *in vivo*. By transplanting iPSC-derived AS neurons into the brain of neonatal immunodeficient mice and a subsequent intracerebroventricular injection with an *UBE3A-ATS* ASO, we were able to restore *UBE3A* expression in human neurons *in vivo*. Using our model we demonstrate the effectiveness of delivery of an *UBE3A-ATS* ASO to the cerebrospinal fluid as a potential therapeutic to treat AS patients.

Introduction

Angelman Syndrome (AS) is a severe neurodevelopmental disorder (NDD) affecting roughly 1:15.000 children. Patients are diagnosed with developmental delay, movement disorders, inappropriate frequent laughter, speech impairments, and frequently severe intractable seizures¹⁵⁰. The genetic cause for AS has been identified – loss-of-function of the maternally expressed copy of *UBE3A* leading to absence of functional HECT E3 ubiquitin ligase UBE3A in mature neurons¹⁵¹. Generally speaking, E3 ubiquitin ligases tag proteins with ubiquitin, marking them for degradation, altered localization or impairing their functioning. *Ube3a* reactivation at an early age can rescue phenotypes in an AS mouse model⁵⁸. Currently, it is unclear why a loss of UBE3A in neurons leads to the symptoms observed in patients. It has been established that *Ube3a*-mutant mice show synaptic deficits¹⁵², however, a disease-related pathway has not yet been identified.

The genomic region that contains *UBE3A*, 15q11-q13, is implicated in two other NDDs, Prader-Willi syndrome (PWS) and 15q11-q13 duplication syndrome (Dup15q). Expression in this region is heavily influenced by the methylation status of the maternal and paternal alleles¹⁵³. Several genes from this region are imprinted, with expression exclusively from a specific parental allele. In neurons, *UBE3A* is only expressed from the maternal allele. On the maternal allele, CpG islands in the PWS imprinting center are methylated, preventing expression of *SNURF-SNRPN*. On the paternal allele, these are unmethylated, allowing expression of a long non-coding antisense RNA transcript (*UBE3A-ATS*) that prevents expression of paternal *UBE3A* in mature neurons¹⁵³. Large deletions in this region on the paternal allele result in PWS, while Dup15q often is the result of duplications of this entire region, although a case has been reported in which only the *UBE3A* gene was duplicated¹⁵⁴. Even though the same genomic region is implicated in all of these disorders, AS, PWS and Dup15q patients present with distinct somatic, neurodevelopmental and psychiatric symptoms. Restoring UBE3A levels without interfering with paternally expressed genes could potentially rescue the symptoms observed in AS patients.

Antisense oligonucleotides (ASO) are small single-stranded DNA sequences that are able to bind RNA transcripts. Once inside a cell the ASO binds to complementary RNAs and, depending on the binding-location, induces RNA breakdown or splicing modifications⁵⁰. ASOs are a potential treatment option for AS patients and other disorders that are caused by a clear dominant genetic defect, making it possible to reduce or modify translation from a specific RNA transcript. ASOs to treat children with spinal muscular atrophy⁵² and Duchenne muscular dystrophy⁵³ are already being used in the clinic. In most cell types, *UBE3A* is transcribed biallelically from both the maternal and paternal allele, as both promotor regions are unmethylated and active. In mature neurons, however, the paternal copy of *UBE3A* is silenced by a paternally expressed non-coding antisense transcript (*UBE3A-ATS*) (**Figure 2A**)^{155,156}. By designing ASOs that target and induce breakdown of the human *UBE3A-ATS* transcript, it is

possible to reactivate paternal *UBE3A* and restore *UBE3A* levels in AS patient derived neurons. Alternatively, ASOs targeting *UBE3A-sense* can be used to decrease *UBE3A* levels in healthy neurons or Dup15q to investigate the effect of loss of functional *UBE3A* in AS, or normalization of increased *UBE3A* levels in Dup15q neurons, during a later stage of development.

Hybridization of an ASO with complementary RNA strands takes place in a sequence-specific manner through Watson-Crick base pairing. Due to species differences in the genomic sequence, especially in non-coding regions, therapeutic ASOs should be designed based on the human genome and tested using human cells. Induced pluripotent stem cells (iPSC) provide an ideal platform to study the effectiveness and toxicity of therapeutic ASOs. We utilized this technique to manipulate *UBE3A* expression in human neurons derived from AS patients or healthy individuals both *in vitro* and *in vivo*. Treatment of brain disorders is often complicated by the blood-brain-barrier that tightly regulates the entry of compounds to the brain¹⁵⁷. To overcome this, ASOs need to be delivered directly into the cerebrospinal fluid of patients⁵². With the intention of incorporating the delivery method used in the clinic onto our model, we transplanted AS neurons into the brain of immunodeficient mice. ASOs specifically targeting the human *UBE3A-ATS* transcript were delivered intracerebroventricular (ICV) to these mice in an attempt to restore *UBE3A* in the transplanted human neurons. Besides AS this model can be used to screen ASOs designed to treat of NDDs, potentially moving towards personalized medicine for ultra-rare genetic NDDs.

Results

UBE3A levels in developing iPSC-derived neurons

Previous work using iPSCs derived from an AS patient has demonstrated that the silencing of paternal *UBE3A* expression occurs relatively late during neuronal development¹⁵⁸. In order to verify this claim and confirm the integrity of the methylation status of the PWS imprinting center, we created iPSC-derived neurons from a healthy individual and an AS patient carrying a nonsense mutation in the maternal copy of *UBE3A* (W577X). iPSC-lines were differentiated towards functional neurons using a previously published and extensively characterized protocol³⁵. iPSCs were first differentiated towards embryoid bodies (EBs) and subsequently towards neural precursor cells (NPCs), followed by terminal differentiation to a mixed neural culture containing neurons, astrocytes and NPCs (**Figure 3.1A**). Both wild-type control (WTC) and AS patient-derived NPCs showed *UBE3A* expression in cells that were positive for SOX2, a cell type-specific marker of neural stem cells. An occasional immature AS neuron, positive for both MAP2 and SOX2, was found to exhibit residual *UBE3A* expression (**Figure 3.1B**). 2 weeks into the differentiation process, both WTC and AS cultures contained mainly immature (MAP2+/NEUN-) neurons, in both cultures we detected *UBE3A* expression in these neurons. A few neurons in these young

Discussion

UBE3A levels in the brain are tightly regulated during neuronal development and maturation. Dysregulation of this protein leads to two distinct disorders – increased dosage gives rise to Dup15q, while depletion leads to AS¹⁵⁹. The mechanisms regulating expression and imprinting of the genomic region containing *UBE3A* are highly conserved between species¹⁶⁰, however, the human *UBE3A-ATS* sequence shows very limited homology to its rodent counterpart. Therefore, ASOs designed to reactivate the paternal *UBE3A* copy will only be effective in a human genetic background. We set out to create a model in which therapeutic ASOs for human NDDs can be tested *in vivo* towards future implementation in the clinic. In order to achieve this, human neurons were transplanted into the brain of neonatal immunodeficient mice followed by administration of ASOs into the cerebrospinal fluid of the recipient host mouse. Using this approach, we were able to restore *UBE3A* levels in human AS neurons while incorporating the ASO delivery method used in the clinic to treat other neurological disorders^{52,53}.

It remains largely unclear why loss of *UBE3A* in neurons leads to AS. Besides its role in the ubiquitin proteasome system, many targets have been proposed, some with a potential link to NDDs. *UBE3A* is predominantly localized to the nucleus, but is also observed at the synapse¹⁶¹, suggesting that *UBE3A* could independently influence global transcription in a cell and regulate the functioning of individual synapses. In AS mice, it has been shown that *Ube3a* directly regulates synaptic plasticity by controlling the integration of a small-conductance potassium channel, SK2, into synapses¹⁶². A different study looking at motor dysfunction in AS mice found that *Ube3a* controls the degradation of GABA transporter 1, influencing GABA concentrations in the synaptic cleft¹⁶³. Besides ligase-dependent activity, nuclear *UBE3A* is associated with euchromatin domains¹⁶¹, potentially influencing gene expression. Functioning of CaMKII, a protein necessary for learning and memory, is affected by *UBE3A* loss-of-function mutations. Decreasing inhibitory autophosphorylation of CaMKII in AS mice rescues the behavioral and learning phenotypes¹⁶⁴. These examples show the difficulty in explaining the mechanism by which *UBE3A* loss leads to strong effects on neuronal functioning and development, these could be caused by altered levels of putative *UBE3A* targets or as a result of changes in the proteasome system or neuronal functioning in general.

AS mouse models show increased excitability of neuronal networks¹⁶⁵, phenotypes for some behavioral tasks and reduced synaptic activity in neurons from the prefrontal cortex⁵⁷. iPSC-derived neurons from AS patients exhibit disrupted maturation, in which neurons failed to develop a hyperpolarized resting membrane potential and, similar to mouse models, showed increased synaptic activity¹⁶⁶. Interestingly, these electrophysiological phenotypes in iPSC-derived AS neurons could be rescued with ASOs during later stages of development, but not at an earlier timepoint. This contradicts findings in an AS mouse model in which temporally-

controlled reinstatement of *Ube3a* during embryonic or neonatal stages was able to rescue behavioral phenotypes, but not at later developmental ages⁵⁸. The *in vivo* time course of murine *Ube3a* reactivation after a single ASO dose remains poorly characterized. However, a prior study demonstrated enduring murine *Ube3a* reactivation up to 4 months after ASO treatment¹⁶⁷. How this relates to the clinic is not known and will require further research. SMA patients receive 6 ASO doses, up to 302 days after starting treatment, to maintain suppression of symptoms⁵².

Multiple (rare) NDDs are caused by an identifiable dysfunction or aggregation of a single protein, ASOs create a unique treatment opportunity for these disorders. The experimental approach presented here provides a platform to test therapeutic ASOs before translation to the clinic. Effectiveness and toxicity can be evaluated on human cells while also incorporating delivery method and potential off target effects in a model animal. AS is a relatively common disorder, enough patients have been identified to perform a randomized clinical trial. Advances in sequencing techniques have led to an increased identification of disease-causing variants, many of which could be manipulated using ASOs. Together these ultrarare variants are causative for a large proportion of NDDs¹⁶⁸. However, since these variants are so rare, a traditional clinical trial cannot be performed. Our platform could provide an alternative approach, variant-specific ASOs can be tested *in vivo* on human cells. Data acquired using our model will facilitate future translation of an effective ASO to the clinic. Currently, genetic screens are being performed in newborns for a defined set of genes, technical advances will make it possible to perform whole-exome or genome sequencing for every newborn¹⁶⁹. This will inherently lead to the identification of (novel) ultrarare variants, it is likely that for NDDs treatment will need to start before symptoms arise. For such dominant genetic variants with a severe phenotype, clinicians will need to decide together with the parents if ASO-treatment could be beneficial, without data from a clinical trial to support this process. The model we propose could at least provide insight into the efficacy of an ASO to modify the expression of a disease-associated protein.

using immunocytochemistry. Primary antibody incubation was performed overnight at 4°C. Secondary antibody incubation was done for 2 hours at room temperature. Both primary and secondary antibody incubation was performed in staining buffer [0.05 M Tris, 0.9% NaCl, 0.25% gelatin, and 0.5% Triton X-100 (Sigma, T8787) in PBS (pH 7.4)]. Primary antibodies and their dilutions can be found in **Table 3.2**. Secondary antibodies conjugated to Alexa-488, Alexa-647 or Cy3 were used at a dilution of 1:400 (Jackson ImmunoResearch). Nuclei were visualised using DAPI (ThermoFisher Scientific, D1306). Samples were mounted using Mowiol 4-88 (Sigma-Aldrich, 81381) and imaged using a Zeiss LSM 800 confocal microscope (Oberkochen, Germany).

Primed neuron engraftment in neonatal immunodeficient mice

All mouse experiments were approved by the local animal welfare committee. Before transplantation NPCs were differentiated in neural differentiation medium (**Table 3.1**) for 7-10 days. iPSC-derived primed neurons were transplanted into the brains of immunodeficient neonatal (P1-3) Rag2^{-/-} CB6F1/J mice. Pups underwent cryoanesthesia and 5-10 x 10⁴ cells were delivered in a 1 µl PBS-drop via a 1 mm-diameter pulled glass pipette into five different sites – in the posterior and anterior anlagen of the corpus callosum bilaterally and in the cerebellar peduncle dorsally¹⁴⁷. After the procedure pups were left to recover on a heating mat and placed back with their mother when fully awake. Mice were sacrificed at 6 and 8 weeks of age by transcardiac perfusion with saline followed by 4% PFA. Brains were removed, left in 4% PFA for 2 hours at room temperature, transferred to a 10% phosphate buffer (PB 0.1 M, pH 7.3) and stored overnight at 4°C. Brains were embedded in 12% gelatin/10% sucrose blocks, fixation was performed for 2 hours at room temperature in a 10% pFA/30% sucrose solution. Embedded brains were stored, at least overnight, at 4°C before being sliced into 40 µm slices on a freezing microtome (Leica, Wetzlar, Germany; SM 2000 R). Brain sections were pre-incubated with a blocking buffer (0.5% Triton X-100 (Sigma, T8787) and 10% normal horse serum (NHS; ThermoFisher, 16050122) in PBS) for 1 hr at room temperature. Primary antibody incubation was done for 48 hours at 4°C (**Table 3.2**). Secondary antibodies conjugated to Alexa-488, Alexa-647 or Cy3 were used at a dilution of 1:400 (Jackson ImmunoResearch), nuclei were visualised using DAPI (ThermoFisher Scientific, D1306) and incubation was done for 2 hours at room temperature. Both primary and secondary antibody incubation were performed in a staining buffer (2% NHS and 0.5% Triton X-100 in PBS). Samples were mounted using Mowiol 4-88 (Sigma-Aldrich, 81381) and imaged using a Zeiss LSM 800 confocal microscope (Oberkochen, Germany).

In vivo reactivation of UBE3A in grafted human AS-neurons

Reactivation of the paternal *UBE3A* allele was achieved by an ICV injection¹⁷⁰ of 75 or 95 µg ATS ASO at P21. Briefly, Rag2^{-/-} CB6F1/J mice were initially anaesthetized using 4% isoflurane and placed in a stereotaxic frame (David Kopf Instruments), sedation was

maintained using 1.5% isoflurane during the entire procedure. After exposing the skull, a glass needle (0.5-0.7 μm tip) was placed 0.5 mm posterior and 1.0 mm lateral to the bregma, and lowered to a depth of 1.5 mm from the meninges. A 3 μl ASO (25 or 28.3 $\mu\text{g}/\mu\text{l}$) or PBS injection was delivered at a rate 0.5 $\mu\text{l}/\text{min}$ using a syringe pump (CMA microdialysis, CMA400). Following the injection, the needle was left in place for an additional 5 minutes to ensure diffusion of the compound. After slow retraction of the needle, the skin incision was sutured and the animals were left to recover under a heating lamp.

Name	Reagents	Manufacturer, catalogue number
hES Medium	Advanced DMEM/F12 20% Knock-out serum replacement 1% MEM-NEAA 7 nl/ml β -mercaptoethanol 1% L-Glutamine 1% Penicillin-Streptomycin 10 ng/ml basic Fibroblast Growth Factor	ThermoFisher Scientific, 1634010 ThermoFisher Scientific, 10828028 ThermoFisher Scientific, 11140035 Sigma-Aldrich, M7522 ThermoFisher Scientific, 25030024 ThermoFisher Scientific, 15140122 Merck, GF003AF
Neural Induction Medium	Advanced DMEM/F12 1% N-2 Supplement 2 $\mu\text{g}/\text{ml}$ Heparin 1% Penicillin-Streptomycin	ThermoFisher Scientific, 1634010 ThermoFisher Scientific, 17502048 Sigma-Aldrich, H3149 ThermoFisher Scientific, 15140122
NPC Medium	Advanced DMEM/F12 1% N-2 Supplement 2% B-27 minus RA Supplement 1 $\mu\text{g}/\text{ml}$ Laminin 1% Penicillin-Streptomycin 20 ng/ml basic Fibroblast Growth Factor	ThermoFisher Scientific, 1634010 ThermoFisher Scientific, 17502048 ThermoFisher Scientific, 12587010 Sigma-Aldrich, L2020 ThermoFisher Scientific, 15140122 Merck, GF003AF
Neural Differentiation Medium	Neurobasal medium 1% N-2 Supplement 2% B-27 minus RA Supplement 1% MEM NEAA 2 $\mu\text{g}/\text{ml}$ Laminin 1% Penicillin-Streptomycin 20 ng/ml BDNF 20 ng/ml GDNF 1 μM db-cAMP 200 μM ascorbic acid	ThermoFisher Scientific, 21103049 ThermoFisher Scientific, 17502048 ThermoFisher Scientific, 12587010 ThermoFisher Scientific, 11140035 Sigma-Aldrich, L2020 ThermoFisher Scientific, 15140122 ProSpec, CYT-207 ProSpec, CYT-305 Sigma-Aldrich, D0627 Sigma-Aldrich, A5960

Table 3.1 Overview of media and reagents used during the differentiation protocol

Antibody	Dilution	Manufacturer, catalogue number
CD15 V450	1:100	BD Bioscience, 561584
CD24 PE-Cy7	1:250	BD Bioscience, 561646
CD44 FITC	1:100	BD Bioscience, 560977
CD184 APC	1:250	BD Bioscience, 560936
CD271 PE	1:500	BD Bioscience, 560927
GFAP	1:200	Millipore, AB5804
Human Nuclei	1:500	Millipore, MAB1281
MAP2	1:200	Synaptic Systems, 188004
SOX2	1:200	Millipore, AB5603
STEM121	1:500	Takara Bio, Y40410
UBE3A	1:200	Sigma, SAB1404508
UBE3A	1:200	Bethyl, BET A300-352A-T

Table 3.2 Overview of primary antibodies used

4

Candidate *CSPG4* mutations and induced pluripotent stem cell modeling implicate oligodendrocyte progenitor cell dysfunction in familial schizophrenia

Evidence for oligodendrocyte progenitor cell dysfunction in schizophrenia

FMS de Vrij^{1#}, CG Bouwkamp^{1,2#}, N Gunhanlar^{1#}, G Shpak¹, B Lendemeijer¹, M Baghdadi¹, M Ghazvini³, TM Li³, M Quadri², S Olgiati², GJ Breedveld², M Coesmans^{1,12}, E Mientjes^{9,10}, T de Wit², FW Verheijen², HB Beverloo², D Cohen¹³, RM Kok¹⁴, PR Bakker^{15,16}, A Nijburg¹⁴, AT Spijker¹⁴, PMJ Haffmans¹⁷, E Hoencamp^{14,18}, V Bergink¹, GROUP Study Consortium[†], JA Vorstman¹⁹, T Wu²⁰, LM Olde Loohuis²⁰, N Amin⁴, CD. Langen^{6,7,8}, A Hofman⁴, WJG Hoogendijk¹, CM van Duijn⁴, MA Ikram^{4,5,6}, MW Vernooij^{4,6}, H Tiemeier^{1,4,7}, AG Uitterlinden^{4,11}, Y Elgersma^{9,10}, B Distel^{21,9}, J Gribnau³, T White⁷, V Bonifati², SA Kushner^{1*}

¹ Department of Psychiatry, Erasmus Medical Center, Rotterdam, The Netherlands

² Department of Clinical Genetics, Erasmus Medical Center, Rotterdam, The Netherlands

³ Department of Developmental Biology, and Erasmus MC iPS Facility, Erasmus Medical Center, Rotterdam, The Netherlands

⁴ Department of Epidemiology, Erasmus Medical Center, Rotterdam, The Netherlands

⁵ Department of Neurology, Erasmus Medical Center, Rotterdam, The Netherlands

⁶ Department of Radiology, Erasmus Medical Center, Rotterdam, The Netherlands

⁷ Department of Medical Informatics, Erasmus Medical Center, Rotterdam, The Netherlands

⁸ Biomedical Imaging Group Rotterdam, Departments of Radiology & Medical Informatics, Erasmus Medical Center, Rotterdam, The Netherlands

⁹ Department of Neuroscience, Erasmus Medical Center, Rotterdam, The Netherlands

¹⁰ ENCORE Expertise Center For Neurodevelopmental Disorders, Erasmus Medical Center, Rotterdam, The Netherlands

¹¹ Department of Internal Medicine, Erasmus Medical Center, Rotterdam, The Netherlands

¹² Delta Psychiatric Center, Poortugaal, The Netherlands

¹³ Mental Health Care Organization North-Holland North, Heerhugowaard, The Netherlands

¹⁴ Parnassia Psychiatric Institute, The Hague, The Netherlands

¹⁵ Department of Psychiatry and Psychology, School of Mental Health and Neuroscience, Maastricht University Medical Center, Maastricht, The Netherlands

¹⁶ Psychiatric Center GGZ Centraal, Amersfoort, The Netherlands

¹⁷ Faculty of Social and Behavioral Sciences Clinical, Health and Neuro Psychology, Department of Affective Disorders, PsyQ, Leiden University, The Netherlands

¹⁸ Institute of Psychology, Leiden University, The Netherlands

¹⁹ Department of Psychiatry, Brain Center Rudolf Magnus, University Medical Center Utrecht, The Netherlands

²⁰ Center for Neurobehavioral Genetics, Semel Institute for Neuroscience and Human Behavior, University of California, Los Angeles, CA, USA

²¹ Department of Medical Biochemistry, Academic Medical Centre, Amsterdam, The Netherlands

[#] These authors contributed equally

[†] Investigators from the GROUP study consortium are listed in the Supplement

* Correspondence to S.A.K. (s.kushner@erasmusmc.nl)



Abstract

Schizophrenia is highly heritable, yet its underlying pathophysiology remains largely unknown. Among the most well-replicated findings in neurobiological studies of schizophrenia are deficits in myelination and white matter integrity; however, direct etiological genetic and cellular evidence has thus far been lacking. Here, we implement a family-based approach for genetic discovery in schizophrenia combined with functional analysis using induced pluripotent stem cells (iPSCs). We observed familial segregation of two rare missense mutations in *Chondroitin Sulfate Proteoglycan 4* (*CSPG4*) (c.391G>A [p.A131T], MAF 7.79×10^{-5} and c.2702T>G [p.V901G], MAF 2.51×10^{-3}). The *CSPG4*^{A131T} mutation was absent from the Swedish Schizophrenia Exome Sequencing Study (2536 cases, 2543 controls), while the *CSPG4*^{V901G} mutation was nominally enriched in cases (11 cases vs. 3 controls, $P=0.026$, OR 3.77, 95% CI 1.05–13.52). *CSPG4*/NG2 is a hallmark protein of oligodendrocyte progenitor cells (OPCs). iPSC-derived OPCs from *CSPG4*^{A131T} mutation carriers exhibited abnormal post-translational processing ($P=0.029$), subcellular localization of mutant NG2 ($P=0.007$), as well as aberrant cellular morphology ($P=3.0 \times 10^{-8}$), viability ($P=8.9 \times 10^{-7}$), and myelination potential ($P=0.038$). Moreover, transfection of healthy non-carrier sibling OPCs confirmed a pathogenic effect on cell survival of both the *CSPG4*^{A131T} ($P=0.006$) and *CSPG4*^{V901G} ($P=3.4 \times 10^{-4}$) mutations. Finally, *in vivo* diffusion tensor imaging of *CSPG4*^{A131T} mutation carriers demonstrated a reduction of brain white matter integrity compared to unaffected sibling and matched general population controls ($P=2.2 \times 10^{-5}$). Together, our findings provide a convergence of genetic and functional evidence to implicate OPC dysfunction as a candidate pathophysiological mechanism of familial schizophrenia.

Introduction

Schizophrenia is a severely debilitating psychiatric disorder affecting ~1% of the population worldwide¹⁷¹. The strongest known determinant for developing schizophrenia is family history. A meta-analysis which included five decades of twin studies concluded a heritability estimate (h^2) of 0.77 ± 0.05 , with a relatively limited contribution of shared environmental influences (c^2) (0.013 ± 0.025)¹⁷².

The Psychiatric Genomics Consortium recently reported a genome-wide association study (GWAS) investigating 36,989 cases and 113,075 controls, in which 128 genome-wide significant single-nucleotide variants were identified across 108 independent genomic loci, suggesting an important contribution of common genetic variation to schizophrenia risk¹⁷³. However, a large proportion of the heritability for schizophrenia remains unexplained, leaving many genetic variants remaining to be discovered. Therefore, increasing attention has also been focused on the potential contribution of rare genomic variation to schizophrenia risk. Copy number variants (CNVs) are a well established source of pleiotropic risk, ranging from asymptomatic carriership to a complex constellation of symptoms affecting multiple organ systems, such as the 22q11.2 microdeletion syndrome¹⁷⁴. In a large-scale schizophrenia case-control cohort analysis, known pathogenic CNVs were significantly more frequent in cases (2%) than controls (0.4%)^{175,176}. Moreover, an independent study found that large (>500kb) CNVs are enriched in loci associated with schizophrenia by GWAS and frequently involve genes encoding proteins located in the postsynaptic density¹⁷⁷.

In addition to microarray-based genotyping methods, the development of next-generation sequencing has allowed the possibility to examine whether rare single nucleotide variants or small insertions-deletions contribute to schizophrenia risk. A Swedish cohort including 2,536 cases and 2,543 controls yielded no single mutation or single gene reaching genome-wide significance for association with schizophrenia, but confirmed a similar enrichment of gene sets for synaptic function as previously identified for genes located in schizophrenia-associated CNVs and GWAS loci¹⁷⁸. Moreover, trio-based studies have identified a number of candidate genes through identification of recurrent *de novo* mutations^{179,180} and an increased burden of mutations occurring in genes encoding glutamatergic postsynaptic proteins¹⁸¹.

Recent genetic and induced pluripotent stem cell (iPSC)-based studies have converged on a model by which neuronal function, and in particular synaptic transmission, is a major pathophysiological mechanism of schizophrenia^{34,173,178,181,182}. However, functional neuronal alterations may arise either by direct cell-type autonomous changes to neurons themselves, or indirectly through a primary pathophysiological influence on other cell types that influence neuronal function. Numerous studies have reported the involvement of glial cell biology in the pathophysiology of schizophrenia, including alterations in oligodendrocytes, myelination, and white matter integrity^{183–188}, which directly regulate neuronal function.

Abnormalities of the integrity of the white matter are strongly associated with schizophrenia¹⁸⁹. The late adolescent critical period for cerebral cortex myelination has long been recognized as overlapping closely with the typical age of onset for schizophrenia^{185,186}. Myelination-related genes have been shown to be enriched for common variants associated independently to white matter integrity¹⁹⁰ and schizophrenia^{184,191}. Two recent brain imaging studies have elegantly compared white matter integrity in 16p11.2 deletion and duplication carriers^{192,193} of which only the 16p11.2 duplication confers increased risk for schizophrenia¹⁷⁶. Notably, both global fractional anisotropy and white matter volume were selectively decreased in 16p11.2 duplication carriers. However, despite increasing evidence of an association between schizophrenia and myelination integrity, the molecular and cellular mechanisms by which oligodendrocyte lineage dysfunction might influence schizophrenia risk have remained largely unknown.

We now report genetic and functional evidence of oligodendrocyte progenitor cell dysfunction in schizophrenia. Using a family-based genetic approach, we observed multiple rare missense mutations in *CSPG4* that segregate with schizophrenia. Functional studies using iPSCs reprogrammed from affected *CSPG4* mutation carriers and their unaffected non-carrier siblings revealed that patient-derived OPCs exhibit abnormal post-translational processing, aberrant subcellular localization of CSPG4/NG2, and abnormal cellular morphology. Moreover, diffusion tensor imaging of *CSPG4* mutation carriers confirmed a global impairment in white matter integrity, together providing support for OPC dysfunction as a candidate pathophysiological mechanism of schizophrenia.

Results

Genetic findings in the discovery family

A non-consanguineous family of Dutch ancestry was ascertained with a pattern of schizophrenia inheritance compatible with autosomal dominant transmission. The core pedigree consisted of a couple and their nine children (5 males, 4 females) of whom the father and 4 sons suffered from non-syndromic schizophrenia (**Figure 4.1A** and **Supplementary Table 4.1**).

Genome-wide parametric linkage analysis was performed on peripheral blood DNA using an autosomal-dominant, affected-only model of inheritance, in order to identify genomic regions shared among all affected family members (**Supplementary Table 4.2**). Whole exome sequencing was performed on three individuals of the family (pedigree IDs: II-2, III-5 and III-9; **Figure 4.1A**). Five candidate heterozygous variants were identified based on the following criteria: a) located within the genomic regions shared among all affected family members, b) predicted to affect protein coding (missense, nonsense, frameshift, splice site), c) called in at least one of the affected individuals [III-5 and III-9], d) absent from the unaffected mother [II-2], e) absent from dbSNP129, and f) with a minor allele frequency (MAF) < 0.001 in the Exome Aggregation Consortium (ExAC) browser (Europeans non-Finnish)¹⁹⁴, EVS6500 European Americans, NHLBI Exome Sequencing Project (ESP)¹⁹⁵, 1000 Genomes¹⁹⁶, and Genome of the Netherlands (GoNL)¹⁹⁷ cohorts (**Supplementary Table 4.3**). Genotyping of these variants was performed by Sanger sequencing in all participating family members.

Among the five candidate variants, *CSPG4* c.391G>A (p.A131T) was the only variant shared by all affected family members and absent in all unaffected relatives, including in the extended family (**Figure 4.1A**). *CSPG4* c.391G>A (p.A131T) is present in the ExAC browser (Total [forward strand]: T=6/C=118,148 alleles [MAF 5.08×10^{-5}], European (Non-Finnish): T=5/C=64,215 alleles [MAF 7.79×10^{-5}])¹⁹⁴ but absent from the Swedish Schizophrenia Exome Sequencing Study (2536 cases, 2543 controls)¹⁷⁸, 1000 Genomes¹⁹⁶ and GoNL¹⁹⁷.

Additional genotyping of CSPG4 discovery family variant

In an effort to further characterize the frequency of *CSPG4* c.391G>A (p.A131T) in the Netherlands, we performed TaqMan genotyping and Sanger sequencing validation in an independent Dutch cohort of 1219 schizophrenia cases and in the general population-based Rotterdam Study cohort¹⁹⁸ (10,611 subjects). One carrier was identified among the schizophrenia cases (MAF_{cases} 4.1×10^{-4}) and three within the general population (MAF_{population} 1.4×10^{-4}). The patient carrier had a long history of severe psychiatric illness including multiple hospital admissions and chronic anti-psychotic and anti-depressant medication. Her most recent prescriptions included penfluridol oral depot (20 mg/week)

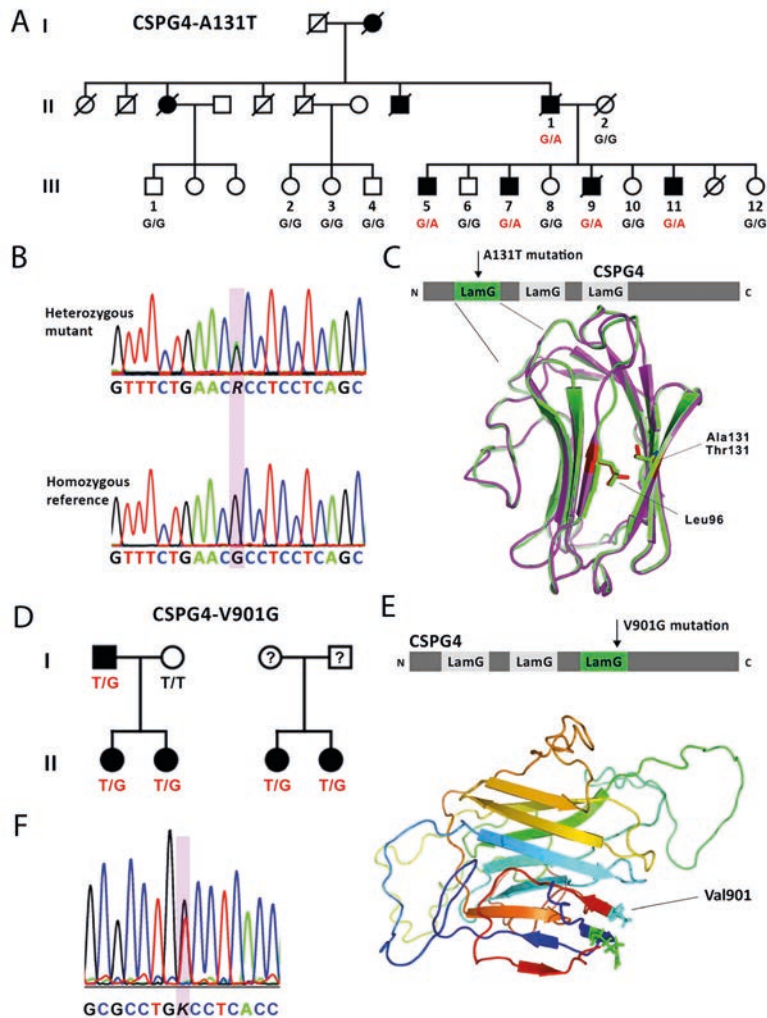


Figure 4.1 Familial segregation of CSPG4 mutations with schizophrenia. **(A)** Pedigree of multiplex discovery family with schizophrenia. Symbols: filled, schizophrenia; open, unaffected; G/A, heterozygous carrier of the CSPG4 c.391G>A mutation (CSPG4A131T); G/G, homozygous reference. **(B)** Representative sequencing results for heterozygous carriers of the CSPG4 c.391G>A mutation. The lower panel reflects homozygous reference sequence. **(C)** Homology model of the first Laminin G domain of CSPG4. Structural alignment of the reference (green) and mutant model (magenta) reveals a difference in the predicted interaction between amino acid positions 131 and 96 (Leu) in the opposing β -strand inside the hydrophobic core of the β -sandwich (predicted alterations of the side-chains in red). **(D)** Family pedigrees segregating the CSPG4 c.2702T>G mutation (CSPG4V901G). Symbols: filled, schizophrenia; open, unaffected; T/G, heterozygous carrier of the CSPG4 c.2702T>G mutation; T/T, homozygous reference. **(E)** Three-dimensional structural homology modeling of the putative 3rd LamG domain of CSPG4 (a.a. 634-921), demonstrating the outside surface location of Val901. **(F)** Representative Sanger sequencing trace of heterozygous carrier of the CSPG4 c.2702T>G mutation.

and venlafaxine (37.5 mg/day). Family members could not be ascertained for additional psychiatric history or genotyping. Among the three unrelated carriers (maximum pairwise $\hat{\pi} = 0.078$) identified in the Rotterdam Study general population cohort, two had a clinically significant history of psychiatric illness ($\hat{\pi} = 0.055$). One of the subjects had a history of multiple inpatient psychiatric hospitalizations for depression, and the other required chronic antidepressant and anxiolytic pharmacotherapy. Notably these findings were unlikely due to chance alone, given the 12.76% period prevalence of antidepressant use in the Rotterdam Study cohort and 0.065% annual prevalence of inpatient psychiatric hospitalization in the Netherlands^{199,200} (Binomial $P = 8.8 \times 10^{-3}$).

Identification of a second rare *CSPG4* variant that segregates with schizophrenia

A previous study identified suggestive linkage at chromosome 15q22-24, containing *CSPG4*, in a cohort of 175 families with schizophrenia or schizoaffective disorder of Central American/Hispanic origin^{201,202}. We therefore sequenced the full open reading frame of *CSPG4* in one proband from each of the 73 families that positively contributed to the linkage signal at this locus (markers D15S131 and D15S655) (**Supplementary Table 4.4**). Four rare missense variants were identified with MAF < 0.005 (ExAC Browser Latino) (**Figure 4.1, Supplementary Figure 4.1**). However in contrast to the other three variants, *CSPG4* c.2702T>G (p.V901G) was found in two independent families, without evidence of incomplete penetrance (**Figure 4.1D, F**), and located within a LamG domain similar to the c.391G>A (p.A131T) discovery family variant (**Figure 4.1**). Moreover, the c.2702T>G p.V901G variant was nominally enriched in cases from the Swedish Schizophrenia Exome Sequencing Study¹⁷⁸ (MAF_{cases} 2.19×10^{-3} ; MAF_{controls} 5.82×10^{-4} , Fisher's Exact Test $P = 0.026$, OR 3.77, 95% CI 1.05-13.52). Together, these findings suggest that rare coding variants of *CSPG4* might influence the risk of familial schizophrenia.

Structural protein modeling of *CSPG4* mutations

The *CSPG4*^{A131T} and *CSPG4*^{V901G} mutations are located within the first and third Laminin G domain of the protein encoded by *CSPG4*, known as neural/glial 2 (NG2) (**Figure 4.1C, E**). Laminin G (LamG) domains are highly conserved across a diverse group of extracellular matrix proteins²⁰³. Intriguingly, several schizophrenia-associated genes such as *NRXN1* and *LAMA2* also contain LamG domains^{180,204–206}. Crystal structures of LamG domains in the Protein Data Bank allowed homology modeling of the LamG domains of NG2. Models implemented using Phyre2²⁰⁷ and I-TASSER²⁰⁸ both suggested that in the reference sequence, Ala¹³¹ and Leu⁹⁶ interact across opposing β -sheets inside the hydrophobic core of the β -sandwich. The mutation of Ala¹³¹, which has a small hydrophobic side chain, to Thr¹³¹, containing a larger polar side-chain, suggests a conformational change impairing the proper folding of the β -sandwich (**Figure 4.1C**).

Interestingly, *CSPG4*^{V901G} is located in a putative 3rd LamG domain predicted by I-TASSER²⁰⁸ (a.a. 634-921, **Figure 4.1E**). This region has not previously been annotated as a LamG domain, despite the striking structural homology to other LamG domains with available crystal structures, most notably that of NRXN1^{209–211}. In contrast to the *CSPG4*^{A131T} mutation that is located on the inside of the globular structure of the first LamG domain of NG2, the *CSPG4*^{V901G} mutation is predicted to be located on the outside of the putative third LamG domain (**Figure 4.1E**), therefore perhaps affecting protein-protein interactions. Intriguingly, the same protein region has been found to bind to collagen V and VI, implicated in cell adhesion and migration of NG2-expressing cells^{212,213}.

Family-based iPSC modeling of the CSPG4A131T mutation

No evidence for a cell-autonomous neuronal phenotype

Recent genetic and iPSC-based studies of schizophrenia have converged on a model by which neuronal function, and in particular synaptic transmission, is a major pathophysiological mechanism^{34,173,178,181,182}. We obtained skin biopsies for iPSC reprogramming from three affected *CSPG4*^{A131T} carriers and three unaffected non-carriers within the core sibship of the discovery family (**Supplementary Figure 4.2 A-D**). Directed differentiation of iPSCs yielded forebrain-specified neural progenitor cells (NPCs) uniformly positive for Nestin, SOX2, Vimentin, and FOXP1 (**Supplementary Figure 4.2E**).

NPCs were differentiated to neural cultures for 8-10 weeks, which notably lack cells of the oligodendrocyte lineage including OPCs. Both control and patient-derived neurons developed robust synaptic network connectivity, confirmed by confocal immunofluorescence (**Figure 4.2, A-C**) and whole-cell patch-clamp electrophysiological recordings (**Figure 4.2, D-R**). Overall, neurons derived from patient carriers and their unaffected siblings had similar electrophysiological properties, including passive membrane properties, action potential characteristics, and synaptic physiology. Of the twelve different electrophysiological parameters examined, input resistance ($t_{50}=2.54$, $P=0.01$) and action potential threshold ($t_{49}=2.84$, $P=0.007$) exhibited nominally significant differences that did not survive Bonferroni correction. Accordingly, the lack of a robust neuronal phenotype is consistent with the absence of expression of NG2 in neurons²¹⁴.

Abnormal posttranslational processing and subcellular localization of CSPG4^{A131T} in OPCs

Given the highly abundant expression of NG2 in OPCs, widely referred to as NG2 cells, we next sought to investigate the influence of the *CSPG4*^{A131T} mutation on iPSC-derived OPCs.

Directed differentiation of iPSCs to OPCs resulted in robust expression of the lineage specific markers NG2, PDGFR α , Olig2, and SOX10 (**Supplementary Figure 4.3**). We first examined the subcellular distribution of NG2, as the structural homology modeling of the *CSPG4*^{A131T} mutation suggested aberrant protein folding (**Figure 4.1C**). Since NG2 is a transmembrane protein, it requires processing by the secretory pathway. Consistent with an impairment of protein processing, *CSPG4*^{A131T} patient-derived OPCs showed a highly abnormal subcellular localization of NG2 exemplified by an increase of co-localization with the endoplasmic reticulum marker calreticulin ($t=5.08$, $P = 0.007$) (**Figure 4.3A, B**).

In order to further characterize the alteration of NG2 subcellular localization, we performed surface biotinylation of *CSPG4*^{A131T} patient and non-carrier sibling control OPCs. NG2 is known to undergo extensive posttranslational modification^{215,216}, including the addition of chondroitin sulfate moieties at Ser999²¹⁷. Consequently, NG2 appears as multiple bands by western blotting: a sharp band at 300 kDa corresponding to an unmodified form of NG2 which lacks chondroitin sulfate side chains, and a large polydisperse smear at >300 kDa corresponding to NG2 with chondroitin sulfate modification. Pre-incubation with chondroitinase ABC to enzymatically cleave the chondroitin sulfate side chains eliminated the >300 kDa polydisperse smear (modified NG2) and increased the 300 kDa band (unmodified NG2) (**Supplementary Figure 4.4A**).

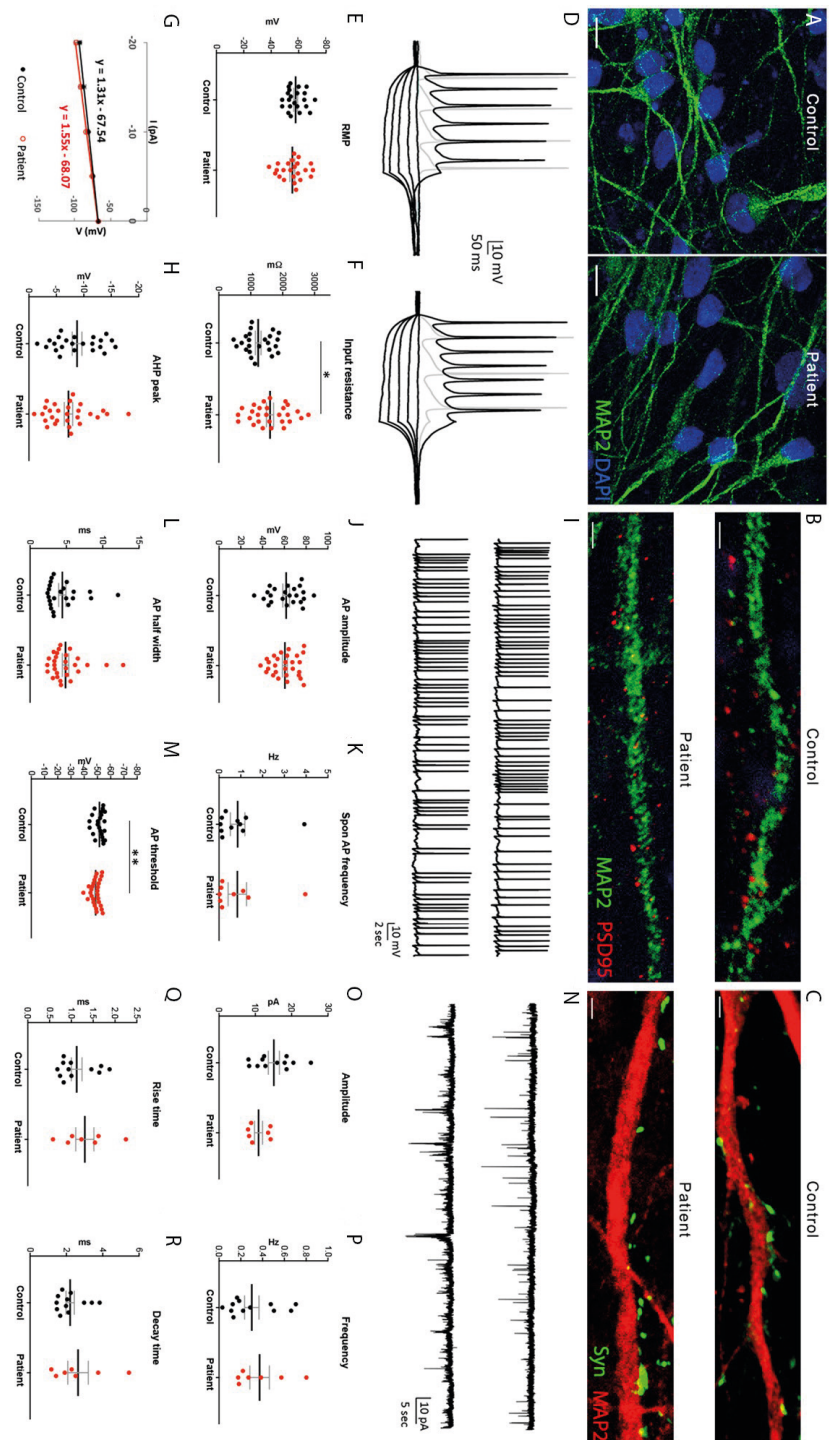
The total level of NG2 protein was similar between patient and control OPCs in whole cell lysates ($t=0.51$, $P = 0.62$) (**Supplementary Figure 4.4, 4.5**). However, patient OPCs exhibited a significant decrease in the ratio of modified versus unmodified NG2 compared to control OPCs. This finding was observed in whole cell lysate ($t=2.88$, $P=0.04$), as well as independently in the intracellular ($t=3.50$, $P=0.02$) and surface protein fractions of OPCs ($t=3.31$, $P=0.03$) (**Supplementary Figure 4.4B, C**). Taken together, these results demonstrate that the *CSPG4*^{A131T} mutation results in abnormal processing of NG2 protein.

Abnormal morphology of OPCs derived from *CSPG4*^{A131T} mutation carriers

In addition to the abnormal processing of NG2 protein, we also observed distinct morphological differences between OPCs derived from patients and controls (**Figure 4.3C**). Patient-derived OPCs exhibited a size distribution that was strongly shifted towards smaller cells, a finding that was highly significant across all patient and control lines (Kolmogorov-Smirnov $D=0.25$, $P=3.0 \times 10^{-8}$; **Figure 4.3D**). Overall, these results suggest that abnormal processing of NG2 influences the function of OPCs derived from *CSPG4*^{A131T} mutation carriers.

Patient OPCs have reduced viability and oligodendrogenesis

Abnormally high co-localization of mutant NG2 with calreticulin is consistent with retention of misfolded mutant NG2 in the endoplasmic reticulum. The extensive literature demonstrating

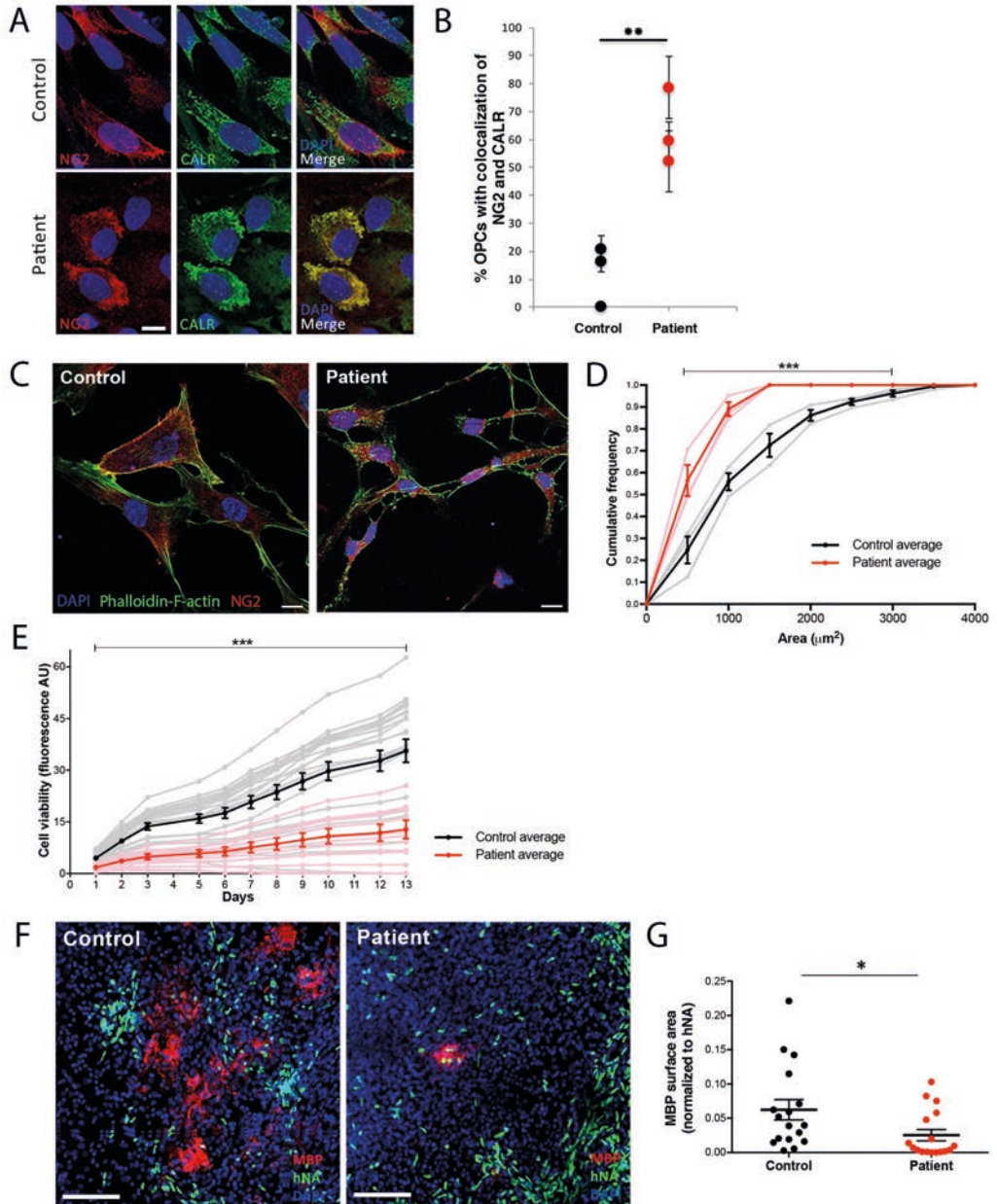


← **Figure 4.2** Normal passive, active, and synaptic function in *CSPG4^{A131T}* patient iPSC-derived neurons. **(A)** Immunostaining of iPSC-derived neural cultures after 8 weeks of differentiation (scale bar = 10 μ m). **(B, C)** Immunostaining with MAP2, PSD95 and synapsin antibodies confirmed the presence of synaptic proteins on dendrites of iPSC-derived neurons 8 weeks post-differentiation (scale bar = 2 μ m). **(D-R)** Electrophysiological measurements of iPSC-derived neurons. **(D)** Representative voltage responses to hyperpolarizing (-20 – 0 pA, 5 pA increments) and depolarizing (10 and 20 pA) current steps (left: control, right: patient). **(E)** Resting membrane potential (RMP) ($t_{44}=1.04$, $P=0.30$). **(F)** Input resistance ($t_{50}=2.54$, $P=0.01$). **(G)** Current-voltage (I-V) relationship of patient and control cells. **(H)** AHP peak ($t_{49}=1.35$, $P=0.18$). **(I)** Representative traces of spontaneous action potential (AP) firing (50 sec at RMP; top: control, bottom: patient). **(J)** AP amplitude ($t_{49}=0.31$, $P=0.76$). **(K)** Spontaneous firing rate ($t_{19}=0.03$, $P=0.98$). **(L)** AP half width ($t_{49}=0.65$, $P=0.52$). **(M)** AP voltage threshold ($t_{49}=2.84$, $P=0.007$). **(n)** Representative traces of spontaneous postsynaptic currents (100 sec at -90 mV; top: control, bottom: patient). **(O)** sPSC amplitude ($t_{17}=1.94$, $P=0.07$). **(P)** sPSC frequency ($t_{17}=0.65$, $P=0.52$). **(Q)** sPSC rise time ($t_{17}=0.84$, $P=0.41$). **(R)** sPSC decay time ($t_{17}=0.84$, $P=0.41$). **(D-R)**, Unpaired two-tailed Student's t-test. Passive properties and evoked APs ($N=24$ control, $N=28$ patient). Spontaneous APs ($N=11$ control, $N=9$ patient). Spontaneous postsynaptic currents ($N=12$ control, $N=7$ patient). All error bars are +/- standard errors of the mean (SEM).

impairments of cell viability resulting from misfolded proteins^{218,219} led us to hypothesize that the abnormal subcellular distribution of mutant NG2 might reduce the viability of OPCs. Therefore, we performed a longitudinal monitoring of cell viability using a quantitative fluorescence-based indicator based on the conversion of non-fluorescent resazurin to its fluorescent metabolite resorufin²²⁰. As evident throughout the entire 13-day time course of monitoring, OPCs derived from *CSPG4*^{A131T} mutation carriers exhibited a significant decrease of cell viability (two-way repeated measures ANOVA, $P=8.9 \times 10^{-7}$; **Figure 4.3E**).

OPCs are the exclusive precursor of oligodendrocytes²²¹. Given the reduced viability of patient OPCs, we also investigated whether their maturation to oligodendrocytes might also be impacted. Therefore, we performed *ex vivo* co-culture of control and patient OPCs with organotypic slices of cerebral cortex from myelin-deficient Shiverer mice that carry a homozygous mutation of *Mbp*. The Shiverer myelination assay is a widely implemented method for assessing the myelination potential of OPCs, using culture conditions that promote OPCs differentiation to myelinating oligodendrocytes²²². Consequently, MBP expression is entirely attributable to cells differentiated from the transplanted human OPCs, since Shiverer mice themselves lack Mbp. Consistent with their decreased viability, patient OPCs exhibited an impaired maturation to MBP-expressing oligodendrocytes ($t=2.17$, $P=0.038$; **Figure 4.3F, G**).

→ **Figure 4.3** Aberrant NG2 subcellular localization, morphology, and viability of *CSPG4*^{A131T} patient OPCs. **(A, B)** Immunostaining for NG2 and calreticulin (CALR) reveals increased ER colocalization of NG2 in patient OPCs (scale bar=10 μ m). Quantification was performed in two independent experiments with three control and three patient OPC lines each ($t=5.08$, $P=0.007$). **(C)** OPCs derived from mutation carriers exhibit an abnormally small morphology (scale bars=10 μ m). **(D)** Cumulative distribution of OPC area (μ m²; $n=361$ control cells, $n=217$ patient cells) demonstrates that OPCs derived from affected mutation carriers are significantly smaller than from their unaffected non-carrier siblings. Control and patient cell size distributions were compared by Kolmogorov–Smirnov test ($D=0.25$, $P=3.0 \times 10^{-8}$). Dark lines show group mean \pm standard error. Gray and pink lines show the results from each of the individual control and patient subjects, respectively. **(E)** Fluorometric cell viability assay of OPCs derived from affected mutation carriers vs. their unaffected non-carrier siblings (two-way repeated measures ANOVA, $P=8.9 \times 10^{-7}$). **(F)** Representative z-stacked images of organotypic cerebral cortex slices of homozygous shiverer mice transplanted with OPCs derived from affected mutation carriers or their unaffected non-carrier siblings. Human nuclear antigen (hNA), green; MBP, red (scale bar=100 μ m). **(G)** MBP surface area normalized to hNA⁺ cells per slice ($t=2.17$, $P=0.038$).



Transfection of OPCs with mutant isoforms of NG2

To further investigate the causality of the *CSPG4*^{A131T} and *CSPG4*^{V901G} mutations, we transfected either the wild-type (WT) or mutant isoforms into OPCs derived from healthy non-carrier siblings. Expression of *CSPG4*^{A131T} recapitulated the abnormal retention in the endoplasmic reticulum, similarly as observed in patient OPCs (one-way ANOVA, WT vs. A131T: $P=5.2 \times 10^{-9}$; **Figure 4.4A, B**). Moreover, OPCs expressing the *CSPG4*^{V901G} mutation also exhibited a significantly increased proportion of cells with co-localization to the endoplasmic reticulum compared to WT transfected OPCs (WT vs. V901G: $P=7.5 \times 10^{-6}$), albeit lower than observed for the *CSPG4*^{A131T} mutation. Notably, however, expression of the *CSPG4*^{V901G} mutation resulted in a distinct accumulation within putative intracellular vesicles that was evident in both OPCs (**Figure 4.4A**, inset) and U373 glioblastoma cells (**Supplementary Figure 4.6**), but not observed with expression of the *CSPG4*^{A131T} mutation in either of these cell types. At present, although we have not yet succeeded in identifying the subcellular compartment to which these *CSPG4*^{V901G}-expressing intracellular vesicles belong, lysosomes have been excluded based on the lack of significant co-localization with lysosomal-associated membrane protein 1 (**Supplementary Figure 4.6**).

Lastly, we sought to evaluate the causality of *CSPG4* mutations for mediating the impaired cell viability observed for patient OPCs. Therefore, we performed transient transfections of either WT or mutant NG2 isoforms into OPCs derived from healthy non-carrier siblings and assessed cell survival after 48 h when plasmid expression was maximal. OPCs transfected with either *CSPG4*^{A131T} or *CSPG4*^{V901G} exhibited a significant decrease in survival compared to *CSPG4*^{WT} (one-way ANOVA, WT vs. A131T: $P=0.006$; WT vs. V901G: $P=3.4 \times 10^{-4}$; **Figure 4.4C**). Notably, we also attempted the same experiment with patient OPCs; however, patient OPCs consistently died following the transfection procedure, regardless of whether the transfection was performed using WT or mutant NG2, or empty vector, a finding that independently confirms their distinct vulnerability.

Impaired white matter microstructure in *CSPG4*^{A131T} mutation carriers

Given the observed abnormalities of patient-derived OPCs, we reasoned that affected *CSPG4*^{A131T} mutation carriers might exhibit impairments of white matter integrity since OPCs are the exclusive precursor of myelinating oligodendrocytes. Therefore, we performed brain magnetic resonance imaging (MRI)-based diffusion tensor imaging (DTI) in affected carrier and unaffected non-carrier siblings and compared them with 294 subjects from the general population Rotterdam Study cohort matched for age, gender, smoking behavior, and alcohol use (**Figure 4.5A**). DTI images were analysed for global and focal reductions in fractional anisotropy (FA), the latter referred to as white matter potholes²²³. Consistent with the hypothesis that the *CSPG4*^{A131T} mutation compromises the integrity of myelination, affected carriers exhibited both a significantly higher number of white matter potholes ($P=2.2 \times 10^{-5}$) and lower global FA ($P=8.2 \times 10^{-3}$), compared to unaffected sibling and matched general population controls (**Figure 4.5B, C**).

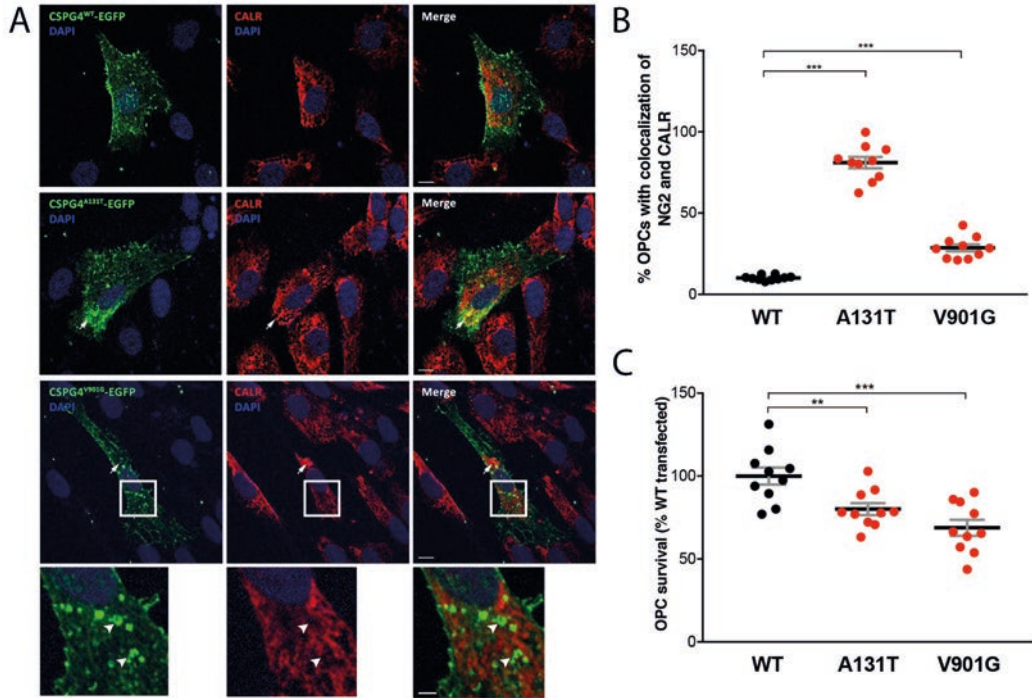


Figure 4.4 Transfection of *CSPG4*^{A131T} and *CSPG4*^{V901G} mutations in healthy non-carrier sibling OPCs. Control OPCs were transiently transfected with plasmids expressing WT or mutant *CSPG4* isoforms fused to EGFP. **(A)** Confocal images of transfected cells confirm a normal extracellular membrane-localization of *CSPG4*^{WT}-EGFP. In contrast, a high proportion of OPCs transfected with *CSPG4*^{A131T}-EGFP exhibited colocalization with the endoplasmic reticulum marker calreticulin (CALR), reminiscent to patient OPCs with endogenous *CSPG4*^{A131}. OPCs expressing *CSPG4*^{V901G}-EGFP also revealed an increased proportion with CALR colocalization, but additionally demonstrated a distinctly abnormal targeting within putative intracellular vesicles that were negative for CALR (insets) (scale bars: main panels=10µm, insets=3µm). **(B)** Percentage of transfected OPCs with colocalization of *CSPG4* isoforms with CALR (WT vs. A131T: $t=10.36$, $P=5.2 \times 10^{-9}$; WT vs. V901G: $t=6.20$, $P=7.5 \times 10^{-6}$). **(C)** Cell survival at 48h after transfection of OPCs (WT vs. A131T: $t=3.11$, $P=0.006$; WT vs. V901G: $t=4.41$, $P=3.4 \times 10^{-4}$).

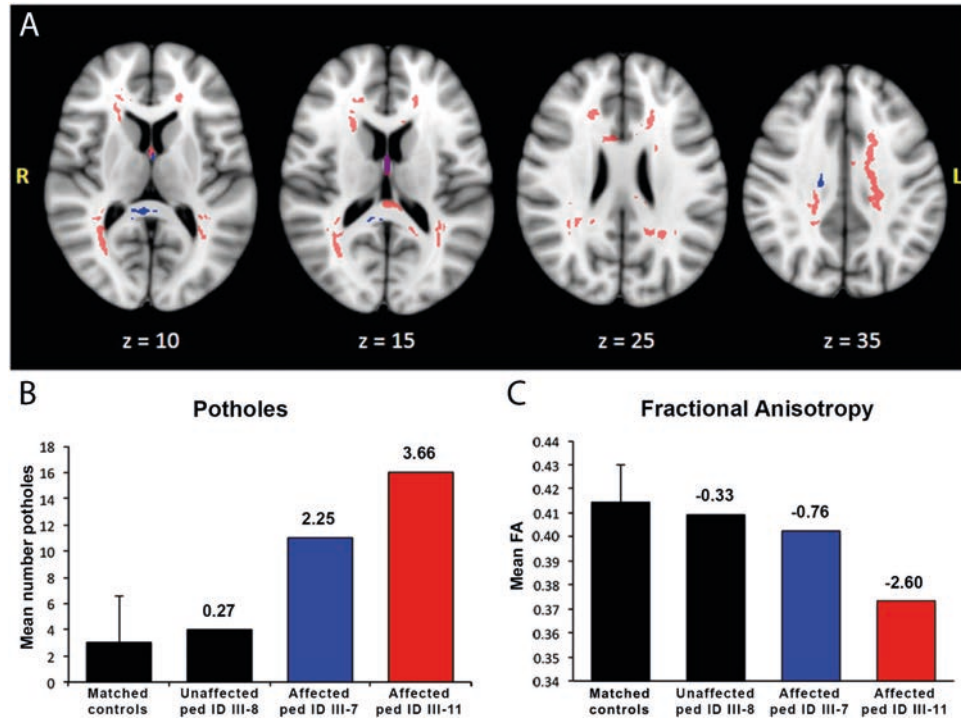


Figure 4.5 White matter abnormalities in *CSPG4*^{A131T} patients. **(A)** White matter potholes found in the two affected family members are shown in red and blue, respectively. Purple regions define a spatial overlap of potholes in both patients. The z-measures provide coordinates of the axial plane in MNI-space. **(B)** Mean number of potholes comparing the matched control population to the unaffected and two affected family members. **(C)** Whole-brain white matter fractional anisotropy (FA) comparing the matched general population subjects to unaffected and affected family members. Error bars in **B** and **C** reflect the standard deviation of the matched general population subjects. The number above each bar reflects the individual z-score compared to the matched general population group.

Discussion

Our findings provide convergent genetic and functional neurobiological evidence that oligodendrocyte progenitor cell dysfunction might influence the pathophysiology of schizophrenia. We identified two different rare missense mutations in *CSPG4* exhibiting familial segregation with schizophrenia. The discovery family *CSPG4*^{A131T} mutation was associated with abnormal protein processing, OPC morphology, cellular viability, and oligodendrogenesis. The second mutation (*CSPG4*^{V901G}), also located in a LamG domain, segregated with schizophrenia in two independent pedigrees and exhibited nominally significant enrichment in the Swedish Schizophrenia Exome Sequencing Study¹⁷⁸. Moreover, induced expression of *CSPG4*^{A131T} and *CSPG4*^{V901G} isoforms confirmed the likely pathogenicity of these mutations for OPC function. Importantly, however, our findings leave still unaddressed the question of the extent to which there are distinct vs. shared pathophysiological mechanisms in schizophrenia attributable to common polygenic risk, CNVs or other familial variants.

Our genetic findings highlight some of the challenges frequently encountered in the effort to identify pathogenic rare variants underlying common diseases such as schizophrenia. Although we identified three independent families exhibiting segregation of two different rare *CSPG4* missense variants with complete penetrance, none of these families was large enough on its own to achieve a genome-wide significant LOD score. Moreover, although the rare MAF of the *CSPG4*^{A131T} mutation precluded case/control validation in the Swedish Schizophrenia Exome Sequencing Study, two of the three *CSPG4*^{A131T} mutation carriers in the general population Rotterdam Study cohort had a clinically significant history of psychiatric illness that was unlikely due to chance. Furthermore, the *CSPG4*^{V901G} mutation was present in the Swedish cohort with a nominally significant enrichment in cases versus controls. Additional follow-up studies in larger cohorts will be required to definitively evaluate the association between schizophrenia and rare *CSPG4* variants.

Genetic variation in *CSPG4* might confer a pleiotropic risk for mental illness since two of the *CSPG4*^{A131T} mutation carriers identified in the general population Rotterdam Study cohort had a clinically significant history of depression. Interestingly, a mouse model of OPC depletion was recently shown to exhibit depression-like behavior²²⁴. Such pleiotropic influences on mental health outcomes would be consistent with many of the previously identified genetic risk factors for schizophrenia^{225,226}. Furthermore, originally named as melanoma-associated chondroitin sulfate proteoglycan upon its cloning²²⁷, NG2/*CSPG4* has since been widely implicated in a wide variety of human cancers both as a diagnostic marker and a therapeutic target, including for glioblastoma and melanoma^{228,229}.

The protein sequence surrounding the *CSPG4*^{A131T} mutation is conserved only among higher-order primates, suggesting recent evolutionary pressure. In contrast, the *CSPG4*^{V901G}

variant is predicted to be a disease-causing mutation by PolyPhen2²³⁰. In non-primate vertebrates, the reference amino acid at position 131 is threonine, corresponding to the patient mutation *CSPG4*^{A131T} and contributing to a benign PolyPhen score. Interestingly, this is analogous to the human *SNCA*^{A53T} mutation, one of the most well established mutations for autosomal dominant Parkinson's Disease²³¹. In mice, the reference amino acid at *SCNA* position 53 is a threonine. But notably, although transgenic expression in mice of the reference human *SCNA* sequence is benign, introduction of the human *SNCA*^{A53T} mutation is highly pathogenic²³¹.

To investigate the cellular pathophysiology resulting from mutation of *CSPG4*, we derived iPSCs from affected and unaffected siblings of the discovery family. Detailed electrophysiological analysis of patient-derived neurons revealed an increase in input resistance and depolarized shift in AP threshold. Multiple previous studies have demonstrated primary functional neuronal mechanisms in human iPSC models of schizophrenia^{34,173,178,181,182,232}; however, the changes we observed are distinct from those previously identified. Therefore, future studies will be required to determine the extent to which these differences may have pathophysiological relevance, and potentially reflect an increased burden of common polygenic risk as recently observed in familial schizophrenia²³³. Importantly, however, our limited findings in neurons compared to OPCs cannot be considered to imply that neuronal dysfunction is not central to the pathophysiology of schizophrenia. Rather, these data suggest that although the symptoms of schizophrenia are ultimately manifest from neuronal dysfunction, the primary pathophysiological mechanism could be mediated by direct neuronal impairments and/or indirectly through non-neuronal cell types including OPCs, depending upon the nature of the etiological factors driving disease risk in a given individual.

OPCs receive extensive GABAergic input from surrounding neurons, which regulate their differentiation to myelinating oligodendrocytes^{234–237}. However, it has remained less well understood whether OPCs directly modulate neuronal function independent of myelination. Notably, two recent studies have suggested novel candidate mechanisms by which OPC dysfunction might directly regulate neuronal function, including activity-dependent ecto-domain cleavage of NG2²¹⁶ and local buffering of extracellular potassium²³⁸.

Regarding the identified *CSPG4* mutations demonstrating familial segregation with schizophrenia, alterations in myelination are a parsimonious candidate mechanism given the convergent findings of genetic mutations in the OPC marker protein *CSPG4*, functional impairments of iPSC-derived OPCs, and *in vivo* DTI-based structural brain imaging. Moreover, the abnormal subcellular localization of NG2 in OPCs expressing the *CSPG4*^{A131T} or *CSPG4*^{V901G} isoforms is consistent with the high susceptibility of cells of the oligodendrocyte lineage to disruptions in the secretory pathway, as their maturation requires a substantial upregulation of membrane protein expression²³⁹. Interestingly, earlier work

has shown a precedent for altered subcellular localization of NG2, in which mutation of Ser999 results in an abrogation of chondroitin sulfate side chain modification and altered subcellular localization²¹⁷.

Taken together, these findings are highly consistent with the growing body of evidence implicating white matter integrity in schizophrenia neuropathology^{223,240–242}. Indeed, recent findings demonstrating myelination of parvalbumin-positive GABAergic interneurons – arguably the most well established neuronal cell type implicated in the pathophysiology of schizophrenia^{243,244} – raises the intriguing possibility that schizophrenia might result from neurodevelopmental alterations of PV interneuron myelination²⁴⁵.

In summary, our findings support the validity of family-based genetics and iPSC modeling to unravel the underlying mechanisms of complex, heterogeneous psychiatric diseases, and provide evidence in support of oligodendrocyte precursor cell dysfunction as a novel candidate mechanism of schizophrenia.

Materials and methods

Recruitment of family with schizophrenia and obtaining patient material

A Dutch white Caucasian non-consanguineous family with a high incidence of schizophrenia was ascertained. Written informed consent was obtained from all participating subjects. This study was approved by the medical ethical committee of the Erasmus University Medical Centre (Rotterdam, The Netherlands). Participating family members were screened for current or past psychiatric symptoms using the Structural Clinical Interview for DSM-IV (SCID-1)²⁴⁶. Medical screening revealed no evidence of somatic comorbidities, dysmorphologies, or neurological symptoms. All individuals with schizophrenia were documented to be of average intelligence at the time of their initial diagnosis. DNA isolation from venous blood samples and skin biopsies were performed using standard procedures. Two family members (II-2 and III-9) passed away since the start of the study.

For skin biopsies, a small area of skin of the medial aspect of the upper arm was anesthetized with an EMLA patch (AstraZeneca) for one hour, after which the skin was disinfected with ethanol and the biopsy was obtained through all skin layers with a standard 3mm biopsy punch. The tissue was collected in Dulbecco's Modified Eagle Medium (DMEM) (Gibco-Invitrogen) without additives and transferred to culture within 24 hours. Primary human fibroblasts were cultured in DMEM containing 10% fetal calf serum and 1% penicillin/streptomycin (P/S).

Genetic analysis

Genomic DNA was isolated using standard methodology from 14 family members, including 13 by whole blood samples and one subject (pedigree ID II-1) using paraffin-embedded tissue (**Figure 4.1A**). Linkage and Copy Number Analysis was performed with Illumina HumanCytoSNP-12v2 chip arrays (294,975 markers). Linkage analysis was conducted exclusively for the purpose of identifying a genome-wide set of candidate chromosomal regions shared by all affected family members (defined as those regions with a LOD score > 0). Linkage was performed using Allegro and implemented in the EasyLinkage version 5.08 interface²⁴⁷ with one marker every 0.5 cM using a co-dominant allele frequency algorithm and dominant scoring function. Unaffected family members were considered as having an unknown affection status in the linkage model, providing no *a priori* constraints on the rate of incomplete penetrance. Copy number analysis was performed using NEXUS discovery edition, version 6 (BioDiscovery, El Segundo, CA), which did not indicate the presence of copy number variants segregating with the phenotype. The strongest evidence of linkage was observed on chromosomes 2, 11, 14, 15, and 16, involving a total of 294.34 Mb of genomic loci.

Whole exome sequencing was performed on three individuals of the discovery family (pedigree IDs: II-2, III-5 and III-9). Sequencing was performed twice for all three samples: initially at 40x, and subsequently at 90x coverage. Exome sequencing was performed using in-solution capturing (Agilent SureSelect V2 and V4 Human 50 Mb kit respectively, Agilent Technologies) and paired-end sequencing with Illumina Hi-Seq 2000 sequencers. Reads were aligned to the human reference genome version 19 using Burrows-Wheeler Aligner. SNPs and indels were called using the Genome Analysis Toolkit (GATK).

The heterozygous variants were filtered based on the following criteria: a) present within the candidate genomic regions shared among all affected family members, b) predicted to affect protein coding (missense, nonsense, frameshift, splice site), c) called in at least one of the affected individuals [III-5 and III-9], d) absent from the unaffected mother [II-2], e) absent from dbSNP129, and f) with a minor allele frequency (MAF) of < 0.001 in the Exome Aggregation Consortium (ExAc) browser (European non-Finnish)¹⁹⁴, Exome Variant Server (EVS6500, NHLBI Exome Sequencing Project)¹⁹⁵, 1000 Genomes¹⁹⁶, and Genome of the Netherlands¹⁹⁷ cohorts.

Genotyping of *CSPG4* c.391G>A was performed in a cohort of Dutch subjects with 1219 schizophrenia cases and 10,611 controls. Genotyping of 763 schizophrenia cases and 386 healthy control subjects were performed using a custom Illumina Infinum Human Exome Beadchip array (Genetic Risk and Outcome of Psychosis [GROUP] / Utrecht cohort study²⁴⁸). TaqMan genotyping was performed on an additional 456 locally-collected schizophrenia cases and 10,225 population-based controls filtered for identity by descent ($\hat{\pi} < 0.25$) (Rotterdam Study¹⁹⁸). All samples with ALT calls by exome array or TaqMan genotyping were validated by Sanger sequencing, particularly given the existence of the *CSPG4P13* pseudogene with high homology to the region surrounding *CSPG4* c.391G>A (**Supplementary Figure 4.7**).

Taqman genotyping of *CSPG4* c.391G>A was performed with the following primers and probes: F_GGCTGGTTCCCCTCAGGTA, R_GTGGTGCTGACTGTCGTAGAG, VIC_TTTCTGAACGCCTCCTC, FAM_TTTCTGAACACCTCCTC. The following primer sets were used for Sanger sequencing of *CSPG4* c.391G>A: F_TCTGGGGCCCCAAGTGTGG and R_AGAGTGGGGCCCAGAGAAGC, with an internal forward primer for sequencing: Fseq_GGGCCAGGAGGAGCTGAGG. A second primer set was used for confirmation: F2_CCACTCCCCATCTCTTTCAGG and R2_CAGGGCCACATCACTGG. *CSPG4P13* pseudogene-specific amplification was performed using the following primers: F_CTCTGGGGCACCAAGAGTGG and R_AGAGTGGGGCCCAGAGAAGC.

Structural homology modeling

Homology modeling of the first Laminin G domain (amino acids 29-176) was performed independently using both the Protein Homology/analogY Recognition Engine – Version 2.0 (Phyre2)²⁰⁷ and Iterative Threading ASSEmbly Refinement (I-TASSER)²⁰⁸ protein structure prediction servers. All 148 residues (100%) of the reference and mutant sequences were modeled at >99% confidence by Phyre2 using intensive mode. For I-TASSER, the confidence (C-score) was 0.81 and topological similarity (TM-score) was 0.82 \pm 0.08, for both models. Reference and mutant models were structurally aligned with PyMol (<http://www.pymol.org>).

Generation and characterization of iPSCs

Reprogramming of human primary skin fibroblasts was performed as previously described²⁴⁹. Briefly, fibroblasts were infected with a multicistronic SIN lentiviral vector containing an SFV promoter, encoding OCT4, SOX2, KLF4 and MYC, as well as dTomato to visualize reprogramming. Emerging iPSC colonies were cultured on γ -irradiated mouse embryonic fibroblasts. All iPSC lines and their derivatives used in this study were screened monthly for mycoplasma.

Characterization of iPSC clones was performed by RT-PCR (**Supplementary Figure 4.2A**), immunostaining for un-differentiated human ES markers (**Supplementary Figure 4.2B**) and markers of three embryonal germ layers on embryoid bodies (EBs) differentiated *in vitro* (**Supplementary Figure 4.2C**). Total RNA of iPSCs was isolated for RT-PCR using standard protocols (primers listed in **Supplementary Table 4.5**). For EB differentiation, iPSC colonies were dissociated by collagenase IV treatment and transferred to ultra-low attachment 6-well plates (Corning). Floating EBs were cultured in iPSC medium without bFGF for a minimum of 6 days with supplemented SB431542 (Tocris Bioscience) for ectoderm conditions only. EBs designated for endoderm differentiation were transferred to gelatin-coated 12-well plates containing the following medium: RPMI 1640 (Gibco-Invitrogen), supplemented with 20% FBS, 1% P/S, 1% glutamine and 0.4mM alpha-thioglycerol. Mesoderm differentiation from the EBs was induced in gelatin-coated 12-well-plates with DMEM medium (low glucose) supplemented with 15% fetal bovine serum, 1% P/S, 1% glutamine and 1% MEM-non-essential amino acids. Ectoderm differentiation was induced in Matrigel (BD)-coated plates with the following medium: neurobasal medium (Gibco-Invitrogen) and DMEM/F12 (v/v 50/50) supplemented with 1% P/S, 1% glutamine, 1% MEM-non-essential amino acids, 0.02% BSA (Gibco-Invitrogen), 0.5% N2 (Gibco-Invitrogen) and 1% B27 (Gibco-Invitrogen). After two weeks in culture, cells were fixed with 4% formalin for immunolabeling.

iPSCs were cultured in standard human embryonic stem (hES) cell culture medium containing DMEM/F12 (Gibco-Invitrogen) supplemented with 20% knock-out serum replacement (Gibco-Invitrogen), 2mM L-glutamine (Gibco-Invitrogen), 1% P/S (Gibco-Invitrogen), 1% MEM-non-essential amino acids (PAA Laboratories GmbH), 0.1mM β -mercapto-ethanol,

and 10 ng/ml bFGF (Gibco-Invitrogen). Medium was replenished daily and colonies were passaged weekly using collagenase IV (1 mg/ml, Gibco-Invitrogen) with 10 μ M ROCK inhibitor (Y-27632, Sigma).

Karyotype analysis

iPSCs were dissociated to single-cell suspension using TrypLE Express (Gibco-Invitrogen) and plated feeder-free in mTeSR1 medium on three Matrigel-coated wells of a 6-well plate in the presence of 10 μ M ROCK inhibitor. The next day, cells were harvested using TrypLE Express, treated with colcemid (200 ng/ml) and hypotonic solution, and fixed using Carnoy's Fixative. At least 20 metaphases were analysed for each clone, for which the chromosome count was considered normal if more than 70% of cells analysed had 46 chromosomes. More detailed karyotypic analysis with RBA and QFQ band analysis was performed for one individual patient clone (individual III-11) to further exclude segregating cytogenetic abnormalities (**Supplementary Figure 4.2D**).

Neuronal differentiation

iPSC colonies were dissociated from MEFs with collagenase IV and transferred to non-adherent plates in hES cell medium on a shaker in an incubator at 37°C/5% CO₂. After two days, EBs were changed to neural induction medium [DMEM/F12, 1% N2-supplement (Gibco-Invitrogen), 2 μ g/ml heparin (Sigma), 1% P/S] and cultured for another four days in suspension. EBs were gently dissociated and plated onto laminin-coated dishes in neural induction medium. Cells were dissociated with collagenase IV after 8 days and plated onto laminin-coated dishes in NPC medium [DMEM/F12, 1% N2, 2% B27-RA, 1 μ g/ml laminin (Sigma) and 20 ng/ml FGF₂ (Millipore), 1% P/S]. After one week, NPCs were dissociated with collagenase IV, re-plated, and passaged 1:4 weekly. For neural differentiation, passage 5 NPCs were plated on coverslips coated with 100 μ g/ml poly-L-ornithine (Sigma) and 50 μ g/ml laminin in neural differentiation medium consisting of Neurobasal medium supplemented with 1% MEM-non-essential amino acids, 1% N2 supplement, 2% B27-RA supplement, 20 ng/ml BDNF (ProSpecBio), 20 ng/ml GDNF (ProSpecBio), 1 μ M db-cAMP (Gibco-Invitrogen), 200 μ M ascorbic acid (Gibco-Invitrogen), 2 μ g/ml laminin and 1% P/S.

Electrophysiological recordings

After 8-10 weeks of neuronal differentiation, culture slides were transferred to the recording chamber following a thirty-minute serial partial exchange of cell culture medium with artificial cerebrospinal fluid (ACSF) containing the following (in mM): 110 NaCl, 2.5 KCl, 2 CaCl₂, 2 MgCl₂, 1 NaH₂PO₄, 25 NaHCO₃, 10 glucose, 0.2 ascorbate (pH 7.4). In the recording chamber, slides were continuously perfused with ACSF at 1.5-2 mL/min, saturated with 95% O₂/5% CO₂ and maintained at 20-22°C.

Whole-cell patch-clamp recordings were performed under infrared differential interference contrast visual guidance using an upright microscope (Zeiss) with borosilicate glass recording micropipettes (3-6 M Ω) filled with the following medium (in mM): 130 K-gluconate, 11 KCl, 10 HEPES, 5 NaCl, 0.1 EGTA, 1 MgCl₂, 2 Mg-ATP, 0.3 Na-GTP, 5 phosphocreatine (pH 7.4). Data were acquired at 10 kHz using an Axon Multiclamp 700B amplifier (Molecular Devices), filtered at 3 kHz, and analyzed using pClamp 10.1 (Molecular Devices). Whole-cell capacitance and series resistance were compensated, and voltage was adjusted for liquid junction potential.

Current-clamp recordings were performed at a holding potential of -60 mV. Passive membrane properties were analysed using a series of hyperpolarizing and depolarizing square wave currents (500 msec duration, 1 sec interstimulus interval) in 5 pA steps, ranging from -20 to +30 pA. AP amplitude, rise time, decay time and half width were measured for the first evoked AP resulted by a depolarizing step, from the threshold to the peak, for which the threshold was defined by the moment at which the second derivative of the voltage exceeded the baseline. Spontaneous APs were recorded at resting membrane potential. Voltage-clamp recordings were performed at a holding potential of -90 mV.

Oligodendrocyte lineage differentiation

iPSC-derived NPCs were differentiated to OPCs according to Monaco *et al*²⁵⁰, with modifications. NPCs were plated on laminin-coated 10 cm plates in NPC medium consisting of DMEM/F12, 1% N2, 2% B27-RA, 1 μ g/ml laminin, 1% P/S, 25 ng/ml basic Fibroblast Growth Factor (bFGF) and 20 ng/ml Epidermal Growth Factor (EGF). When NPCs reached 90% confluence, NPC medium was changed to OPC differentiation medium for three weeks: DMEM/HAMS F12, 1% N2, 1% BSA, 1% L-Glutamine, 1% P/S, 20 ng/ml bFGF, 10 ng/ml platelet derived growth factor (PDGF-AA, ProspeBio), 2ng/ml Sonic hedgehog (Shh), 2 ng/ml neurotrophic factor 3 (NT-3) and 3 nM triiodothyronine (T3). OPC medium was changed every other day, and cells were passaged weekly at 1:4.

Surface Biotinylation

Biotinylation of cell surface proteins was adapted from Huang *et al*²⁵¹, with modifications. First, the OPCs were washed twice in cold PBS/CaCl₂/MgCl₂ (2.5 mM CaCl₂, 1 mM MgCl₂, pH 7.4). Then, the OPCs were incubated for 15 minutes on ice with or without 0.3 mg/ml of freshly dissolved Sulfo-NHS-SS-Biotin (Thermo Scientific) in PBS/CaCl₂/MgCl₂. Next, the OPCs were washed three times on ice in cold biotin quenching solution consisting of 50 mM glycine in PBS/CaCl₂/MgCl₂. Subsequently, the OPCs were lysed by incubation for 10 minutes on ice with lysis buffer, pH 7.4, consisting of 5 mM EDTA, 5 mM EGTA, 1% Phosphatase inhibitor cocktail 2 and 3 (Sigma), 1% PIC (Sigma), and 1% Triton X in PBS. At least 3 wells were pooled from each cell line at each experimental condition, to minimize

any plating or growing variability in the cell culture. A portion of the lysate was removed and labeled as the total fraction (whole cell lysate). The remaining lysate was then centrifuged (13200 rpm at 4°C for 15 minutes) to remove insoluble proteins. The supernatants were incubated overnight at 4°C with PBS-washed and lysis buffer-equilibrated Pierce™ NeutrAvidin™ Agarose beads (Life Technologies). Next, the mixture was spun down at 2000 rpm, separating the supernatant termed the intracellular fraction from the surface protein fraction attached to the beads. Subsequently, the beads were washed four times by rotating with lysis buffer and after the final wash the beads were dried completely and taken up in 20 µl of lysis buffer, labeled as the surface fraction.

Sodium dodecyl sulfate (SDS)-PAGE and Western Blotting

First, 25% XT Sample Buffer (Biorad) and 10% 100mM dithiothreitol (DTT) were added to equal volumes of cell extract followed by heating to 65°C for 15 minutes. Then, the samples were electrophoresed through 4%-12% Criterion™ XT Bis-Tris gradient gels (Biorad) in XT-Mops buffer (Biorad). Proteins were transferred overnight at 4°C on 0.45 µm pore nitrocellulose membrane (Biorad) in a Tris-Glycine buffer consisting of 10% Tris/Glycine buffer (Biorad) and 20% anhydrous methanol in distilled water. Membranes were blocked for 2 hours while shaking at room temperature in TBST buffer containing 4% blotting grade blocker (Biorad). Then, the membranes were incubated with a monoclonal antibody generated from hybridoma B5 cells raised against purified intact NG2 protein from melanoma cells (generous gift from W.B. Stallcup) and mouse anti-actin (Sigma) in TBST buffer containing 1% Tween and 2% milk for 48 hours at 4°C followed by washing with TBST buffer. Finally, the blots were incubated with IRDye® secondary antibodies (LI-COR) against the primary antibody species for two hours at room temperature. The blots were washed twice in TBST and TBS followed by one wash in water, subsequently the antibody fluorescence was visualized using an ODYSSEY® CLx scanner (LI-COR). Quantification of NG2 western blot bands was performed using ImageJ software (<http://imagej.nih.gov/ij/>).

Shiverer co-culture assay

Experiments were approved by the Dutch Ethical Committee and in accordance with the Institutional Animal Care and Use Committee (IACUC) guidelines. *Shiverer* mice (*C3Fe. SWV-Mbp^{shi}*, Jackson Laboratory) were backcrossed >10 generations into *C57BL/6J*. Organotypic cortex slices were established from homozygous shiverer (*Mbp^{shi/shi}*) mice at P3-P5 according to Stoppini *et al.*²⁵², with modifications. Briefly, the brain rapidly removed and transferred to ice cold Gey's Balanced Salt Solution (Sigma) containing 5.4 mg/ml glucose and 1% P/S. After dividing the brain sagittally into two hemispheres, 300 µm fronto-parietal coronal slices were obtained using a tissue chopper (McIlwain). Slices were cultured on an air-fluid interface at 37°C with 5% CO₂, using culture plate inserts (Millipore: 0.4 µm pore size; 30 mm diameter; 3 cultures per insert) in 1.0 mL culture medium containing 50% MEM alpha, 25% HBSS, 25% horse serum, 6.5 mg/mL glucose, 2 mM glutamine,

1% N2 supplement and 1% P/S, supplemented with PDGF-AA. For each *Mbp^{shi/shi}* mouse, adjacent slices were randomly assigned for transplantation with either patient or control OPCs, thereby providing comparative matched pairs. Each slice was transplanted with 1×10^4 iPSC-derived OPCs in 1.0 μ L PBS containing 0.1% FastGreen (Gibco-Invitrogen) using a Picospritzer. OPCs were allowed to differentiate into myelinating oligodendrocytes for 10 days, following the procedure described in Najm *et al*²².

Immunocytochemistry and confocal imaging

Cell cultures and organotypic slices were fixed using 4% formalin in PBS. Primary antibodies were incubated overnight at 4°C in labeling buffer containing 0.05 M Tris, 0.9% NaCl, 0.25% gelatin, and 0.5% Triton-X-100 (pH 7.4). The following primary antibodies were used: SOX2 (AB5603), Nestin (MAB5326), MAP2 (AB5622), NeuN (MAB377), GFAP (AB5804), human Nuclear Antigen (hNA, MAB1281) [Millipore], FOXG1 (45-053) [ProSci], NG2-EC [kindly provided by W.B. Stallcup], Olig2 (AB42453), MBP (AB7349) [Abcam], Vimentin (SC6260) [Santa Cruz Biotechnology], AFP (MAB1368), SOX10 (AF2864) [R&D Systems], TRA-1-81 (560072), Nanog (560482) [Beckton Dickinson], OCT4 (AB19857) [Abcam], Calreticulin (PA3-900) [Fisher Scientific]. The following secondary antibodies were used: Alexa-488, Alexa-546, Alexa-555 and Cy3 antibodies [Jackson ImmunoResearch]. Samples were imbedded in Mowiol 4-88 (Fluka) after which confocal imaging was performed with a Zeiss LSM700 confocal microscope (Apochromatic 40x objective, 1.3 NA, oil immersion) using ZEN software (Zeiss, Germany).

Experimenters were blinded to group allocation when performing experiments, during data collection, and when assessing outcomes. OPC area (μm^2) was quantified on maximum projection of z-stack images covering the full depth of each measured cell using a manually drawn surface contour in ImageJ. Quantification of human nuclei (hNA) and myelin (MBP) content of organotypic cortex slices was performed using Image J. Maximum intensity projections of tiled z-stacks covering the full dimensions of each slice with a constant interval of 1.0 μm were converted to individual 8-bit threshold images. Human nuclei (hNA) images were further segmented using a binary watershed filter. The number and surface area of labelled cells were quantified using the particle analysis algorithm. Cell viability was measured using resazurin (AlamarBlue, Thermo Fisher Scientific) in 96-well plates. Fluorimetric data were collected using a plate reader at a wavelength of 570 nm excitation and 585 nm peak emission. The data were normalised for the number of living cells using calcein AM (Thermo Fisher Scientific) at 488 nm excitation and 517 nm peak emission and quantified in adjacent wells seeded concurrently with equal numbers (2000 cells/well).

Plasmid Transfections

Control OPCs and U373 glioma cells were transfected with cDNA constructs to express fusion proteins of CSPG4 and its mutant variants with C-terminal EGFP. *CSPG4* cDNA sequence (*CSPG4^{WT}*) was cloned into the Gateway vector pcDNA-DEST47 (pcDNA-DEST47-*CSPG4^{WT}*) and converted to *CSPG4^{A131T}* by site-directed mutagenesis. The corresponding plasmid containing the *CSPG4^{V901G}* sequence was obtained by sub-cloning a custom-ordered V901G-containing fragment (GeneArt, Thermo Fisher Scientific) into the pcDNA-DEST47-*CSPG4^{WT}* vector. All three plasmids were confirmed by sequencing. OPCs were transfected with *CSPG4^{WT}-EGFP*, *CSPG4^{A131T}-EGFP*, or *CSPG4^{V901G}-EGFP* using X-TremeGENE transfection reagent (Sigma-Aldrich) with 0.1 µg DNA per 96-well, or 1.0 µg DNA per 12-well. Cells were fixed 48 hours after transfection.

Magnetic Resonance Imaging (MRI)

Two patients and two control siblings of the discovery family provided additional written informed consent for MRI scanning. One of the unaffected siblings was excluded due to a history of systemic chemotherapy known to influence white matter integrity²⁵³. Population controls (n=294) were selected from the Rotterdam Study based on matching for age, gender, smoking behavior, and alcohol use. All subjects, including population controls and family members, were imaged using the identical MRI scanner and acquisition protocol.

MRI images were obtained using a 1.5 Tesla General Electric scanner (GE Healthcare, Milwaukee, Wisconsin, USA, software version 11X), with a bilateral phased-array head coil. A full description of the imaging protocol has been described previously²⁵⁴. Diffusion-weighted imaging was performed using echo planar imaging (EPI) sequences collected in 25 directions with a b value of 1,000 s/mm² and three b = 0 images. Additional sequence parameters were TR = 8,000 ms, TE = 74.6 ms, bandwidth 14.71 kHz, flip angle = 13°, acceleration of 2, and a voxel resolution of 3.3 x 2.2 x 3.5 mm³.

Pre-processing of the diffusion-weighted images was performed using FSL²⁵⁵. After conversion from dicom to nifti format, individual images were eddy-current corrected using FMRIB's eddy_correct²⁵⁵ followed by skull stripping using BET²⁵⁶. Fractional anisotropy (FA) images were created by fitting a tensor model to the diffusion data using FMRIB's Diffusion Toolbox (FDT)²⁵⁵. All subjects' FA data were then aligned into common space using the nonlinear registration tool FNIRT²⁵⁷, which employs a b-spline representation of the registration warp field²⁵⁸. Whole brain mean FA was calculated by masking each image using the Johns Hopkins University White Matter Atlas (JHU WMA)²⁵⁹ and determining the mean intensity of FA within the mask.

An in-house MATLAB (Mathworks, Natick, MA) algorithm was used to quantify the number and spatial characteristics of white matter 'potholes' along the major white matter tracts²⁶⁰.

The input to the algorithm was the set of FA images that had undergone non-linear registration into MNI space using TBSS²⁶¹. No spatial filtering was applied to the images. The first step was to generate a voxel-by-voxel mean and standard deviation (SD) image of the 294 matched population controls. These group and SD images were then used to individually create a voxel-wide z-image for all of the subjects, including the three family members. This resulted in individual z-images with each voxel based on the mean and SD of the matched population controls. To ensure the search involved only white matter regions, each image was masked with the cortical areas defined by the Johns Hopkins University white matter atlas²⁵⁹.

The individual z-FA images were then used to search for contiguous voxels of white matter below a threshold of $z < -2^{223,260}$. Clusters were determined by thresholding each image and labeling contiguous voxels in three-dimensional space that fell below the defined threshold. Only clusters greater than 250 voxels were used in the analyses.

Statistical Analysis

Significance of observations was established for genetic case-control analyses using the Fisher's exact test. Brain imaging results in family members were evaluated using z-scores based on the matched population control cohort distribution. For functional studies, statistical comparisons were performed using two-tailed t-test, analysis of variance (ANOVA), or Kolmogorov-Smirnov test, as indicated. Data are expressed as mean \pm S.E.M., unless otherwise specified. The threshold for significance was set at $P < 0.05$ for all statistical comparisons.

Conflict of interest

The authors declare no conflicts of interest.

Acknowledgements: We wish to thank Roel Ophoff for facilitating the contribution of the GROUP/Utrecht Study samples and discussions regarding the genetic analyses, Gerard Borst for discussions regarding the electrophysiological analyses, and Siska Verploegh for her assistance in sample collection. This project was partially funded by the Erasmus MC – University Medical Centre Rotterdam, the Netherlands Organization for Scientific Research (NWO) and Netherlands Organisation for Health Research and Development (ZonMW) to S.A.K, V.B., Y.E. and J.G., the NeuroBasic-PharmaPhenomics consortium to S.A.K. and Y.E., Stichting ParkinsonFonds (The Netherlands) to V.B., Netherlands Institute for Regenerative Medicine (NIRM) and European Research Council (Consolidator Grant) to J.G.

The authors would like to thank the NHLBI GO Exome Sequencing Project and its ongoing studies which produced and provided exome variant calls for comparison: the Lung GO Sequencing Project (HL-102923), the WHI Sequencing Project (HL-102924), the Broad GO Sequencing Project (HL-102925), the Seattle GO Sequencing Project (HL-102926) and the Heart GO Sequencing Project (HL-103010).

This study makes use of data generated by the Genome of the Netherlands Project. A full list of the investigators is available from www.nlgenome.nl. Funding for the project was provided by the Netherlands Organization for Scientific Research under award number 184021007, dated July 9, 2009 and made available as a Rainbow Project of the Biobanking and Biomolecular Research Infrastructure Netherlands (BBMRI-NL). The sequencing was carried out in collaboration with the Beijing Institute for Genomics (BGI).

The generation and management of genomics data for the Rotterdam Study were supported by the Netherlands Organisation of Scientific Research Investments (nr. 175.010.2005.011, 911-03-012) and the Netherlands Genomics Initiative (NGI) project nr. 050-060-810 (Netherlands Consortium for Healthy Ageing; NCHA). We thank the members of the Human Genomics Facility (HuGeF) and the ERGO support team for their help in sampling the data and in creating the database. The Rotterdam Study is funded by Erasmus Medical Centre and Erasmus University, Rotterdam, Netherlands Organisation for Health Research and Development (ZonMw), the Research Institute for Diseases in the Elderly (RIDE), the Ministry of Education, Culture and Science, the Ministry for Health, Welfare and Sports, the European Commission (DG XII), and the Municipality of Rotterdam. The authors are grateful to the study participants, the staff from the Rotterdam Study and the participating general practitioners and pharmacists.

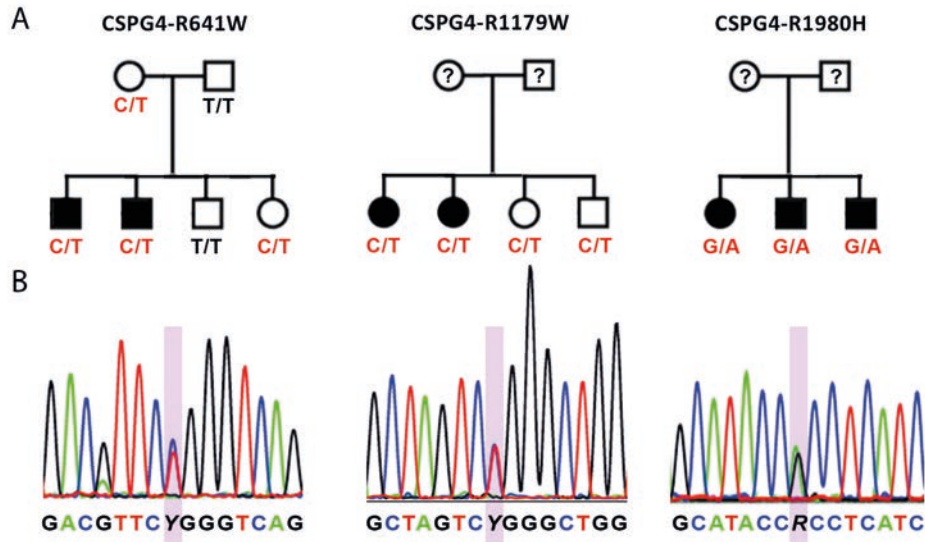
NIMH Study 13 -- Data used in this research report were collected by the International Neuro-Genetics Association of Spanish America and the United States (INGASU), and funded by a collaborative NIMH grant (Genetics of Schizophrenia in Latino Populations) to Dr. Michael Escamilla (University of Texas Health Science Center at San Antonio) (MH60881)

and to Dr. Ricardo Mendoza (University of California at Los Angeles-Harbor) (MH60875). Additional principal investigators who participated in these grants were Dr. Henriette Raventos (University of Costa Rica, San Jose, Costa Rica), Dr. Alfonso Ontiveros (Instituto de Informacion de Investigacion en Salud Mental, Monterrey, Mexico), Dr. Humberto Nicolini (Medical and Family Research Group, Carracci S.C., Mexico City, Mexico), Dr. Rodrigo Munoz (Family Health Centers of San Diego, California), and Dr. Alvaro Jerez (Centro Internacional de Trastornos Afectivos y de la Conducta Adictiva-CITACA, Guatemala). Additional investigators from the University of Texas Health Science Center at San Antonio included Dr. Albana Dassori and Dr. Rolando Medina.

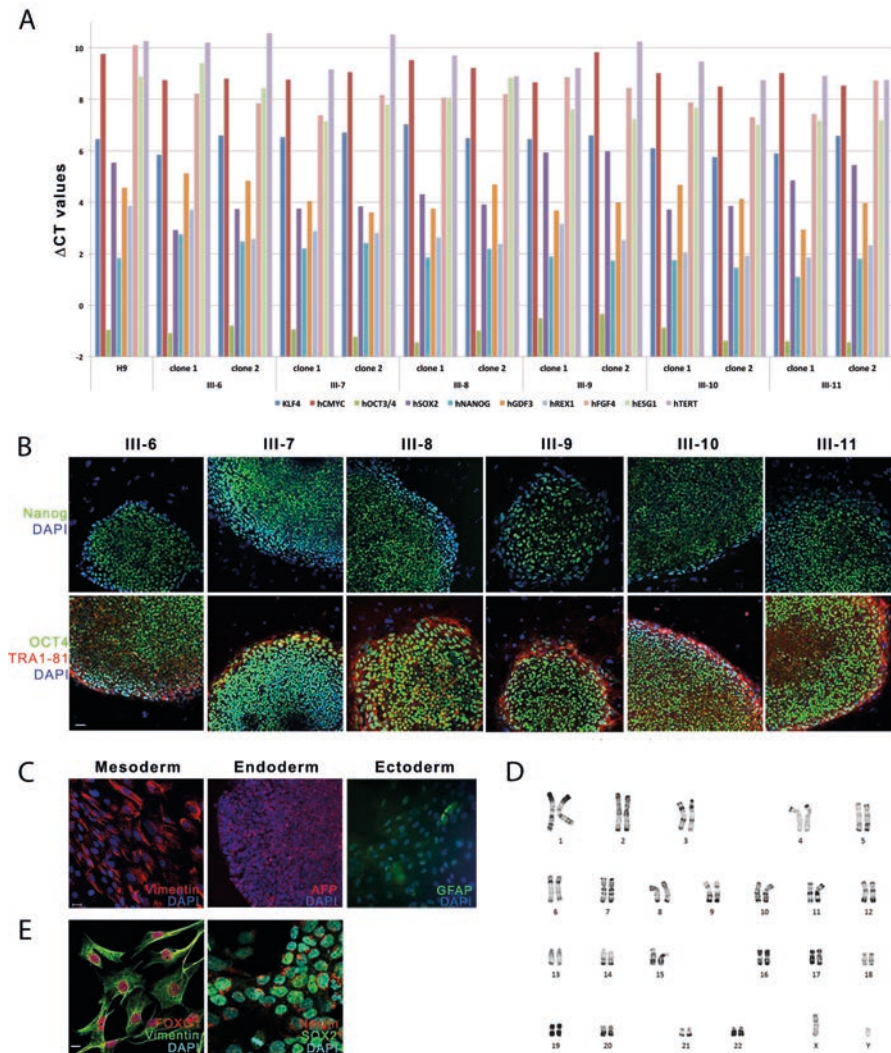
Swedish Schizophrenia Exome Sequencing project: Data obtained from dbGaP at <http://www.ncbi.nlm.nih.gov/gap> through dbGaP accession number [20 September 2015, accession phs000473.v1.p1]. Samples used for data analysis were provided by the Swedish Cohort Collection supported by the NIMH grant R01MH077139, the Sylvan C. Herman Foundation, the Stanley Medical Research Institute and The Swedish Research Council (grants 2009-4959 and 2011-4659). Support for the exome sequencing was provided by the NIMH Grand Opportunity grant RCMH089905, the Sylvan C. Herman Foundation, a grant from the Stanley Medical Research Institute and multiple gifts to the Stanley Center for Psychiatric Research at the Broad Institute of MIT and Harvard.

The authors would like to thank the Exome Aggregation Consortium and the groups that provided exome variant data for comparison. A full list of contributing groups can be found at <http://exac.broadinstitute.org/about>.

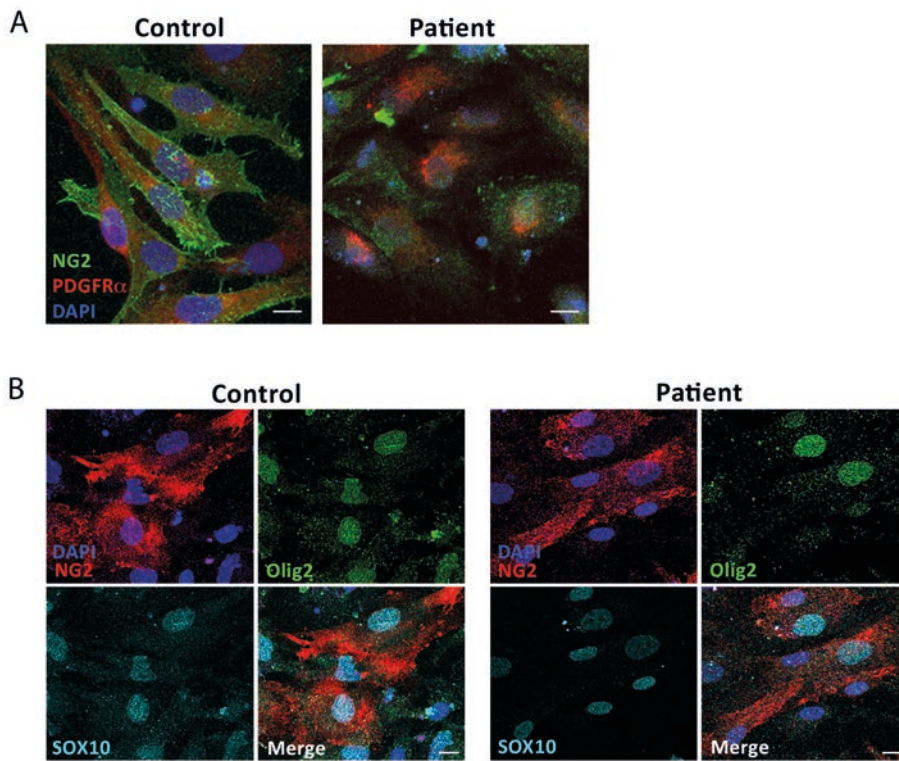
Supplementary Figures



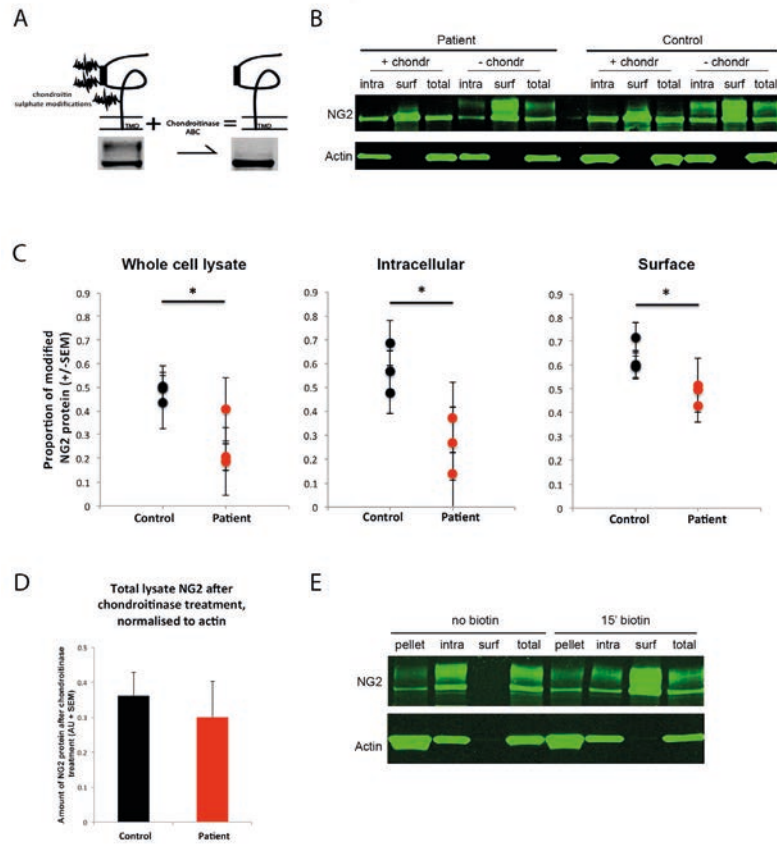
Supplementary Figure 4.1 Additional rare coding variants in *CSPG4*. (A) Pedigrees with *CSPG4*^{R641W}, *CSPG4*^{R1179W}, and *CSPG4*^{R1980H} variants. Symbols: filled, schizophrenia; open, unaffected; heterozygous carriers of the *CSPG4* c.1921C>T p.R641W, c.3535 C>T p.R1179W, and c.5939 G>A p.R1980H. (b) Representative sequencing results for heterozygous carriers of the corresponding *CSPG4* mutations in panel A.



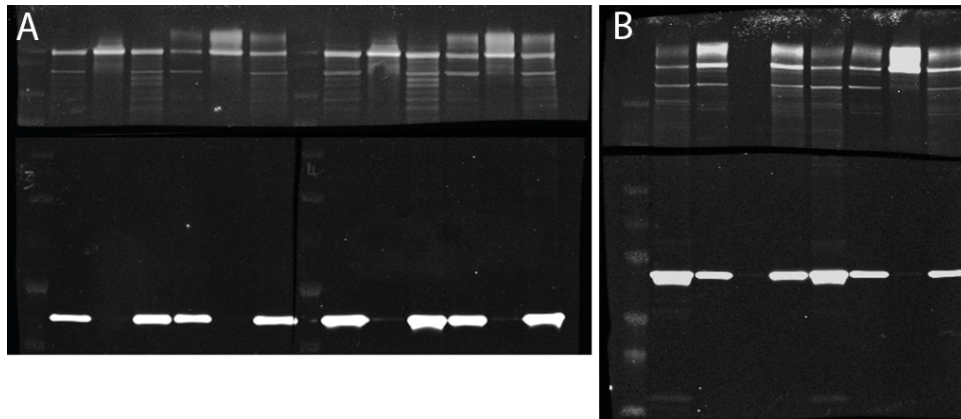
Supplementary Figure 4.2 Characterization of iPSC clones and NPCs. **(A)** RT-PCR of pluripotency genes normalized to GAPDH expression levels confirmed down-regulation of exogenous reprogramming genes and up-regulation of endogenous stem cell genes, similar to H9 human embryonic stem cells. **(B)** iPSC colonies showed uniform staining for pluripotency markers Nanog, OCT4 and TRA1-81. **(C)** EB differentiation confirmed that iPSCs were capable of generating representative cell types of all 3 embryonic layers – endoderm (AFP), mesoderm (Vimentin) and ectoderm (GFAP) (scale bar = 20 μ m). **(D)** Karyotyping was performed on all iPSC clones to confirm genomic integrity following reprogramming. Shown is a representative karyogram from the iPSC line of subject III-11. **(E)** NPCs were positive for SOX2, Nestin, Vimentin and FOXG1, confirming their forebrain specification (scale bar = 10 μ m).



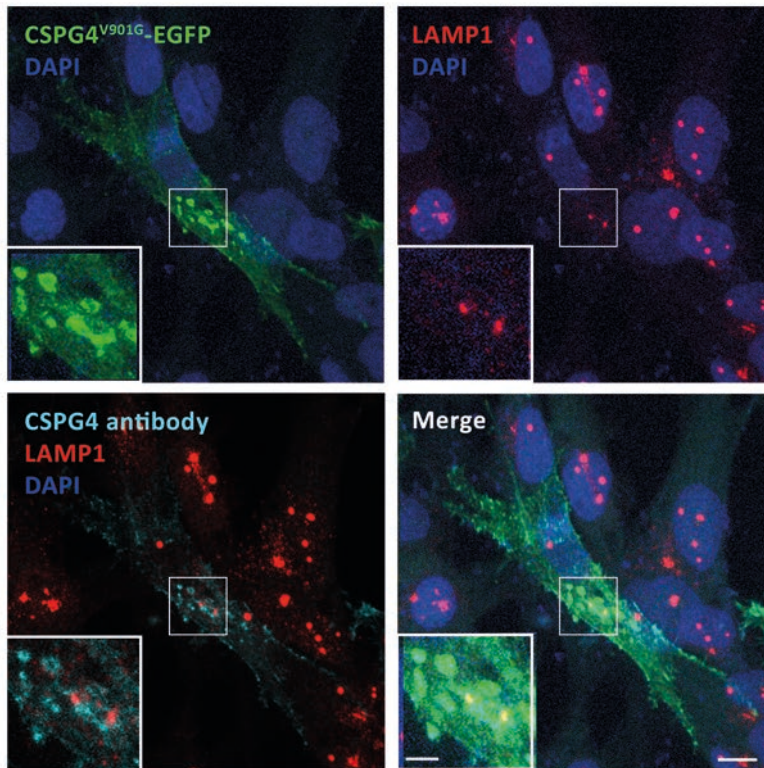
Supplementary Figure 4.3 Characterization of OPCs. NG2⁺ cells co-expressed the OPC markers PDGFR α (**A**), Olig2 and SOX10 (**B**) (scale bars = 15 μ m).



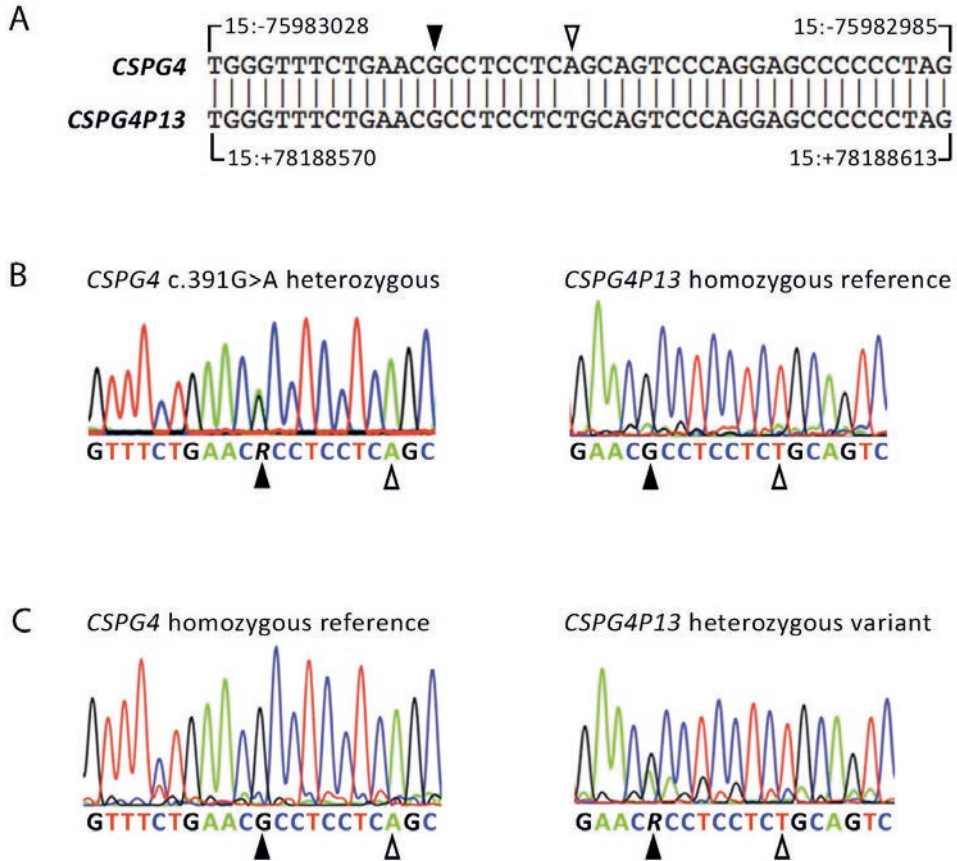
Supplementary Figure 4.4 Aberrant post-translational chondroitin sulphate modification in CSPG4^{A131T} patient-derived OPCs. **(A)** Chondroitin sulphate side chains are specifically cleaved by chondroitinase treatment. **(B)** Representative western blot of biotinylation assay samples of control and patient OPCs +/- chondroitinase ABC treatment (intra = intracellular fraction, surf = surface fraction, total = whole cell lysate fraction). **(C)** Quantification of the proportion of chondroitin sulphate-modified NG2 protein. The proportion of modified to unmodified NG2 in OPC extracts was determined by normalizing the integrated density of modified NG2 (>300 kDa) to the total integrated density of the modified plus unmodified NG2 bands. Experiments using control (n=9) and patient (n=8) OPCs are shown as aggregated data per individual subject (3 control and 3 patient siblings). Error bars in all panels reflect standard errors of the mean. Unpaired two-tailed Student's t-test revealed significantly less modified NG2 protein in whole cell lysate (t=2.88, P=0.04), intracellular (t=3.50, P=0.02) and surface fractions (t=3.31, P=0.03). **(D)** Control experiment showing that following chondroitinase ABC treatment, the abundance of 300 kDa (unmodified) NG2 in the whole cell lysate fraction is similar between patient and control OPCs (n=6 control and 6 patient clones, t=0.51, P=0.62). **(E)** In the absence of biotin (left panel), NG2 protein is undetectable in the Neutravidin-purified surface fraction. Furthermore, the absence of detectable actin in the surface protein samples confirms the high specificity of the biotin purification.



Supplementary Figure 4.5 Raw LI-COR western blot images. Full western blots for NG2 protein (upper) and re-blotting for actin (below). **(A)** Full blot corresponding to Figure 3D (lower half cut vertically for processing). **(B)** Full blot corresponding to **Supplementary Figure 4B**.



Supplementary Figure 4.6 CSPG4^{V901G} exhibits abnormal protein localization in U373 human glioma cells. Transfection of CSPG4^{V901G}-EGFP expression in human U373 glioma cells that lack endogenous CSPG4 demonstrates abnormal localization in vesicular structures that do not colocalize with lysosome marker LAMP1.



Supplementary Figure 4.7 *CSPG4P13* pseudogene sequencing controls. **(A)** Partial alignment of *CSPG4* Taqman amplicon (hg19 chromosome 15: 75982916-75983072) with homologous *CSPG4P13* pseudogene sequence (hg19 chromosome 15: 78188526-78188682). Filled arrow indicates the position of the *CSPG4* c.391G>A variant. Open arrow indicates the differential nucleotide distinguishing the flanking *CSPG4* sequence from *CSPG4P13*. **(B)** Sanger traces of an individual carrying the *CSPG4* c.391G>A variant while homozygous reference for *CSPG4P13*. **(C)** Sanger traces of a sample called falsely positive by Taqman genotyping due to a homologous *CSPG4P13* polymorphism (genomic position, hg19 chromosome 15: 78188583) while being homozygous reference for *CSPG4* c.391G.

Patient	II-1	III-5	III-7	III-9	III-11
Diagnosis (DSM)	SZ	SZ	SZ	SZ	SZ
Age of onset first psychosis	46	18	36	18	15
Medication	n/a	Clozapine Biperidene Lithium Oxazepam	Quetiapine Paroxetine Lorazepam	Zuclopenthixol	Zuclopenthixol Trihexyphenidyl Lithium Lorazepam

Supplementary Table 4.1 Discovery Family – Patient characteristics

Chromosome	Start position	End position	Start SNP	End SNP	MB	MAX LOD score
2	2686579	17262830	rs11694900	rs17476649	14.576251	0.8809
4	14744996	20524715	rs4464561	rs16869706	5.779719	0.8808
6	164665485	End	rs942731	rs9459964	5.675712	0.8809
7	Start	2739017	rs6583338	rs809547	2.692778	0.8852
7	69935641	97595184	rs4717530	rs9692345	27.659543	0.8852
7	148239179	End	rs6957883	rs1125769	10.809432	0.8852
10	1147045	9247586	rs4880763	rs1469993	8.100541	0.8808
11	Start	4905155	rs1045454	rs11603903	4.700927	0.8852
11	68289796	129160763	rs11228269	rs4644651	60.870967	0.8852
14	89036519	End	rs2116445	rs2583292	18.068524	0.8852
15	39135102	101779863	rs7167406	rs11858464	62.644761	0.8852
16	10480846	76592633	rs7195621	rs12599021	66.111787	0.8826
19	52447068	End	rs8105910	rs7910	6.646396	0.8851

Supplementary Table 4.2 Linkage analysis – Affected only model

Chromosome	Genomic position (hg19)	Ref	Alt	Gene symbol	Nr unaffected	MAF ExAC
11	108014748	A	G	ACAT1	1	0.00042
11	113679159	T	C	USP28	1	3.0x10 ⁻⁵
15	75983015	C	T	CSPG4	0	7.8x10 ⁻⁵
16	23080205	C	T	USP31	2	1.6x10 ⁻⁵
16	31371780	T	C	ITGAX	2	4.6x10 ⁻⁵

Supplementary Table 4.3 Discovery family candidate variants

PCR amplification primers		Internal Sanger primers	
Name	Sequence	Name	Sequence
CSPG4_ex01_F	CTGCCCCAGAGAGGAACAGC	CSPG4_ex3a_int_f1	ATGCAGCCACCCTCAATGG
CSPG4_ex01_R	CCCCTAACTGGACAGCCTTGG	CSPG4_ex3a_int_r1	TCCTCCTCCAGCCTGCAGC
CSPG4_ex02_F	GGGCTGGACACAAGGTGAGC	CSPG4_ex3a_int_f2	CGTCACCTCCAGGAACACCG
CSPG4_ex02_R	CAAGAGCCTGGCAGCAAGC	CSPG4_ex3a_int_r2	GGCAGCCAGAGAGTG GGG
CSPG4_ex03a_F	TGCCACAGCCTCCAAAGTAGC	CSPG4_ex3b_int_f1	CTGGCCCAAGGCTCTGCCAT
CSPG4_ex03a_R	GCAGAGTCCGGGTCATAGGC	CSPG4_ex3b_int_r1	GGTGCCCTGGCCTCCTTGAG
CSPG4_ex03b_F	GCTGGAGGTGTCCGGTGACG	CSPG4_ex3b_int_f2	ACAAGGCTGTGAGATGGCCAGG
CSPG4_ex03b_R	GGCAGCTGCACACATGTAACC	CSPG4_ex3b_int_f3	GGAGGTACGGGGTGTCTTCCG
CSPG4_ex04_F	ACCAGCTGCATGTCTGGCTGC	CSPG4_ex3b_int_f4	CCAACCTCGACATCCGCAGTG
CSPG4_ex04_R	CTGGCTCCGAGGAGTTGTGAGG	CSPG4_ex3b_int_r2	GCCGGCCACGCAACAGG
CSPG4_ex05_F	CAGTCTGGGGTTATACACAGAGAGG	CSPG4_ex3b_int_r3	TGGGTGTTCTGAGTGTGCAGTGG
CSPG4_ex05_R	GCTCTGAGCCGCGAAGTAGG	CSPG4_ex3b_int_r4	CGGCAGGAGAACTCGGTCG
CSPG4_ex06-07_F	AGCTGGGGCCTTCCTGGGTA	CSPG4_ex10a_int_f1	CCCAGCTGGCTGCAGGGC
CSPG4_ex06-07_R	GCCAGGTCCAGGCCTGTGTTT	CSPG4_ex10a_int_f2	CATCGAGGTGCAGCTGCGGG
CSPG4_ex08_F	GGTCACGCTGCCTCTTTGC	CSPG4_ex10a_int_r1	CTGCCACGCTGCTCCCGTTG
CSPG4_ex08_R	ACGTCTGCTGCCAGTGATGC	CSPG4_ex10a_int_r2	CCGGCTGGGGAAGTGTGTGAC
CSPG4_ex09_F	CCCAGAGTGGGGCCTGAG	CSPG4_ex10b_int_f1	GACCTTGAGGACGGGAGGCT
CSPG4_ex09_R	CCCAACCATCAAGCCAGGTC	CSPG4_ex10b_int_f2	CTGACTGCCAAGCCCCGCAA
CSPG4_ex10a_F	GGGAGGGACAATGGGAGAGG	CSPG4_ex10b_int_r1	GTAAGGCTCAGTGGCAAAGTCCA
CSPG4_ex10a_R	CCAGCTCGCCAGCATCTAGG	CSPG4_ex10b_int_r2	ATCTAGGACGGTGGGGTCCAGG
CSPG4_ex10b_F	CTCCGGGTGGTTTCAGATCG		
CSPG4_ex10b_R	TCTCCAGGCTCGGAGTGAGC		

Supplementary Table 4.4 Sanger sequencing primers for CSPG4 open reading frame

Name	Sequence
hOCT3/4-F	GACAGGGGGAGGGGAGGAGCTAGG
hOCT3/4-R	CTTCCCTCCAACCAGTTGCCCCAAAC
hSOX2-F	GGGAAATGGGAGGGGTGCAAAAGAGG
hSOX2-R	TTGCGTGAGTGTGGATGGGATTGGTG
hNANOG-F	CAGCCCCGATTCTTCCACCAGTCCC
hNANOG-R	CGGAAGATTCCCAGTCGGGTTCACC
hGDF3-F	CTTATGCTACGTAAAGGAGCTGGG
hGDF3-R	GTGCCAACCCAGGTCCCGGAAGTT
hREX1-F	CAGATCCTAAACAGCTCGCAGAAT
hREX1-R	GCGTACGCAAATTAAAGTCCAGA
hFGF4-F	CTACAACGCCTACGAGTCCTACA
hFGF4-R	GTTGCACCAGAAAAGTCAGAGTTG
hESG1-F	ATATCCCGCCGTGGGTGAAAGTTC
hESG1-R	ACTCAGCCATGGACTGGAGCATCC
hTERT-F	CCTGCTCAAGCTGACTCGACACCGTG
hTERT-R	GGAAAAGCTGGCCCTGGGGTGGAGC
hKLF4-F	TGATTGTAGTGCTTTCTGGCTGGGCTCC
hKLF4-R	ACGATCGTGGCCCCGAAAAGGACC
h-cMYC-F	GCGTCCTGGGAAGGGAGTTCCGGAGC
h-cMYC-R	TTGAGGGGCATCGTCGCGGGAGGCTG

Supplementary Table 4.5 qPCR primers for iPSC pluripotency genes

5

Replication kinetics, cell tropism and associated immune responses in SARS-CoV-2 and H5N1 virus infected human induced pluripotent stem cell-derived neural models

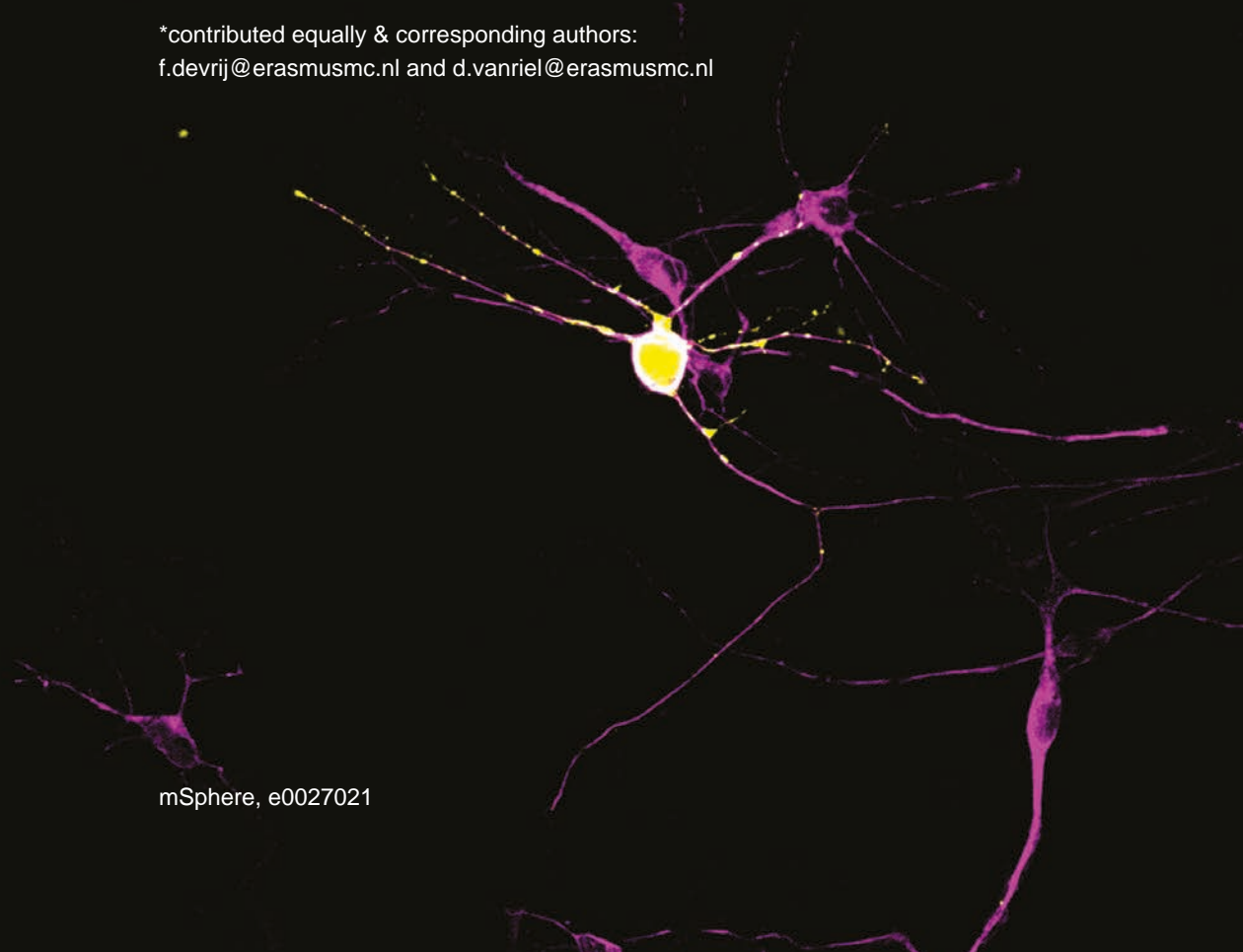
L Bauer^{1#}, B Lendemeijer^{2#}, L Leijten¹, CWE Embregts¹,
B Rockx¹, SA Kushner², FMS de Vrij^{2,*}, D van Riel^{1*}

Authors contributed equally

*contributed equally & corresponding authors:

f.devrij@erasmusmc.nl and d.vanriel@erasmusmc.nl

mSphere, e0027021

A fluorescence microscopy image showing several neurons. The cell bodies (soma) are stained bright yellow, while the extensive network of dendrites and axons is stained a vibrant magenta. The neurons are distributed across the field of view, with some showing more complex branching than others. The background is dark, making the stained cells stand out.

Abstract

Severe Acute Respiratory Syndrome Coronavirus-2 (SARS-CoV-2) infection is associated with a wide variety of neurological complications. Even though SARS-CoV-2 is rarely detected in the central nervous system (CNS) or cerebrospinal fluid, evidence is accumulating that SARS-CoV-2 might enter the CNS via the olfactory nerve. However, what happens after SARS-CoV-2 enters the CNS is poorly understood. Therefore, we investigated the replication kinetics, cell tropism, and associated immune responses of SARS-CoV-2 infection in different types of neural cultures derived from human induced pluripotent stem cells (hiPSCs). SARS-CoV-2 was compared to the neurotropic and highly pathogenic H5N1 influenza A virus. SARS-CoV-2 infected a minority of individual mature neurons, without subsequent virus replication and spread, despite ACE2, TMPRSS2 and NPR1 expression in all cultures. However, this sparse infection did result in the production of type-III-interferons and IL-8. In contrast, H5N1 virus replicated and spread very efficiently in all cell types in all cultures. Taken together, our findings support the hypothesis that neurological complications might result from local immune responses triggered by virus invasion, rather than abundant SARS-CoV-2 replication in the CNS.

Importance

Infections with the recently emerged Severe Acute Respiratory Syndrome Coronavirus-2 (SARS-CoV-2) are often associated with neurological complications. Evidence suggests that SARS-CoV-2 enters the brain via the olfactory nerve, however SARS-CoV-2 is only rarely detected in the central nervous system of COVID-19 patients. Here we show that SARS-CoV-2 is able to infect neurons of human iPSC neural cultures, but that this infection is abortive, and does not result in virus spread to other cells. However, infection of neural cultures did result in the production type III interferon and IL-8. This study suggests that SARS-CoV-2 might enter the CNS and infect individual neurons which triggers local immune responses that could contribute to the pathogenesis of SARS-CoV-2 associated CNS disease.

Introduction

Neurological manifestations are present in a substantial proportion of patients suffering from the respiratory coronavirus disease 2019 (COVID-19). Symptoms comprise loss of smell (anosmia), loss of taste (hypogeusia), headache, fatigue, nausea and vomiting^{111,262,263}. Additionally, more severe neurological complications such as seizures, confusion, cerebrovascular injury, stroke, encephalitis, encephalopathies and altered mental status are being increasingly reported in hospitalized patients^{264–266}.

It remains to be established whether the reported neurological manifestations are a direct consequence of local invasion of Severe Acute Respiratory Syndrome Coronavirus-2 (SARS-CoV-2) into the central nervous system (CNS), an indirect consequence of the associated systemic immune responses, or a combination of both. In human and animal models, it has been shown that SARS-CoV-2 is able to replicate in the olfactory mucosa^{267,268}, suggesting that the olfactory nerve could function as an important route of entry into the CNS²⁶⁹, as observed previously for other respiratory viruses¹¹². Post-mortem brain tissue analyses of fatal COVID-19 cases has revealed mild neuropathological changes which might be related to hypoxia, as well as pronounced neuroinflammation in different regions of the brain²⁷⁰. In the majority of cases, neither SARS-CoV-2 viral RNA, nor virus antigen, could be detected in the CNS^{265,271}. In line with this, SARS-CoV-2 viral RNA has rarely been detected in the cerebrospinal fluid (CSF) of COVID-19-patients with neurological symptoms^{110,272,273}. Together, this suggests that SARS-CoV-2 might enter the CNS but unable to replicate there efficiently.

In the brain, viruses encounter a variety of different cell types such as neurons, astrocytes and microglia. Investigations of CNS cell-type specific infection of SARS-CoV-2 have been inconsistent^{274–281}. Most studies have investigated virus replication by the detection of viral RNA, but have not reported whether infectious progeny viruses are produced during the course of infection. In order to investigate replication efficiency, cell tropism and associated immune responses of SARS-CoV-2 infection in cells of the CNS, we infected different types of human neural cultures. These cultures were differentiated from human induced pluripotent stem cells (hiPSCs) along a variety of different neural lineage specifications, which provided a unique and flexible platform to study the neurotropism of viruses *in vitro*. Specifically, we directed hiPSC-colonies towards neural progenitor cells (NPCs) via an embryoid body stage and subsequently differentiated NPCs to mature neural networks²⁸². In addition, we also utilized a rapid neuronal differentiation protocol based on forced overexpression of the transcription factor Ngn2 in hiPSCs (**Figure 5.1A**)^{40,148} to generate a pure population of neurons that we co-cultured with hiPSC-derived astrocytes. Using these specified CNS cell types, we directly compared the characteristics of SARS-CoV-2 infection with the highly pathogenic H5N1 influenza A virus, a virus with zoonotic potential which is known to efficiently replicate in neural cells *in vivo*^{283–288} and *in vitro*^{289–292}.

Results

SARS-CoV-2 does not replicate efficiently in hiPSC-derived neural cell types, despite the presence of ACE2, TMPRSS2 and NRP1

To investigate the replication efficiency of SARS-CoV-2, we utilized hiPSC-derived NPCs and differentiated these to mature forebrain cortical neural cultures using a previously published protocol²⁸² (**Figure 5.1A, Supplementary Figure 5.1**). The resulting cultures contain a mix of electrically active neurons, astrocytes and progenitors. Pure NPC and mixed mature neural network cultures were infected with SARS-CoV-2 and H5N1 virus at a multiplicity of infection (MOI) of 0.1 and 0.5. At 2, 6, 24 48 and 72 hours post infection (hpi), infectious virus titers in the supernatants were determined by endpoint titration. In contrast to H5N1 virus, no productive infection in SARS-CoV-2 inoculated NPC and mature neural network cultures was detected (**Figure 5.1B, C**). However, in one out of 3 experiments we observed an increase in virus titers at 72 hours post infection, which explains the small increase in virus titer in the mature neural network cultures. As an alternative to the laborious and time-consuming differentiation of mature neural networks through embryoid bodies and NPC stages, we also employed an established rapid differentiation protocol that yields a pure culture of iPSC-derived glutamatergic cortical neurons by overexpressing the transcription factor neurogenin-2 (Ngn2)⁴⁰. We further supplemented the Ngn2-induced neurons with hiPSC-derived astrocytes to support their survival and maturation. The final Ngn2 co-cultures contain astrocytes and functional forebrain cortical neurons that form synapses (**Figure 5.1A, Supplementary Figure 5.1**). SARS-CoV-2 did not replicate efficiently in the Ngn2 co-cultures, in contrast to H5N1 virus (**Figure 5.1D**). As a positive control for virus replication, Vero-E6 and MDCK cells were infected with SARS-CoV-2 and H5N1 virus, respectively (**Figure 5.1E and 5.1F**).

Next, we evaluated the presence of important SARS-CoV-2 entry factors, such as angiotensin-converting enzyme 2 (ACE2), transmembrane protease serine 2 (TMPRSS2) and neuropilin-1 (NRP1). In all cultures, there was clear evidence for ACE2, TMPRSS2 and NRP1 expression, suggesting cellular susceptibility to SARS-CoV-2 infection (**Figure 5.1G, Supplementary Figure 5.2**).

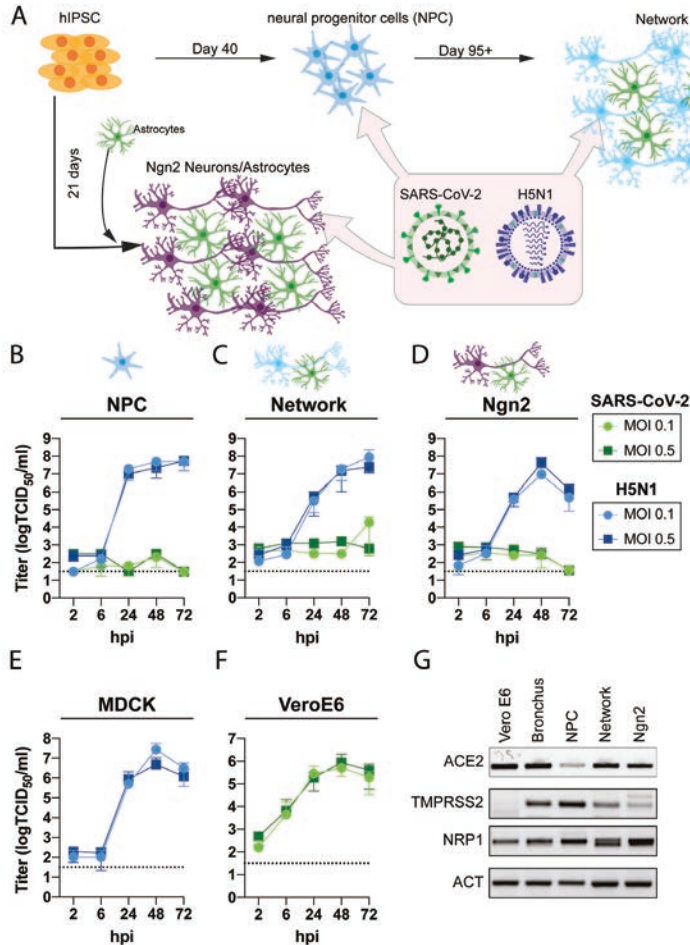


Figure 5.1 SARS-CoV-2 does not replicate in hiPSC derived neural (co-)cultures in contrast to H5N1 virus. **(A)** A schematic depiction of the different hiPSC-derived differentiation strategies of the neural cultures. hiPSC are differentiated into neural progenitor cells (NPC) and subsequently into mixed neural cultures containing mixed neurons and astrocytes. Alternatively, hiPSC are differentiated into excitatory neurons by inducing overexpression of Ngn2, these are grown in a co-culture with hiPSC-derived astrocytes. Growth kinetics of SARS-CoV-2 or H5N1 virus, in hiPSC-derived **(B)** NPCs, **(C)** mature neural networks, or **(D)** Ngn2 co-cultures using a MOI of 0.1 and 0.5. As positive controls **(E)** MDCK and **(F)** VeroE6 cells were infected with H5N1 virus or SARS-CoV2, respectively. Data represent mean \pm standard deviation (SD) from three independent experiments. Every growth curve was performed either in biological duplicates or triplicates. **(G)** Presence of the host factors angiotensin-converting enzyme 2 (ACE2), Transmembrane protease serine 2 (TMPRSS2) and neuropilin-1 (NRP1) of the neural cultures was determined with PCR. As controls for the expression of ACE2 and TMPRSS2 bronchus bronchiole organoids were used. The uncropped agarose gels are displayed in **Supplementary Figure 5.2**.

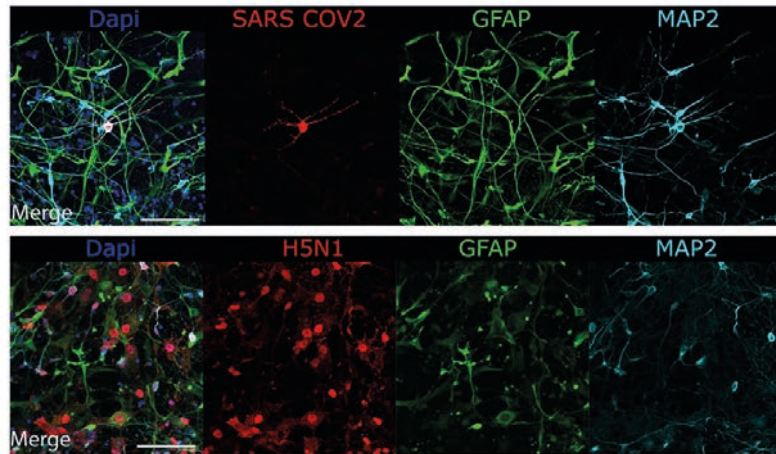
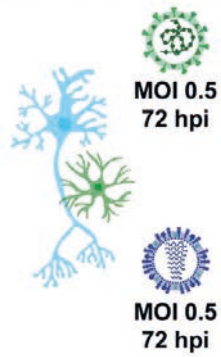
SARS-CoV-2 infects MAP2-expressing neurons and does not induce cleavage of caspase-3

To determine whether SARS-CoV-2 was able to infect individual cells, we stained for virus nucleocapsid protein (NP) 24 and 72 hpi with a MOI of 0.5. SARS-CoV-2 sparsely infected cells in neural cultures at 24 and 72 hpi. Infection was observed in single scattered MAP2⁺ neurons (**Figure 5.2A, B** and **Supplementary Figure 5.3A, C**). In one experiment, we identified a cluster of MAP2⁺ cells that stained positively for SARS-CoV-2 NP at 72 hpi (**Supplementary Figure 5.4A**). In the Ngn2 co-cultures, we were only able to detect MAP2⁺/NEUN⁺ neurons positive for SARS-CoV-2 NP, suggesting that SARS-CoV-2 infects only mature neurons and does so only sparsely (**Supplementary Figure 5.4B**). We found no convincing evidence of SARS-CoV-2 NP⁺ cells among SOX2⁺ NPCs or GFAP⁺ astrocytes (**Figure 5.2A-2C**). In contrast, H5N1 virus abundantly infected SOX2⁺ NPCs, GFAP⁺ astrocytes and MAP2⁺ neurons (**Figure 5.2A-C**).

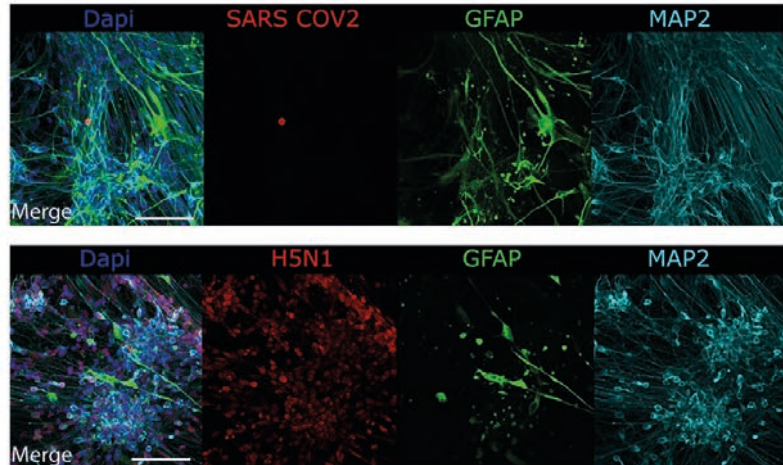
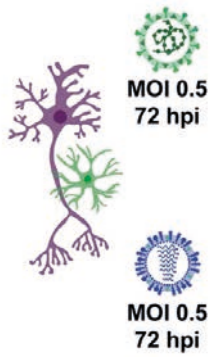
Next, despite the fact that there was no morphological evidence for cell death in the SARS-CoV-2 infected cultures, we wanted to investigate whether SARS-CoV-2 infection induced apoptosis in SARS-CoV-2 NP⁺ neurons. Therefore, we infected Ngn2 co-cultures with SARS-CoV-2 and stained for cleaved caspase-3, an apoptosis marker. We again observed that SARS-CoV-2 infected only MAP2⁺ neurons. Neurons expressing SARS-CoV-2 NP did not show accumulation of cleaved caspase-3 (**Figure 5.3A, B** and **Supplementary Figure 5.4C**).

→ **Figure 5.2** SARS-CoV-2 infects MAP2⁺ neurons. (**A**) Mixed neural culture (scale bar = 100 μm), (**B**) Ngn2 co-cultures (scale bar = 100 μm) and (**C**) NPCs (scale bar = 50 μm) were infected with a MOI of 0.5 with SARS-CoV-2 or H5N1 virus, respectively. 72 hours post infection, the cells were fixed, stained for the presence of viral antigen (SARS-CoV-2 NP or H5N1 NP in red). MAP2 (cyan) was used as a marker for neurons, astrocytes were identified by staining for glial fibrillary acidic protein (GFAP) (green) and SOX2 (green) was used as a marker for NPCs. Cells were counterstained with DAPI (blue) to visualize the nuclei. Data shown are representative examples from three independent experiments for each culture condition.

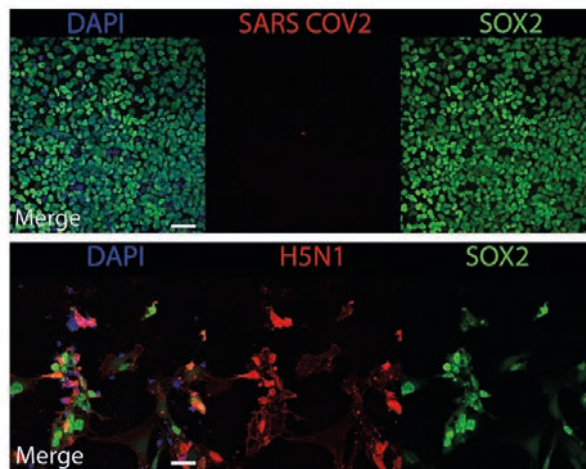
A Network



B Ngn2



C NPCs



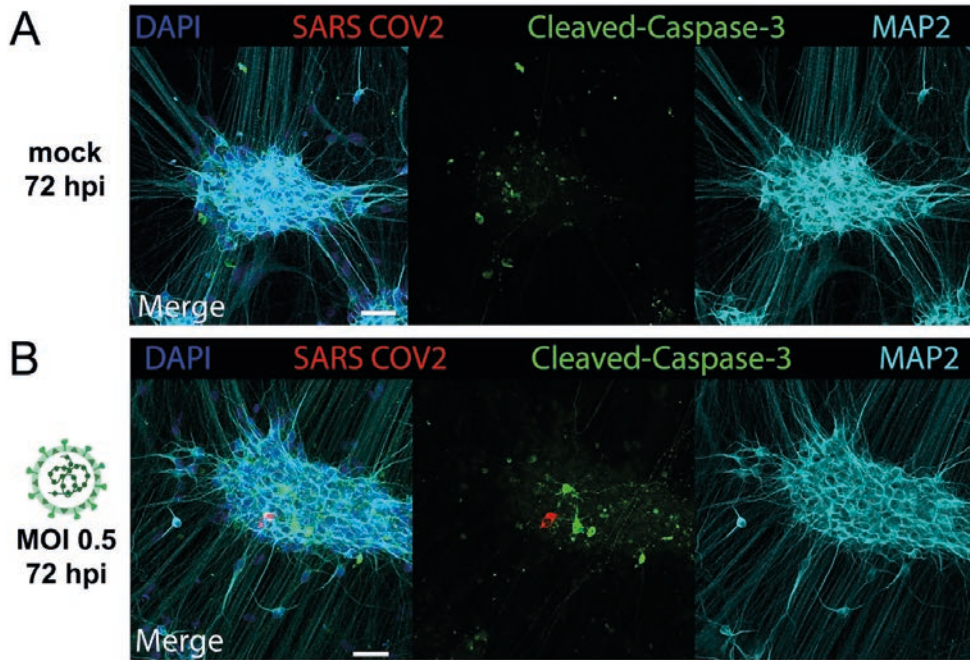


Figure 5.3 SARS-CoV-2 infections does not result in upregulation of cleaved caspase-3. Ngn2 co-cultures were either (A) mock infected or infected with (B) SARS-CoV-2 at a MOI 0.5 (scale bar = 50 μ m). 72 hours post infection, the cells were fixed and stained for the presence of SARS-CoV-2 antigen (red) and for the apoptosis marker cleaved caspase-3 (green). Data shown are representative examples from two independent experiments.

SARS-CoV-2 infection induces IFN λ 2/3 and IL-8

To determine the immune response of the neural cultures towards SARS-CoV-2 and H5N1 virus infection, we measured a panel of antiviral cytokines in the supernatant of infected neural cultures at 24 and 72 hours post infection (**Figure 5.4**). Even though SARS-CoV-2 infection was scarce, IFN λ 2/3 was induced in both the mixed neural culture and Ngn2 co-cultures, but not in NPC cultures. Increased secretion of IL-8 was observed in NPC cultures, mixed neural culture and Ngn2 co-cultures. H5N1 virus infection induced both type-III-IFN -IFN λ 1 and -IFN λ 2/3 in mixed neural cultures and Ngn2 co-cultures, but not among NPCs. Furthermore, increased levels of IP-10 were detected only in the H5N1 virus infected neural cultures. Similar to SARS-CoV2, H5N1 virus was also able to induce IL-8 in all neural cultures. Neither SARS-CoV-2, nor H5N1, virus infection induced type-I-interferon (IFN α /IFN β) or type-II-IFN (IFN γ) or other cytokines such as IL-1b, TNF-a, IL-12p70, GM-CSF or IL-10 (**Supplementary Figure 5.5**).

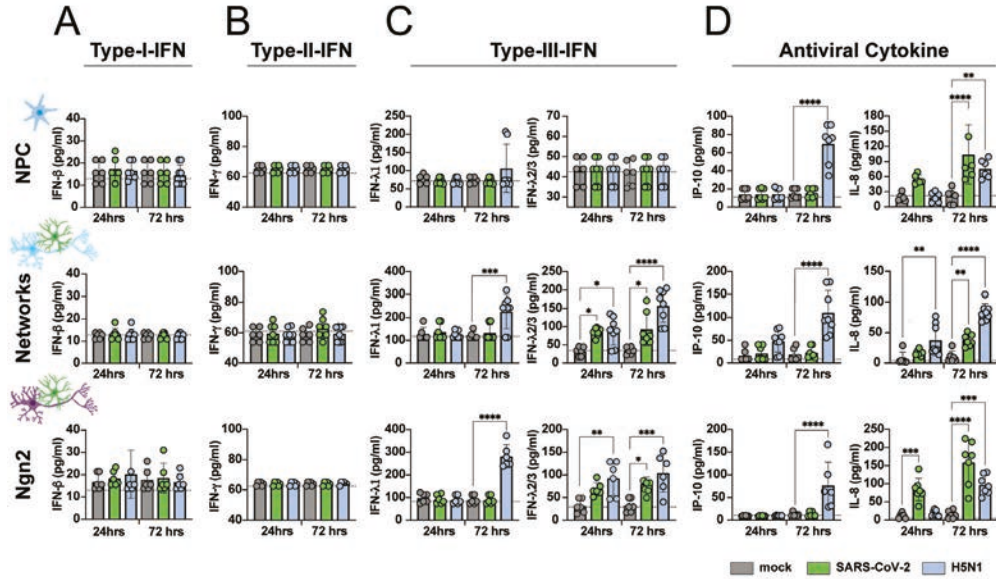


Figure 5.4 SARS-CoV-2 infection induces type-III-IFN and IL-8. NPCs, mixed neural cultures and Ngn2 co-cultures were infected with SARS-CoV-2 and H5N1 virus at a MOI 0.1. Concentration of (A) type-I-interferon (IFN-β), (B) type-II-IFN (IFN-γ), (C) type-III-IFN (IFN-λ1 and IFN-λ2/3) and (D) the antiviral cytokines IP-10 and IL-8 were measured in the supernatant 24 and 72 hours post infection. The data are derived from three independent experiments and each experiment was performed either in biological duplicates or triplicates. The assay was performed in technical duplicates for each sample. The data displayed represent average values of the technical duplicates of each experiment performed. Error bars denote mean ± standard deviation (SD). Statistical significance was calculated with a one-way ANOVA with a Bonferroni post hoc test, the means of the mock infected samples were compared to the means of the SARS-CoV-2 and H5N1 virus infected samples at 24 and 72 hours post infection. Asterisks (*) indicate statistical significance. *P<0.05, **P<0.01, ***P<0.001, ****P<0.0001.

Discussion

SARS-CoV-2 replicated poorly in all three types of hiPSC-derived neural cultures used in our experiments, which contrasts largely to H5N1 virus, which replicated efficiently to high titers. Even though important entry factors for SARS-CoV-2 are expressed in all of the cultures used, SARS-CoV-2 infected a very small proportion of cells without evidence of subsequent spread. Additionally, we did not observe SARS-CoV-2 induced neuronal cell death, indicated by a lack of co-labeling with apoptosis-marker cleaved caspase 3 in SARS-CoV-2 NP⁺ neurons. However, SARS-CoV-2 infection did induce type-III-IFN and IL-8 production.

Evidence is accumulating that SARS-CoV-2 enters the CNS via the olfactory nerve^{267–269}, a pathway that is also used by influenza A viruses to enter the CNS in many mammals including humans^{112,293}. H5N1 virus spreads efficiently to the CNS via the olfactory nerve in experimentally inoculated ferrets and subsequently replicates very efficiently in the CNS^{283,285,294}. Unlike H5N1 virus infection, SARS-CoV-2 is rarely detected in the CNS of fatal COVID-19 patients or experimentally inoculated animals^{110,270–273}. In addition, only a handful of case reports of SARS-CoV-2 induced encephalitis have been reported^{295,296}. *In vitro* studies have mainly focused on the ability of SARS-CoV-2 to infect cells of the CNS based on the detection of viral RNA or viral antigen^{276,277,280,297,298} but not many have investigated replication efficiency in time by measuring infectious virus titers²⁷⁵. So far, several studies showed limited infection of neurons in hiPSC derived brain organoids²⁸⁰ and brainspheres²⁷⁷, without efficient SARS-CoV-2 replication. So far, only efficient replication has been shown in choroid plexus organoids especially within choroid plexus epithelium cells^{275,298}. Altogether, these observations are consistent with our findings of poor SARS-CoV-2 replication in hiPSC-derived NPCs, neurons and astrocytes, and supports a pathophysiological model whereby SARS-CoV-2 invades the CNS, but does not replicate efficiently in CNS cell types. However, one caveat of our study is that other cells such as microglia, oligodendrocytes and vascular cells (pericytes, endothelial cells) are not present. Therefore, we cannot exclude that SARS-CoV-2 can infect and possibly replicate efficiently in other cells of the CNS or neuronal cell types such as cortical PV interneurons, midbrain or hindbrain cell types.

Despite the low proportion of SARS-CoV-2 infected cells and the fact that infection seemed to be abortive in the hiPSC-derived neural cultures, we found evidence for cellular immune activation. In particular, SARS-CoV-2 infection of the neural cultures resulted in the induction of type-III-IFN especially IFN λ 2/3, but not type-I-IFN or type-II-IFN. This result is in accordance with earlier reports suggesting that SARS-CoV-2 triggers only very mild type-I and type-II-IFN responses, but does trigger a robust type-III-IFN response in cell culture, human airway epithelial cells, ferrets and SARS-CoV-2 infected individuals^{299,300}. In addition, IL-8—a chemotactic factor that attracts leukocytes—was induced in all hiPSC-derived cultures. In lung tissue and peripheral venous blood serum of SARS-CoV-2 infected

patients, elevated levels of IL-8 are associated with severe COVID-19^{301–303}. Furthermore, IL-8 has been detected in the CSF of SARS-CoV-2 patients who developed encephalitis, which might be induced by the SARS-CoV-2 associated brain immune response, since SARS-CoV-2 RNA could not be detected in the CSF³⁰⁴. However, how exactly these cytokines contribute to the *in vivo* neuroinflammatory process, and if they are directly triggered by SARS-CoV-2 entry into the CNS needs further investigations.

Highly pathogenic H5N1 virus replication has been reported *in vivo*^{283,285,287,288,305} and *in vitro* across several different types of human and mouse neural cell cultures^{290–292}, including the human neuroblastoma line SK-N-SH²⁶, suggesting this virus is neurotropic. This fits with our observation that H5N1 virus replicates productively and spreads throughout hiPSC-derived neural cultures, infecting NPCs as well as mature neurons and astrocytes. H5N1 virus infection also results in the upregulation the type-III-IFN IFN λ 1 and IFN λ 2/3, as well as the antiviral cytokines IL-8 and IP-10. IP-10 has been detected in the CSF of influenza A virus infected patients and was found to be elevated in the brains of mice experimentally infected with H5N1 virus³⁰⁶. However, the mechanism by which H5N1 virus achieves abundant virus replication and robust induction of pro-neuroinflammatory cytokines remains poorly understood.

Overall, our data fit with clinical findings concerning the ability of these viruses to cause acute CNS disease. In both humans and mammalian animal models, H5N1 virus is able to invade and replicate in cells of the CNS, including neurons, resulting in an acute (meningo)-encephalitis^{307–309}. In contrast, even though evidence exists that SARS-CoV-2 is able to spread to the CNS via the olfactory nerve^{267–269} in SARS-CoV-2 infected patients or experimentally infected animal models, virus is rarely detected in the CNS or associated with acute encephalopathies^{110,272,273}.

Altogether, our findings reveal that replication of SARS-CoV-2 in CNS cell types is very limited, which is in contrast to the efficient replication and spread of H5N1 virus. Although the mechanistic pathogenesis of SARS-CoV-2 associated CNS disease remains poorly understood, this study supports the hypothesis that SARS-CoV-2 entry into the CNS and direct infection of a small subset of neurons might trigger inflammation in the brain.

Material and Methods

Cell Lines

VeroE6 (ATCC® CRL 1586TM) cells were maintained in Dulbecco's modified Eagle's medium (DMEM, Lonza, Breda, the Netherlands) supplemented with 10% fetal calf serum (FCS, Sigma-Aldrich, St. Louis, MO, USA), 10mM HEPES, 1.5 mg/ml sodium bicarbonate, 100 IU/ml penicillin (Lonza, Basel, Switzerland) and 100 µg/ml streptomycin (Lonza). Madin-Darby Canine Kidney (MDCK) cells were maintained in Eagle minimal essential medium (EMEM; Lonza) supplemented with 10% FCS, 100 IU/ml penicillin, 100 µg/ml streptomycin, 2 mM glutamine, 1.5 mg/ml sodium bicarbonate, 1 mM, 10 mM HEPES and 0.1 mM nonessential amino acids. All cell lines were grown at 37 °C in 5% CO₂. The medium was refreshed every 3–4 days, and cells were passaged at >90% confluence with the use of PBS and trypsin-EDTA (0.05%). The cells were routinely checked for the presence of mycoplasma.

Differentiation of iPSCs to NPCs and mature neural cultures

Human induced pluripotent stem cells (iPSCs) [WTC-11 Coriell #GM25256, obtained from the Gladstone Institute, San Francisco, USA] were differentiated to NPCs as previously described² with slight modifications. After passage 3, NPC cultures were purified using fluorescence-activated cell sorting (FACS) as described previously¹⁴⁶. Briefly, NPCs were detached from the culture plate and resuspended into a single cell solution. CD184+/CD44-/CD271-/CD24+ cells were collected using a FACSaria III (BD bioscience) and expanded in NPC medium (**Table 5.1**). NPCs were used for experiments between passage 3 and 7 after sorting or differentiated to neural networks. For differentiation towards mature neural cultures, NPCs were grown in neural differentiation medium (**Table 5.1**) for 6-8 weeks to achieve mature neural networks²⁸² and subsequently used for experiments, after week 4 only half of the medium was refreshed. Cultures were kept at 37 °C/5%CO₂ throughout the entire differentiation process.

Differentiation of iPSCs to Ngn2 co-cultures

iPSCs were directly differentiated into excitatory cortical layer 2/3 neurons by forcibly overexpressing the neuronal determinant Neurogenin 2 (Ngn2)^{40,148}. To support neuronal maturation, hiPSC-derived astrocytes were added to the culture in a 1:1 ratio. At day 3, the medium was changed to Ngn2-medium (**Table 5.1**). Cytosine b-D-arabinofuranoside (Ara-C) (2 µM; Sigma, C1768) was added once to remove proliferating cells from the culture and ensure long-term recordings of the cultures. From day 6 onwards, half of the medium was refreshed three times per week. Cultures were kept at 37 °C/5%CO₂ throughout the entire differentiation process.

Viruses

The SARS-CoV-2 isolate (isolate BetaCoV/Munich/BavPat1/2020; European Virus Archive Global #026V-03883; kindly provided by Dr. C. Drosten) was previously described by Lamers *et al.*^{310,311} The zoonotic HPAI H5N1 virus (A/Indonesia/5/2005) was isolated from a human patient and the virus was propagated once in embryonated chicken eggs and twice in MDCK cells.

Virus Titrations

The SARS-CoV-2 titers were determined by endpoint dilution on VeroE6 cells, calculated according to the method of Spearman & Kärber and expressed as 50% tissue culture infectious dose/ml (TCID₅₀/ml). SARS-CoV-2 virus titers were determined by preparing 10-fold serial dilutions in triplicates of supernatants in Opti-MEM containing GlutaMAX. Dilutions supernatants were added to a monolayer of 40.000 VeroE6 cells/well in a 96-well plate and incubate at 37°C. After 5 days the plates were examined for the presence of cytopathic effect (CPE). Virus titers of HPAI H5N1 were determined by endpoint dilution on MDCK as described previously³¹². In short, 10-fold serial dilutions of cell supernatant in triplicates were prepared in Influenza infection medium which consists of EMEM supplemented with 100 IU/ml penicillin, 100 µg/ml streptomycin, 2 mM glutamine, 1.5 mg/ml sodium bicarbonate, 10 mM HEPES, 1× (0.1 mM) nonessential amino acids, and 1 µg/µl TPCK-treated trypsin (Sigma-Aldrich). Prior to adding the virus dilutions to the MDCK cells, the cells were washed once with plain EMEM-medium to remove residual FCS. 100 µl of the diluted supernatants was used to inoculate 30.000 MDCK cells/well in a 96-well plate. After one hour, the inoculum was removed and 200 µl fresh influenza infection medium was added. Four days after infection, supernatants of the infected MDCK cells were tested for agglutination. 25 µl of the supernatant were mixed with 75 µl 0.33% turkey red blood cells and incubated for one hour at 4°C. The titers of infectious virus were calculated according to the method of Spearman & Kärber and expressed as TCID₅₀/ml. All experiment with infectious SARS-CoV-2 and H5N1 virus were performed in a Class II Biosafety Cabinet under BSL-3 conditions at the Erasmus Medical Center. The initial 1:10 dilution of cell supernatant resulted in a detection limit of 10^{1.5} TCID₅₀/ml.

Replication Kinetic

Before infection of neural progenitors, network neurons and NGN2 neurons, supernatant was removed and cells were infected with SARS-CoV-2 and H5N1 virus at the indicated multiplicity of infection (MOI). As control for active virus replication, VeroE6 and MDCK cells were infected with SARS-CoV-2 and H5N1 virus, respectively. Before virus infection, the VeroE6 cells were washed with SARS-CoV-2 infection medium (DMEM supplemented with 2% FBS and 100 IU/ml penicillin, 100 µg/ml streptomycin) and MDCK cells were washed with influenza infection medium. After 1 hours of incubation at 37°C, the inoculum was

removed and replaced with fresh medium and old medium in a 1:1 ratio. After removing the inoculum from VeroE6 and MDCK cells, SARS-CoV-2 infection medium and influenza infection medium, respectively, were added to the cells. At the indicated timepoints an aliquot of the supernatant was collected for subsequent virus titration. All experiments were performed in biological triplicates and either in technical duplicates or triplicates.

PCR Validation of ACE2, TMPRSS2 and NRP1 expression

RNA was isolated from the neural cultures and VeroE6 cells using the High Pure RNA Isolation Kit (Roche). The concentration of RNA was determined using Nanodrop. 2.5µg of RNA was reverse transcribed into cDNA using the SuperScript III reverse transcriptase (Invitrogen) according to the manufacturers' protocol. cDNA of bronchus-bronchiol organoids were kindly provided by Anna Z. Myktyyn. Presence of ACE2, TMPRSS2, NRP1 and ACT was evaluated by amplified these genes with gene specific primers (**Table 5.2**) by PCR. Gene products were visualized on a 2% agarose gel which was stained with SYBR Safe. PCR products of the genes were sequenced to validate that the right product was amplified.

Multiplexed bead-assay for Cytokine Profiling

Cytokines were measured using the LEGENDplex™ Human Anti-Virus Response Panel (BioLegend). The kit was used according to manufacturer's manual with an additional fixing step. After adding the SA-PE and performing the washing steps, the supernatant and the beads were fixed with formalin for 15 minutes at room temperature and washed twice with the provided wash buffer. This ensures that all pathogens are not infectious.

Immunofluorescent labeling

Cells were fixed using 4% formalin in PBS and labeled using immunocytochemistry. Primary antibody incubation was performed overnight at 4°C. Secondary antibody incubation was performed for 2 hours at room temperature. Both primary and secondary antibody incubation was performed in staining buffer [0.05 M Tris, 0.9% NaCl, 0.25% gelatin, and 0.5% Triton X-100 (Sigma, T8787) in PBS (pH 7.4)]. Primary antibodies and their dilutions can be found in **Table 5.3**. Secondary antibodies conjugated to Alexa-488, Alexa-647 or Cy3 were used at a dilution of 1:400 (Jackson ImmunoResearch). Nuclei were visualised using DAPI (ThermoFisher Scientific, D1306). Samples were embedded in Mowiol 4-88 (Sigma-Aldrich, 81381) and imaged using a Zeiss LSM 800 confocal microscope (Oberkochen, Germany).

Acknowledgments

We thank Anna Z. Mykytyn and Mart M. Lamers for sharing reagents, cDNA of the airway organoids, SARS-CoV-2 virus stocks and for technical advice and scientific discussions. This work was funded by a fellowship to D.V.R. from the Netherlands Organization for Scientific Research (VIDI contract 91718308) and a EUR fellowship. This work was also supported by the Netherlands Organ-on-Chip Initiative, an NWO Gravitation project (024.003.001) funded by the Ministry of Education, Culture and Science of the government of the Netherlands (S.K, F.D.V., B.L.) and by an Erasmus MC Human Disease Model Award to F.D.V.

The authors declare no conflict of interest.

Name	Reagents	Manufacturer, catalogue number
NPC Medium	Advanced DMEM/F12 1% N-2 Supplement 2% B-27 minus RA Supplement 1 µg/ml Laminin 1% Penicillin-Streptomycin 20 ng/ml basic Fibroblast Growth Factor	ThermoFisher Scientific, 1634010 ThermoFisher Scientific, 17502048 ThermoFisher Scientific, 12587010 Sigma-Aldrich, L2020 ThermoFisher Scientific, 15140122 Merck, GF003AF
Neural Differentiation Medium	Neurobasal medium 1% N-2 Supplement 2% B-27 minus RA Supplement 1% MEM NEAA 2 µg/ml Laminin 1% Penicillin-Streptomycin 20 ng/ml BDNF 20 ng/ml GDNF 1 µM db-cAMP 200 µM ascorbic acid	ThermoFisher Scientific, 21103049 ThermoFisher Scientific, 17502048 ThermoFisher Scientific, 12587010 ThermoFisher Scientific, 11140035 Sigma-Aldrich, L2020 ThermoFisher Scientific, 15140122 ProSpec, CYT-207 ProSpec, CYT-305 Sigma-Aldrich, D0627 Sigma-Aldrich, A5960
Ngn2 medium	Neurobasal medium 2% B-27 minus RA Supplement 2 µg/ml Laminin 1% Glutamax 10 ng/ml NT3 20 ng/ml BDNF 1% Penicillin-Streptomycin	ThermoFisher Scientific, 21103049 ThermoFisher Scientific, 12587010 Sigma-Aldrich, L2020 ThermoFisher Scientific, 35050061 PeproTech, 450-03 ProSpec, CYT-207 ThermoFisher Scientific, 15140122

Table 5.1 Overview of media used during differentiation.

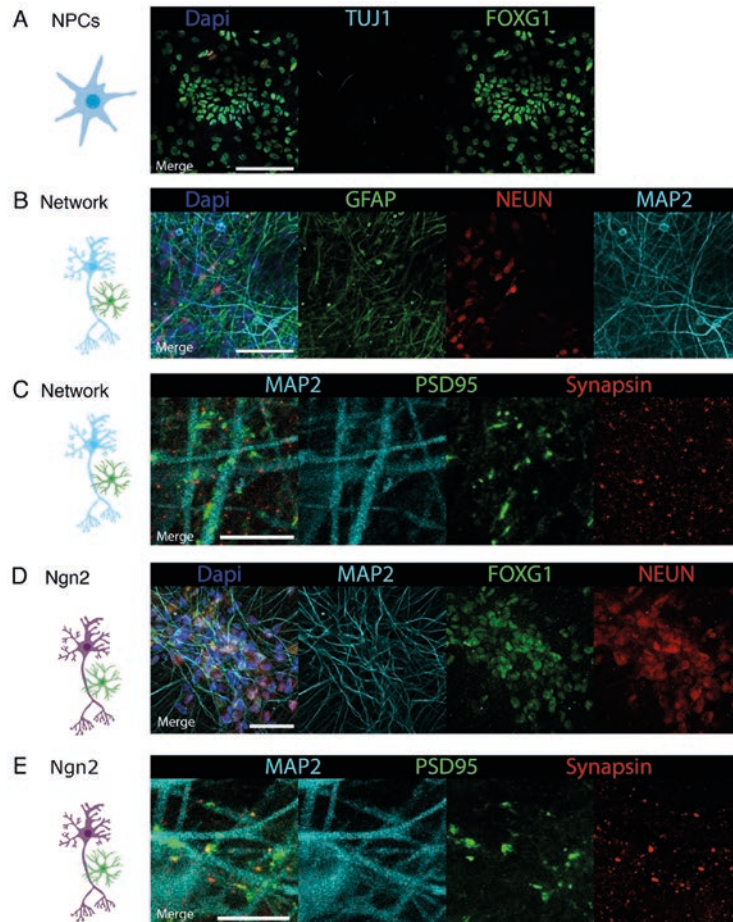
Genes	Sequence (5' > 3')	Annealing Temp (°C)	Amplicon (bp)	Ref
ACE2-FWD	GGGATCAGAGATCGGAAGAAGAAA	60	124	1
ACE2-REV	AGGAGGTCTGAACATCATCAGTG			1
b-ACTIN-FWD	CCCTGGACTTCGAGCAAGAG	60	153	1
b-ACTIN-REV	ACTCCATGCCCAGGAAGGAA			1
TMPRSS2-FWD	AATCGGTGTGTTCCGCTCTAC	60	106	1
TMPRSS2-REV	CGTAGTTCTCGTTCCAGTCGT			1
NRP1-FWD	GACTGGGGCTCAGAATGGAG	60	187	
NRP1-REV	ATGACCGTGGGCTTTTCTGT			

Table 5.2 Overview of primers used

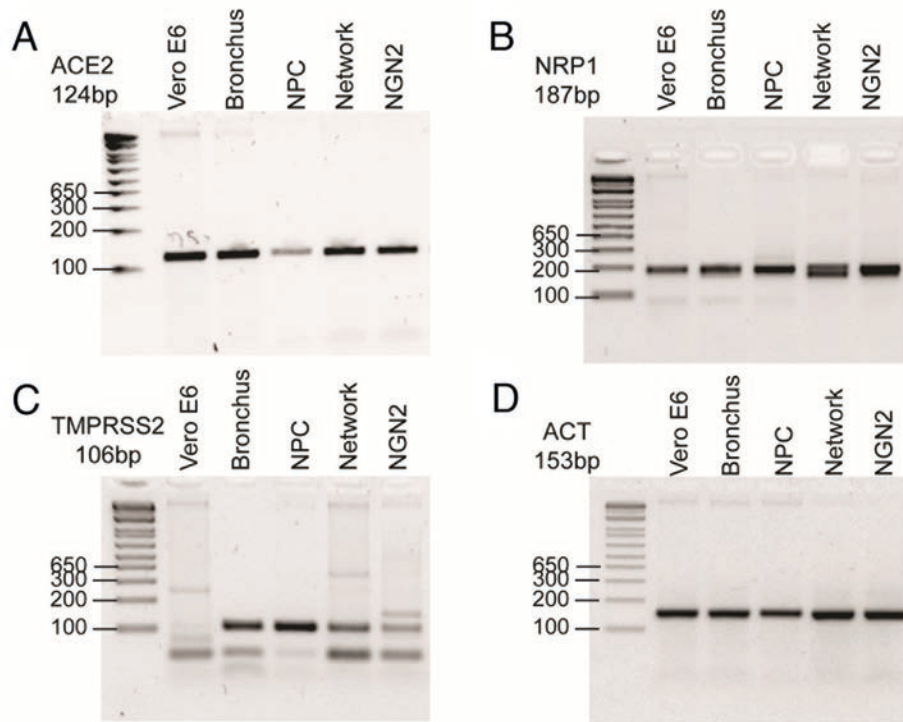
Antibody	Dilution	Manufacturer, catalogue number
SARS-CoV-2- Anti NP	1:500	Sino Biological, 40143-MM05
SOX2	1:250	Millipore, AB5603
NEUN	1:100	Merck, ABN78
GFAP	1:200	Millipore, AB5804
MAP2	1:200	Synaptic Systems, 188004
H5N1- Anti NP	1:1000	EVL, EBS-I-047, Clone Hb65
Cleaved Caspase-3	1:100	Cell Signaling Technologies, 9661S
Beta III Tubulin (TUJ1)	1:200	Millipore, AB9354
PSD-95	1:100	Thermo Scientific, MA1-046
Synapsin	1:100	Synaptic Systems, 106 103
FOXG1	1:200	Abcam, 18259

Table 5.3 Antibodies used for immunocytochemistry.

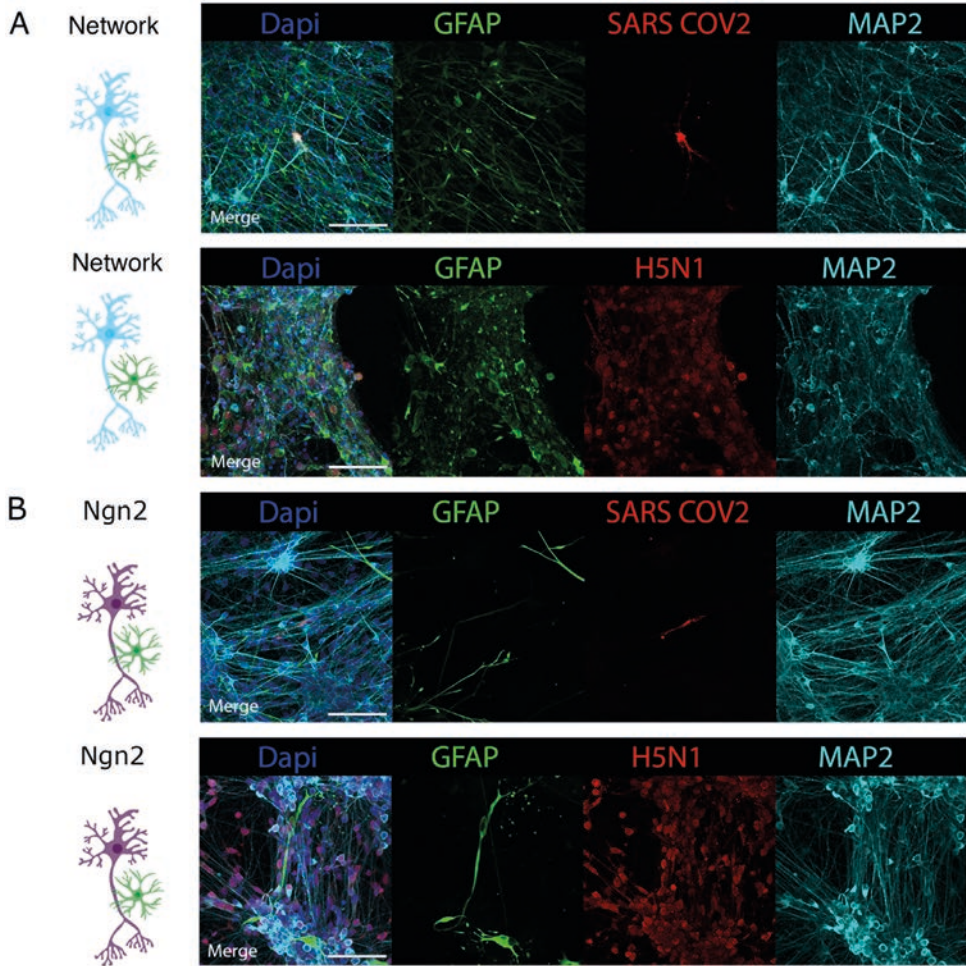
Supplementary Figures



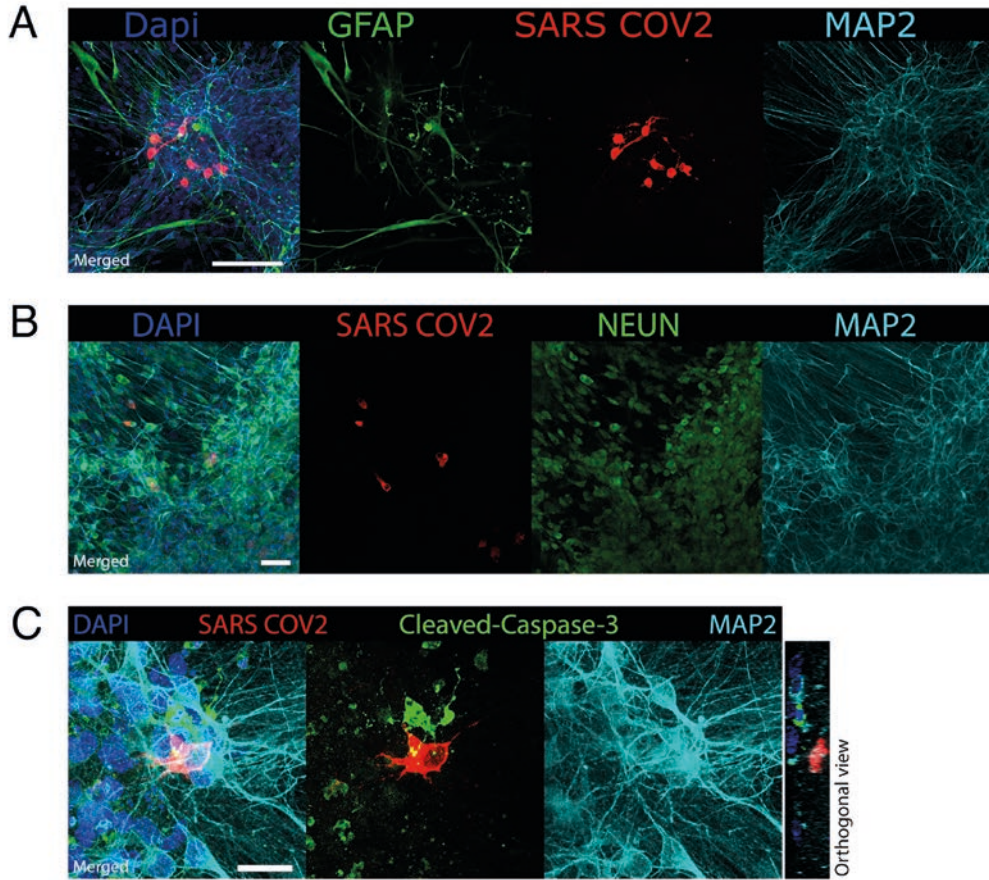
Supplementary Figure 5.1 Immunohistological characterization of neural cultures. **(A)** NPC cultures that were used to generate mixed neural cultures are positive for FOXG1 (green), indicating a forebrain identity. TUJ1, a marker for immature neurons, is hardly detected in cells, suggesting a pure population of precursor cells (scale bar = 100 μ m). **(B)** Eight-week old mixed neural cultures contain astrocytes (GFAP, green) and neurons that stain positive for MAP2 (cyan) and the mature neuronal marker NEUN (red) (scale bar = 100 μ m). **(C)** Neurons express pre- (synapsin, red) and post-synaptic (PSD95, green) proteins that co-localize with MAP2 (cyan), suggesting the formation of synapses (scale bar = 10 μ m). **(D)** Neurons (MAP2, cyan) in three-week old Ngn2 co-cultures express FOXG1 (green) and NEUN (red), indicating that the cells have developed towards mature cortical forebrain neurons (scale bar = 50 μ m). **(E)** Ngn2-neurons express pre- (synapsin, red) and post-synaptic (PSD95, green) proteins that co-localize with MAP2 (cyan), suggesting the formation of synapses (scale bar = 10 μ m).



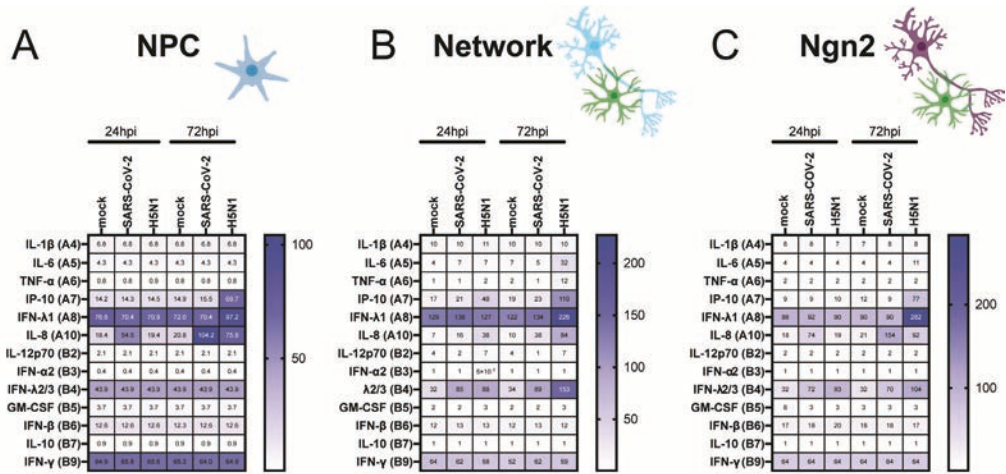
Supplementary Figure 5.2 Expression of important entry factors for SARS-CoV-2, original pictures from the gels. Expression of **(A)** ACE2 with amplicon size 124bp **(B)** NRP1 with amplicon size 187 bp **(C)** TMPRSS2 with amplicon size 106bp **(D)** ACT with amplicon size 153bp from one out of two independent experiment are shown. The important bands with the correct sizes of the amplicon were cropped and are represented in **Figure 1G**.



Supplementary Figure 5.3 SARS-CoV-2 infects MAP2+ neurons. **(A)** Mixed neural culture (scale bar = 100 μ m) and **(B)** Ngn2 co-cultures (scale bar = 100 μ m) were infected with a MOI of 0.5 with SARS-CoV-2 or H5N1 virus, respectively. 24 hours post infection, cells were fixed and stained for the presence of viral antigen (SARS-CoV-2 NP or H5N1 NP in red). MAP2 (cyan) was used as a marker for neurons, astrocytes were identified by staining for glial fibrillary acidic protein (GFAP) (green). DAPI (blue) was used to visualize the nuclei. Data shown are representative examples from two independent experiments.



Supplementary Figure 5.4 SARS-CoV2 infects NEUN+ neurons and does not induce cleaved-caspase-3 expression. **(A)** One focus of multiple infected cells was identified (scale bar = 100 μ m). **(B)** The neurons in the Ngn2 cultures consist of a homogeneous population of mature NEUN+ neurons (scale bar = 50 μ m). **(C)** High magnification image of a SARS-CoV-2 infected cell in which no cleaved-caspase-3 is visible (scale bar = 20 μ m).



Supplementary Figure 5.5 SARS-CoV-2 infection as well as H5N1 virus infection results in modest immune responses. The concentration of the cytokines which were measured in the supernatant of SARS-CoV-2 or H5N1 virus infected (A) NPCs, (B) mixed neural cultures and (C) Ngn2 co-cultures are displayed. The values represent the means of three independent experiments.

6

General discussion

IPSC-derived neural cultures

Since the establishment of human induced pluripotent stem cell (iPSC)-technology in 2007, the protocols to obtain iPSC-derived neural cells have improved tremendously. Early protocols considered neurons mature when they could fire a single action potential. More recent studies have demonstrated iPSC-derived brain organoids that exhibit waves of synchronized electrical activity³¹³. The work described in this thesis attempts to expand this toolbox and shows the enduring potential of iPSC technology for investigating human brain disorders.

In **Chapter 2** we present a novel protocol to efficiently differentiate iPSCs to functional astrocytes that support the formation and maturation of neuronal networks. This provides the opportunity to mature iPSC-derived neurons *in vitro* by supplementing human astrocytes instead of their rodent counterpart and thereby create a fully human co-culture system. Moreover, we were able to show reciprocal effects of co-culture on both astrocytes and neurons, which resulted in a more mature cellular identity of both cell types.

In vitro culture conditions are designed to mimic physiological development through recapitulation of key aspects of the *in vivo* environment. **Chapter 3** describes a model in which we transplant iPSC-derived neural cells into the brain of neonatal immunodeficient mice, providing the human cells with a more physiological environment to enhance their development. iPSC-derived astrocytes maintain their hominid characteristics after murine transplantation and develop a more complex morphology compared to 2D monolayer culture. Furthermore, we leveraged this model for preclinical screening of human antisense oligonucleotide (ASO) therapy for Angelman Syndrome (AS). We show that we can selectively reactivate the human paternal *UBE3A* allele by administering an ASO targeting *UBE3A*-ATS to immunodeficient mice transplanted with AS patient-derived neurons.

An example of how iPSCs can be used to study familial schizophrenia is described in **Chapter 4**. By performing linkage analysis combined with whole exome sequencing and reprogramming iPSC lines from patients and their unaffected siblings, we were able to identify rare genetic variants in patients and a cellular phenotype in iPSC-derived oligodendrocyte lineage cells. Mutant Chondroitin Sulfate Proteoglycan 4^{A131T/V901G} (CSPG4) showed defects in membrane trafficking, and OPCs from patients with the *CSPG4*^{A131T} mutation were less viable and exhibited decreased myelination potential. Consistent with these findings, diffusion tensor imaging of affected *CSPG4*^{A131T} mutation carriers displayed a reduction in brain white matter integrity. This study provides evidence in support of oligodendrocyte precursor cell dysfunction as a novel candidate mechanism of schizophrenia and supports the validity of combining family genetics and iPSC modeling to unravel underlying biological mechanisms of psychiatric disorders.

The value of having efficient access to an unlimited source of iPSC-derived neural cells is illustrated in **Chapter 5** by our work with Severe Acute Respiratory Syndrome Coronavirus-2 (SARS-CoV-2). The current COVID-19 pandemic has shown the importance of having a thriving scientific community. Neurological symptoms reported by COVID-19 patients sparked research into possible SARS-CoV-2 infections in the central nervous system (CNS). We infected different types of iPSC-derived neural cultures with SARS-CoV-2 to investigate the kinetics, cell tropism and associated immune response after infection. Definitive evidence of SARS-CoV-2 infection was found in only a small proportion of neurons without evidence for subsequent spread to other cells. We did not find evidence for infection in neural precursor cells (NPCs) or astrocytes. However, we did observe a strong increase of a subset of pro-inflammatory cytokines, raising the possibility that the neurological symptoms observed in patients might result from a heightened immune response to SARS-CoV-2 infection.

During the past decade, advances in iPSC technology have generated strong interest among biomedical researchers, especially in the field of neuroscience. iPSC-derived neural cells have been enthusiastically adopted to model human brain diseases. These cells contain the human genome of the individuals from whom the iPSCs are reprogrammed, and allow for elegant experimental designs through rapid advances in genome editing. This has created a greatly expanded opportunity to study the human brain, a tissue that previously was largely inaccessible for live cellular studies. Accordingly, many scientists have refocused their work on iPSC-based studies and published a plethora of studies utilizing this technique³¹⁴. Although brain disease modeling with iPSCs is an expensive and technically challenging endeavor, it offers great potential to answer fundamental questions about human neural cell functioning and development that have not been solved using other approaches. Consequently, interest in this technique continues to increase, as a model system for therapeutic drug discovery³¹⁵ or, for example, as a personalized treatment option for Parkinson's disease through delivery of iPSC-derived neural cells³¹⁶. To critically appraise their use, and position iPSC-technology in the wider technical and conceptual setting of brain research, an overview describing the current state of the field and guidance for designing iPSC-studies is described below.

Biological variability in iPSC cultures

Variability and reproducibility are a concern in all fields of experimental biology. The source for this variability can be both biological and technical. iPSC lines from different individuals have a different genetic background and will behave differently *in vitro* due to biological variability. Two iPSC clones created from one individual should be biologically identical, however due to technical variability these two clones can still behave different in seemingly identical culture conditions. These sources of variability contribute to the observed cellular heterogeneity in cultures used for experiments and should be taken into account when designing experiments. From a biological point of view, neurodevelopmental and psychiatric disorders are associated with subtle cellular phenotypes that could easily be lost in batch-to-batch variability. Understanding how genetic background and culture conditions affect variability and reproducibility is essential when attempting to identify disease-related phenotypes using iPSC-lines carrying pathogenic mutations or risk genotypes.

Traditional approaches to create iPSCs relied on random integration of the “Yamanaka factors” into somatic cells, causing every iPSC-clone from an individual to have a slightly different genetic identity. Integration-free methods circumvented this problem, however mutations that are not present in the parental line can still be detected³¹⁷. These are likely created during the initial cell divisions of the founder population of iPSCs. Genetic stability is reduced during the process of converting somatic cells to iPSCs – it is estimated that 10% of all somatic mutations observed in iPSCs are sub-clonal and not observed in the parental line^{318,319}. Although the majority of these mutations likely have no impact on gene expression or functioning, quality control checks for every iPSC-clone being considered for use in experiments should be performed, minimally to exclude the presence of gross genetic abnormalities and verify their ability to differentiate towards all three germ-layers.

When converting terminally differentiated somatic cells to iPSCs, the epigenetic landscape of the donor cell is transformed to resemble that of embryonic stem cells. Pluripotency genes become expressed and genes that previously determined donor cell identity are silenced through the methylation of their promotor region. It has been established that there can be residual expression of somatic genes due to incomplete DNA methylation, creating a so-called epigenetic memory of the somatic cell type of origin^{320,321}. These residual epigenetic markings tend to bias iPSCs towards easier differentiation along the lineage of the somatic cell type of origin. For example, iPSCs derived from blood will more easily differentiate towards hematopoietic progenitors³²². Therefore, when designing studies using iPSCs, it is not only important to consider the desired experimental cell type, but also the somatic donor cells used to create the iPSCs. Different cellular origins will already be responsible for epigenetic variation between iPSC-lines and could obscure potential cellular differences between lines. Notably in **Chapter 3**, we demonstrate that the imprinting of the paternal *UBE3A* allele in iPSC-derived neurons is preserved during the creation of iPSCs. A more

extensive study looked into multiple known imprinted genes in the iPSC-lines and donor cells of four individuals and found that imprinting is conserved in most actively transcribed genes³²³. Quality control screening of iPSC-clones helps to circumvent these problems as clone-specific effects heavily influence aberrant methylation at CpG sites in a non-random manner³²⁴.

The biggest source of biological variability arises from differences in the genetic background of donors. iPSC-clones of a single individual created from different somatic cell types, such as blood or skin, are more similar in their expression profile than iPSC-lines created from identical somatic cell types from different donors³²³. In iPSC-based studies of genetic disorders, one of two potential strategies is often implemented to circumvent these issues. One approach is to create iPSC-lines from multiple donors, ideally with a similar genotype at the locus of interest, in an effort to filter out the effect of different genetic backgrounds and identify the effect of the putatively causal genetic variant on a cellular phenotype. Alternatively, It is possible to create or correct a known causal variant in an iPSC-line using gene editing techniques such as CRISPR/Cas9⁹⁶ to create so-called isogenic lines – two cell lines that only differ in their genetic sequence at a locus of interest. This technique makes it possible to precisely edit the genome by directing the CRISPR/Cas9 complex to a specific location in the genome via a single guide RNA (sgRNA). The resulting double-stranded break is repaired based either on an exogenously supplied template or through nonhomologous DNA end joining (NHEJ). Using this approach, knock-out lines for a specific gene are created in an otherwise healthy genetic background. Template-based single nucleotide editing is done in order to introduce putatively causal missense variants and quantify their contribution to an observed cellular phenotype in a susceptible genetic background, or introduce a causal variant into an iPSC line with a healthy genetic background³²⁵. Even though targeted gene editing using CRISPR/Cas9 in human iPSCs remains a laborious process, it has become widely adopted in the iPSC field. As an alternative to targeted editing, CRISPR/Cas9 has evolved into a tool to manipulate gene expression using CRISPR interference (CRISPRi) and CRISPR activation (CRISPRa)³²⁶, respectively decreasing or increasing the expression of a gene-of-interest. For example, this approach has been used to successfully modulate the top-ranked schizophrenia-associated expressive trait loci, converging on a synaptic phenotype³²⁷.

When iPSC-lines are available to ensure proper controls and adequate sample size, this approach to cellular disease modeling is an excellent tool to answer fundamental questions about cellular processes and, potentially, unravel the etiology of genetic brain disorders. However, not all aspects of human brain development can be modeled *in vitro* using iPSCs. Attempting to link cellular phenotypes *in vitro* to symptoms observed in psychiatric patients remains challenging due to the complex and temporal nature of psychiatric symptoms. For example, the substantially reduced viability observed in iPSC-derived NPCs of patients with bipolar disorder is difficult to reconcile with their normal brain development³²⁸. It is important

to consider what phenotype is intended to be pursued for a given model and whether such a phenotype can be effectively recapitulated using iPSCs. Many protocols exist to create iPSC-derived neural cells – depending on the desired cell type and research question, some approaches are more suitable than others.

Technical variability in iPSC cultures

Batch to batch variability is a problem in all cell culture studies, even in widely used primary clonal cell lines³²⁹. Differentiation of iPSCs to mature neural cells typically takes several months. Different types of medium guide cells through progressive developmental stages until they mature into the desired cell type. Due to their lengthy nature and multiple stages during these protocols, variance in experimental outcomes is easily acquired through technical variability. Extensive literature has been written on how to differentiate iPSCs along different neural lineages. Early neural differentiation protocols often showed relatively low and variable yields of the desired cell type. During the past decade, substantial progress has been made in the efficiency and reproducibility of these protocols.

Already at the iPSC stage, different protocols exist to maintain pluripotency. Traditional approaches make use of a mouse or human feeder layer of embryonic fibroblasts¹. This feeder layer promotes pluripotency and helps maintain genetic stability. Growing iPSCs on a feeder layer is labor intensive and difficult to scale. Researchers have developed feeder-free systems by replacing the feeder layer with extracellular matrix proteins such as Matrigel and growing the iPSCs in Essential 8 or MTeSR medium, significantly reducing the required effort to maintain and expand iPSCs. However, when grown in these conditions, genomic stability of iPSCs is often reduced³³⁰. The latest iteration of feeder-free culture conditions uses StemFlex medium. In these conditions, iPSCs are more stress resilient, enhancing the efficiency of gene editing techniques³³¹.

Among the biggest challenges for realizing the therapeutic discovery potential of iPSC is translation of phenotypes observed in patients or putative causative genetic variants to cellular phenotypes that can be measured *in vitro*. The formulated hypothesis combined with practical and technical constraints will already determine certain decisions in experimental design and donor or cell type. To illustrate this with an example from this thesis, when the goal is to identify cellular phenotypes in a family with a high incidence of schizophrenia, in which the affected individuals carry a mutation in *CSPG4*¹¹, creating iPSCs from affected and unaffected siblings is an obvious choice. Alternatively, it is possible to create this identified genetic variant in a control iPSC-line, in which the effect of the variant can be studied outside a known susceptible genetic background, or correct the mutation in a patient-derived iPSC-line. Since *CSPG4/NG2* is highly expressed in OPCs, it makes sense to utilize protocols that are designed to obtain iPSC-derived OPCs. The

processing of (mutant) NG2 in these cells can be studied in 2D mono-layer cultures, a relatively simple culture system. Their maturation towards myelinating oligodendrocytes is best done in the presence of unmyelinated axons, adding an additional layer of complexity to the culture system.

An ideal culture system models the relevant aspects of a disorder and is simple enough to minimize technical variability. Brain cells require the physical presence of other neural cells to properly develop, e.g. neurons are unable to repetitively fire action potentials or develop into functional neuronal networks without the presence of astrocytes⁷³ and astrocytes show altered expression and increased maturity in co-culture with neurons (this thesis). Due to these reciprocal inductive interactions during the development of neural cells, iPSC-derived neural cultures typically require a heterogeneous population of cells. This creates more mature cells, but increases the chances of variability between cultures. Before initiating differentiation, a homogenous culture of iPSCs shows little technical variability when grown and expanded in defined culture conditions. During the differentiation towards neural cells these cultures become less homogenous and more batch-to-batch variation occurs. When differentiating iPSCs to NPCs, not all NPCs in the culture will be in the exact same developmental window, emphasized by the emergence of structural differences by NPCs forming neural rosettes. The emergence of these structures is heavily influenced by culture conditions, they will only form at a certain confluency of cells. Moreover, it is likely that not all cells will have fully committed towards the neural, or even ectoderm, lineage. The amount of variability in this process will vary between iPSC-lines and clones, potentially masking relevant cellular phenotypes. Variability at a progenitor stage can be reduced through magnetic or fluorescence activated cell sorting, purifying the cell population based on surface markers^{146,332}. A positive selection for NPC-markers combined with a negative selection for mature glial, neuronal and mesenchymal marker results in a more homogenous NPC population. This greatly reduces variability between different batches and iPSC-clones, facilitating in the identification a potential phenotype in the terminally differentiated cultures.

The large stereotypically-folded neocortex is one of the striking features of the human brain. iPSC-derived brain organoids attempt to add this feature to the toolbox for investigating human brain disorders *in vitro*. 3D organoids add another layer of complexity to iPSC models of human brain development and, consequently, show increased variability compared to 2D models³³³. Brain organoids exhibit features not observed in 2D neural cultures: dendritic spines are only observed in 3D models³³⁴, organoids recapitulate key events of cortical development such as cortical layering³³⁵, natural development of myelinating oligodendrocytes is only observed in brain organoids³³⁶. Organoid models largely rely on the self-organizational capability of neural stem cells. In a free-floating environment, stochastic asymmetrical division of neural stem cells gives rises to a three-dimensional tissue containing different mature neural cells in organized structures that resemble early brain development. Depending on the brain region of interest, it is possible to introduce

regional specificity using defined media³³⁷, or to fuse organoids with different regional identities to model cortico-striatal or -thalamic connections, then called assembloids^{338,339}. Researchers are adopting strategies to further enrich brain organoids with features relevant to their studies by fusing them with cells or tissue types that they are currently lacking, e.g. blood vessels³⁴⁰, microglia³⁴¹, choroid plexus cells³⁴², or muscle tissue to look at the functional output of brain organoids³³⁴.

Compared to 2D cultures, these approaches yield more mature cells. However, organoids have the disadvantage that they are highly heterogeneous. Early protocols introduced features not seen previously in iPSC-derived neural cultures, but their efficiency was limited due to variability in cell composition, morphology and tissue identity³⁴³. Technical refinements have addressed some issues regarding variability^{333,344}. Nevertheless, it remains a significant issue when growing brain organoids. Despite these, and likely future refinements, it is currently still necessary to take this expected variability in account when designing experiments using iPSC-derived brain cells, both in 2D and 3D culture systems. Moreover, phenotypic analysis of organoids can typically only be performed after dissociating the tissue, resulting in the termination of the culture, whereas in 2D cultures it is possible to monitor the development and activity of individual cells over time. A determination of the most suitable cell culture model should be based on the specific research question to be addressed – adding layers of complexity to a system will not necessarily improve the likelihood of identifying a disease associated phenotype.

Future of *in vitro* brain modeling

Technical advancements in culturing protocols, standardized commercial media and specialized culture environments have greatly reduced the batch-to-batch variability associated with iPSC-derived cultures³⁴⁵. Due to the logistical and financial burden traditionally associated with iPSC-based studies, they are often underpowered to detect relevant cellular phenotypes³⁴⁶. An increase in sample size will be necessary to detect more subtle cellular differences in iPSC-derived cultures. The first large-scale iPSC studies are emerging^{347–349}, however these studies focus on cellular variability at the pluripotent state. The differentiation of multiple iPSC-lines towards neural cells is a laborious and lengthy process, often requiring a multi-staged differentiation process and, consequently, careful monitoring of batch effects. Technical advancements such as single-cell RNA sequencing have made it possible to differentiate and identify multiple iPSC lines in a single well, so called “cell villages”³⁴⁸, potentially reducing technical, but not biological, variation between lines and dramatically reducing the associated logistical burden and necessary infrastructure. This approach is cost-effective and allows for the identification of common genetic variants associated with certain cellular phenotypes³⁵⁰. Currently, there are a limited

number of functional readouts that can be acquired from these pooled cultures. Individual donors need to be identified based on genomic information, restricting the potential to study living cells or donor-autonomous effects on cellular phenotypes. Novel techniques are being developed to interrogate cultures with a mixed or pooled genetic background, allowing for the study of neural cells with different genetic signatures in a single culture dish.

Besides mixing iPSCs of multiple donors, CRISPR/Cas9 is being used to create cultures with a mixed genetic background from a single donor. By using sgRNA libraries, it is possible to target every gene in the genome or in cell type/function specific genesets^{351,352}. The combination of CRISPRi/a and sgRNA libraries is being employed to perform genome-wide screens to systematically profile gene function. A recent successful study has used this approach to screen for regulators of a known disease-associated protein, PARKIN³⁵³, an E3 ligase mutated in familial Parkinson's disease. Using a pooled lentiviral sgRNA library, "cell villages" were created within a culture of HEK293 cells by knocking down single genes in individual cells. This screen identified regulators that influenced PARKIN protein levels; these were later verified in neuronal cultures. So far, very few genome-wide CRISPR screens have been performed to study brain disorders, likely a consequence of the substantial costs and time investment associated with iPSC-derived neural cultures. The first large scale CRISPRi screen in human iPSC-derived neurons utilized a defined sgRNA library to identify genes that are essential for neuronal survival³⁵⁴. Interestingly, follow-up single-cell RNA sequencing showed that knockdown of *UBA1*, a broadly expressed housekeeping gene, induced a plethora of downstream transcriptomic phenotypes in neurons, but not in iPSCs. Technical limitations prevent a large-scale analysis of gene-specific effects on neuronal functioning, since experimental readouts are needed to provide information on the genotype of the cells. An array approach combined with longitudinal imaging was used to look at the effect of 23 genes on neurite outgrowth³⁵⁴. This proof-of-concept screen already produced a wealth of data, uncovering genes that promote or hamper neurite outgrowth, providing insight into fundamental neurodevelopmental processes.

Aside from their use in a disease-related context, studies using human iPSC have revealed a great deal about normal human brain development. Extensive genetic analysis of up to 20-months old brain organoids revealed that iPSC-derived neural models can mature beyond the fetal stage and, at least partly, recapitulate the timing of human brain development³⁵⁵. These organoids follow an internal clock that synchronizes their development in the lab to that of human *in vivo* neurodevelopment. Interestingly, the developmental timing of human brain organoids is slower compared to macaque or chimpanzee organoids³⁵⁶, again highlighting the importance of using human cells to study human biology. Other studies have used human stem cells to identify human specific molecular cues involved in brain development. For example, human-specific *NOTCH2NL* genes were found to affect Notch signaling in radial glia and influence NPC maturation, possibly contributing to the emergence

of the large neocortex in humans³⁵⁷. Human brain evolution was studied by reintroducing an archaic variant of *NOVA1* into human iPSCs, using these cells researchers were able to create “Neanderthal brain organoids”³⁵⁸. This single variant caused changes in splicing variants of genes involved in neurodevelopment, cell proliferation and synapse formation. Neurons in these archaic organoids showed altered network activity and changes in synaptic density. These studies provide insight into the genetic pathways that were involved in the evolution of the human brain.

Technical advances have created new opportunities to combine genetic screens with functional readouts. Identifying the targeted gene in individual cells currently has to be done based on genomic information. Through single cell RNA sequencing, the effect of such a mutation on the transcriptome can be studied. Functional readouts can be implemented before identifying the targeted gene in genome-wide screens, but these are often relatively basic and limited to genes related to cell survival^{350,354}. Combining RNA sequencing and calcium imaging of individual cells in the developing human cortex has provided insight into the functional dynamics of individual cells³⁵⁹. At multiple timepoints during development, calcium dynamics of individual cells were measured in the presence of different compounds and followed by single cell RNA sequencing, creating a multimodal dataset for individual cells. Other studies have developed 3D high density multi-electrode arrays (MEA) to track the growth and electrical activity of neurons over time³⁶⁰ or expressed DNA barcodes for *in vitro* clonal lineage tracing³⁶¹. Future combinations of these techniques with high content imaging³⁶² and in situ sequencing³⁶³ can overcome many limitations currently associated with iPSC brain disease modeling. Batch-to-batch variability is less of an issue when the comparison is between individual cells. Clonal lineage tracing from individual iPSCs to mature neural cells can resolve the effect of iPSC biological heterogeneity on the developmental trajectory towards neural cells.

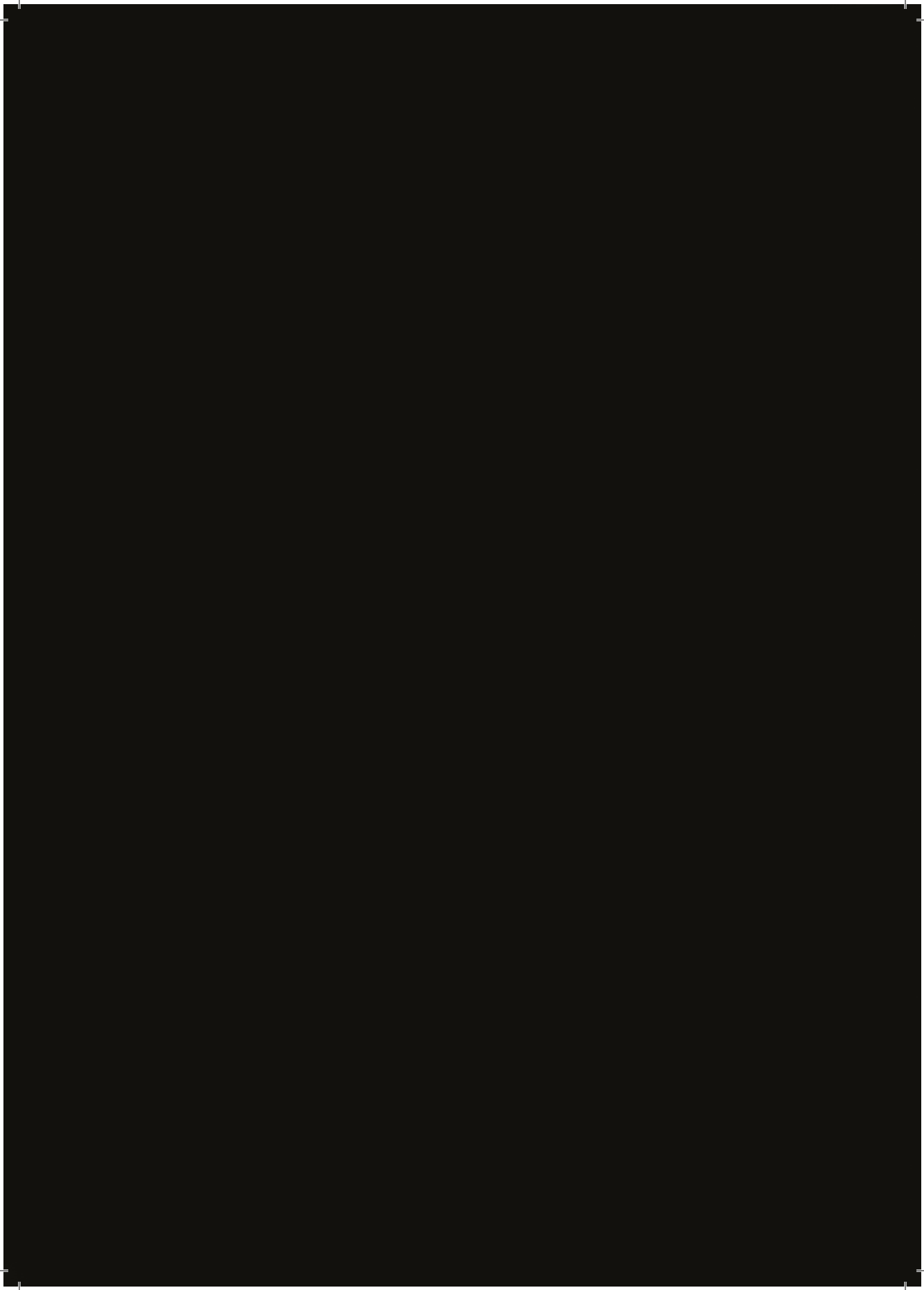
The incorporation of these modern molecular techniques to interrogate cells *in vitro* requires tailored cell culture vessels. Traditional well plates are often unsuited to perform detailed analysis on individual living cells. Custom devices have been designed to monitor neural cells during their maturation. The fabrication of these cell culture chips is a matter of significant biomedical engineering research^{364,365}. Organ-on-a-chip and more specifically brain-on-a-chip (BoC) devices can incorporate microfluidics, electrodes and 3D compartmentalized structures in a single translucent vessel. These chips attempt to mimic the structural and functional aspects of the brain in order to provide iPSC-derived neural cells with a more *in vivo*-like environment. BoC-devices try to minimize cell culture variability by more closely defining the environment in which the cells are grown. Combined with the ability to perform continuous functional readouts, their small footprint make these chips an excellent tool for genetic or drug screens.

What constitutes a BoC is loosely defined, in general a cell culture vessel with an additional engineered feature to increase cell functioning or experimental assays is considered a BoC device. Microfluidics are often incorporated into BoC devices, providing additional control over the flow of nutrients and a more natural 3D scaffold for cells. An artificial model of the blood-brain-barrier can be created in such a chip in which iPSC-derived microvascular endothelial cells and astrocytes form a tight layer of cells separating two microfluidic channels³⁶⁶. This model recapitulates molecular, structural and functional blood-brain-barrier properties, including trans-endothelial electrical resistance and the creation of a specialized transporter barrier. Microfluidics can also be used to create growth factor gradients, more closely mimicking neural developmental events *in vivo*³⁶⁷. Other approaches make use of physical barriers to direct axonal connections between two MEAs in a single chip³⁶⁸ or recreate anatomical features of the human brain such as the hippocampus³⁶⁹ or cortical folding³⁷⁰. BoC devices that incorporate high density MEAs with optical stimulation can be used to track the migration of cells, differentiate between electrical signals of multiple neurons or stimulate defined clusters of neurons in a network using laser-targeted optogenetics or direct electrical microstimulation³⁷¹. On a larger scale, spinning bioreactors have been developed to address some of the variability observed when creating brain organoids^{337,372}. These small bioreactors significantly reduce the associated costs and improve the functioning of neural cells in the organoid. This increases the scalability of brain organoid cultures and their potential for studying the effect of pharmacological compounds or genetic variants on complex neural networks.

Advances in BoC models have created novel cellular models of the human brain. The innovation of molecular techniques to influence and monitor individual cells or complete neural networks have provided scientists with powerful tools to study iPSC-derived neural cells. Combined with forward-genetics, technical breakthroughs are providing increasingly robust platforms to study the effect of genetic variants on the development of cellular phenotypes *in vitro* and, hopefully, elucidate the underlying etiology of psychiatric and neurodevelopmental disorders.

Concluding remarks

It is important to consider what it is that is being modeled when using iPSC-derived neural cultures to study brain disorders. From a biological perspective most individuals suffering from neurodevelopmental or psychiatric disorders present with almost imperceivable cellular phenotypes. Their symptoms are mostly behavioral and require trained physicians to be properly diagnosed, still leaving diagnoses subjective and complex with many overlapping symptoms between disorders. For all intents and purposes, the fundamental architecture of the brain has developed normally in the setting of psychiatric disorders. Early iPSC-studies successfully focused on severe monogenic disorders, using iPSC-derived neural cells to study the effect of a mutation on specific proteins. With increased interest in iPSC disease modeling, there has been an increase in reports overinterpreting findings in an attempt to link *in vitro* findings to an *in vivo* phenotype observed in patients. iPSC-technology has provided scientists with nearly limitless access to living brain tissue to manipulate and study, and increasingly advanced protocols for directed differentiation. Therefore, it is critical for the field to focus on the question of how can brain disorders be most optimally studied and attempt to create the most faithful representation of a human brain *in vitro*. Although protocols will continue to improve, it is unlikely that it will become possible to recreate a human brain in a dish without crossing ethical boundaries. Increasing knowledge on the etiology of human brain disorders will require researchers who perform iPSC-based studies to utilize data from other fields of research to formulate a defined hypothesis and adopt the proper model to efficiently answer these questions. The broad adaptation of iPSCs into all fields of human biology has accelerated the development of tools available to researchers. Combining disciplines will further elucidate the processes involved in the development of the healthy and diseased human brain, and hopefully provide novel treatments for patients suffering from brain diseases.



Appendices

Summary

Samenvatting

Curriculum Vitae

PhD portfolio

Acknowledgements

List of publications

References

Summary

Induced pluripotent stem cell (iPSC)-technology has created the ability to study the development of patient-derived neural cells *in vitro* and identify cellular phenotypes. The potential of this relatively new field has sparked great interest in the field of neuroscience and beyond. The work presented in this thesis attempts to improve the techniques to differentiate iPSCs towards cells of the neural lineage and demonstrates how these cells can be leveraged to study brain disorders. We describe a protocol to generate functional astrocytes that are able to support the development and maturation of neural networks, creating the opportunity to study completely human astrocyte and neuron co-cultures. Patient-derived iPSCs are used for an *in vivo* preclinical screening of human antisense oligonucleotide therapy to treat Angelman Syndrome, restoring the expression of the causal gene defect in neurons. By performing genetic analysis on a family with a high incidence of schizophrenia and creating iPSCs from affected and unaffected siblings, we were able to identify a causative variant highly expressed in oligodendrocyte precursor cells, and show that these cells, when derived from patients, were less likely to mature into myelinating oligodendrocytes. The value of having quick access to iPSC-derived neural cells is demonstrated in our work with Severe Acute Respiratory Syndrome Coronavirus-2 (SARS-CoV-2), the virus responsible for the current pandemic. Patients often experience neurological symptoms during or following infection. We show that although SARS-CoV-2 primarily infects neurons, it displays limited replication in neural cultures but does induce the production of pro-inflammatory cytokines. Together, iPSC technology has provided novel insights into the processes involved in healthy and diseased human brain development.

Samenvatting

De techniek om geïnduceerde pluripotente stamcellen (iPSC) te maken heeft de mogelijkheid gecreëerd om de ontwikkeling van patiënt-afgeleide neurale cellen te bestuderen *in vitro* en om mogelijke cellulaire fenotypes te identificeren. Dit relatief nieuwe onderzoeksveld heeft veel potentie en wordt daarom met veel interesse gevolgd door hersenwetenschappers. Het werk dat wordt beschreven in dit proefschrift doet een poging om de bestaande technieken voor iPSC differentiatie naar neurale cellen te verbeteren en laat zien hoe deze technieken gebruikt kunnen worden om hersenziekten te bestuderen. We beschrijven een nieuw protocol om functionele astrocyten te maken van iPSCs die de ontwikkeling en maturatie van neurale netwerken ondersteunen. Dit maakt het mogelijk om volledig humane co-culturen van neuronen en astrocyten te bestuderen. iPSCs van Angelman syndroom patiënten worden gebruikt voor een *in vivo* preklinische screening van een humaan-specifieke antisense oligonucleotiden therapie, hiermee is het mogelijk om alleen in neuronen de expressie van het causatieve gen voor deze ziekte te herstellen. Door genetische analyse uit te voeren binnen een familie met een hoge incidentie van schizofrenie en iPSCs te maken van zieke en gezonde familieleden hebben we een genetische variant geïdentificeerd die hoog tot expressie komt in de voorlopercellen van oligodendrocyten. Deze cellen ontwikkelen zich minder goed tot myeliniserende oligodendrocyten als ze gemaakt worden van patiënt-afgeleide iPSCs. Dat het hebben van snelle toegang tot iPSC-afgeleide neurale cellen zeer waardevol is werd duidelijk door ons werk met Severe Acute Respiratory Syndrome Coronavirus-2 (SARS-CoV-2), het virus verantwoordelijk voor de huidige pandemie. We laten zien dat SARS-CoV-2 vooral neuronen infecteert, dat het zich daar slecht kan repliceren, maar wel de productie van pro-inflammatoire cytokines induceert. Alles bij elkaar genomen heeft de iPSC techniek nieuwe inzichten opgeleverd over de processen die betrokken zijn bij gezonde hersenontwikkeling en tijdens ziekte.

Curriculum Vitae

Bas Lendemeijer was born on March 11th, 1990 in 's-Hertogenbosch, The Netherlands. In 2012 he attained a BSc degree in Biomedical Sciences from the VU University in Amsterdam and completed his thesis research on animal models to evaluate the efficacy of cochlear implants. Afterwards he commenced a neuroscience research master at the Erasmus University Medical Centre in Rotterdam and participated in the Honours Exchange programme between Amsterdam and Rotterdam. After finishing his thesis project on the transplantation of human induced pluripotent stem cell-derived neural cells into the rodent brain in 2014, he started his PhD research project in the lab of Prof. dr. SA Kushner at the department of Psychiatry at the ErasmusMC in Rotterdam.

PhD portfolio

Name:	Bas Lendemeijer
Phd period:	2014-2021
Department:	Psychiatry
Promotor:	prof. dr. S.A. Kushner prof. dr. W.J.G. Hoogendijk
Co-promotor:	dr. F.M.S. de Vrij
Research school:	Research School of Neuroscience (ONWAR)

Training

FACSAria III Operator training, <i>BD biosciences, Leuven, Belgium</i>	2015
Laboratory Animal Science (Article 9), <i>ErasmusMC, Rotterdam, Netherlands</i>	2015
Teach the teacher, <i>EUR, Rotterdam, Netherlands</i>	2015
Translational approaches in schizophrenia, <i>ONWAR, Utrecht, Netherlands</i>	2015
Scientific integrity, <i>ErasmusMC, Rotterdam, Netherlands</i>	2015
International Astrocyte School, <i>Bertinoro, Italy</i>	2017
Single cell transcriptomics, <i>Cajal online lecture series</i>	2020

Presentations and conferences

Dutch ENP meeting, <i>Lunteren, Netherlands (poster presentation)</i>	2014
ENCODS, <i>Sesimbra, Portugal (poster presentation)</i>	2015
Dutch Neuroscience meeting, <i>Lunteren, Netherlands (oral presentation)</i>	2016
Dutch Neuroscience meeting, <i>Lunteren, Netherlands (poster presentation)</i>	2017
Neurodevelopmental disorders day, <i>Nijmegen, Netherlands (oral presentation)</i>	2017
Dutch Neuroscience meeting, <i>Lunteren, Netherlands</i>	2018
Annual ISCCR meeting, <i>Amsterdam, Netherlands</i>	2018
Annual hDMT consortium meeting, <i>Rotterdam, Netherlands (oral presentation)</i>	2018
Dutch Neuroscience meeting, <i>Lunteren, Netherlands (poster presentation)</i>	2019
Donders discussions, <i>Nijmegen, Netherlands (oral presentation)</i>	2019
Annual hDMT consortium meeting, <i>Rotterdam, Netherlands (oral presentation)</i>	2019
Dutch Neuroscience meeting, <i>Lunteren, Netherlands (oral presentation)</i>	2021

Teaching

Junior Med School, summer internship	2015
Supervising systematic review medical students	2016-2020
Supervising scientific report medical students	2016
Ratna Mellema, master biomedical sciences literature review	2019
Iris Gombert, master biomedical sciences literature review	2020

Bachelor/master thesis

Siawosh Eskandari, bachelor internship medicine	2015
Sara Gordillo Sampedro, Neuroscience master internship	2016-2018
Roxane Wouters, bachelor internship medical laboratory sciences	2017
Hilde Smeenk, Neuroscience master internship	2017-2019
Shreekara Gopalakrishna, Molecular medicine master internship	2018
Anna Lopez Marti, Molecular medicine master internship	2019
Mirle Buurma, Neuroscience master internship	2019-2021

List of publications

In this thesis:

Rapid specification of human pluripotent stem cells to functional astrocytes supporting neural network activity

Lendemeijer B, Mossink B, Hijazi S, Sampedro SG, Shpak G, Slump DE, Unkel M, van den Hout MCGN, van IJcken WFJ, Hoogendijk WJG, Kasri NN, de Vrij FMS, Kushner SA. (*Manuscript in preparation*)

In vivo preclinical screening of human antisense oligonucleotide therapy for Angelman Syndrome

Lendemeijer B[#], Buurma M[#], Smeenk H, Slump DE, Milazzo C, Mientjes E, Hoogendijk WJG, Elgersma Y, de Vrij FMS[#], Kushner SA[#]. (*Manuscript in preparation*)

Candidate CSPG4 Mutations and Induced Pluripotent Stem Cell Modeling Implicate Oligodendrocyte Progenitor Cell Dysfunction in Familial Schizophrenia

de Vrij FMS[#], Bouwkamp CG[#], Gunhanlar N[#], Shpak G, **Lendemeijer B**, Baghdadi M, Gopalakrishna S, Ghazvini M, Li TM, Quadri M, Olgati S, Breedveld GJ, Coesmans M, Mientjes E, de Wit T, Verheijen FW, Beverloo HB, Cohen D, Kok RM, Bakker PR, Nijburg A, Spijker AT, Haffmans PMJ, Hoencamp E, Bergink V; GROUP Study Consortium, Vorstman JA, Wu T, Olde Loohuis LM, Amin N, Langen CD, Hofman A, Hoogendijk WJ, van Duijn CM, Ikram MA, Vernooij MW, Tiemeier H, Uitterlinden AG, Elgersma Y, Distel B, Gribnau J, White T, Bonifati V, Kushner SA. (*Molecular Psychiatry*, 24(5):757-771)

Replication Kinetics, Cell Tropism, and Associated Immune Responses in SARS-CoV-2- and H5N1 Virus-Infected Human Induced Pluripotent Stem Cell-Derived Neural Models.

Bauer L[#], **Lendemeijer B**[#], Leijten L, Embregts CWE, Rockx B, Kushner SA, de Vrij FMS[#], van Riel D[#]. (*mSphere*, e0027021)

[#] Authors contributed equally

Other publications:

SOX10 Single Transcription Factor-Based Fast and Efficient Generation of Oligodendrocytes from Human Pluripotent Stem Cells.

García-León JA, Kumar M, Boon R, Chau D, One J, Wolfs E, Eggermont K, Berckmans P, Gunhanlar N, de Vrij F, **Lendemeijer B**, Pavie B, Corthout N, Kushner SA, Dávila JC, Lambrichts I, Hu WS, Verfaillie CM. (*Stem Cell Reports*, 10(2):655-672)

A simplified protocol for differentiation of electrophysiologically mature neuronal networks from human induced pluripotent stem cells.

Gunhanlar N, Shpak G, van der Kroeg M, Gouty-Colomer LA, Munshi ST, **Lendemeijer B**, Ghazvini M, Dupont C, Hoogendijk WJG, Gribnau J, de Vrij FMS, Kushner SA. (*Molecular Psychiatry*, 23(5):1336-1344)

Novel genetic loci affecting facial shape variation in humans.

Xiong Z, Dankova G, Howe LJ, Lee MK, Hysi PG, de Jong MA, Zhu G, Adhikari K, Li D, Li Y, Pan B, Feingold E, Marazita ML, Shaffer JR, McAloney K, Xu SH, Jin L, Wang S, de Vrij FM, **Lendemeijer B**, Richmond S, Zhurov A, Lewis S, Sharp GC, Paternoster L, Thompson H, Gonzalez-Jose R, Bortolini MC, Canizales-Quinteros S, Gallo C, Poletti G, Bedoya G, Rothhammer F, Uitterlinden AG, Ikram MA, Wolvius E, Kushner SA, Nijsten TE, Palstra RT, Boehringer S, Medland SE, Tang K, Ruiz-Linares A, Martin NG, Spector TD, Stergiakouli E, Weinberg SM, Liu F, Kayser M; International Visible Trait Genetics (VisiGen) Consortium. (*Elife*, 8:e49898)

A functional variant in the miR-142 promoter modulating its expression and conferring risk of Alzheimer disease.

Ghanbari M, Munshi ST, Ma B, **Lendemeijer B**, Bansal S, Adams HH, Wang W, Goth K, Slump DE, van den Hout MCGN, van IJcken WFJ, Bellusci S, Pan Q, Erkeland SJ, de Vrij FMS, Kushner SA, Ikram MA. (*Human Mutation*, 40(11):2131-2145)

Conserved UBE3A subcellular distribution between human and mice is facilitated by non-homologous isoforms.

Zampeta FI, Sonzogni M, Niggli E, **Lendemeijer B**, Smeenk H, de Vrij FMS, Kushner SA, Distel B, Elgersma Y. (*Human Molecular Genetics*, 4;29(18):3032-3043)

Appendices

Acknowledgements

Everything in this thesis has been achieved with the support of friends and colleagues around me. Seven years is a long time, during which I've had to pleasure to meet and work with many different people. I couldn't possibly thank everyone enough in a few words, so I will give them a shout out in my own way.

I would like to use this space to thank my promotor and co-promotor, prof. dr. Steven Kushner, prof. dr. Witte Hoogendijk and dr. Femke de Vrij. Thank you for giving me the opportunity to work on my PhD under your supervision. I'll be forever grateful for the amount of trust you've put in me to figure things out on my own and how, at the same time, you were always available when I needed help.

A special thanks goes out to the committee members, prof. dr. Elly Hol, dr. Nael Nadif Kasri, dr. Geeske van Woerden, prof. dr. Joost Gribnau and dr. ing. Debby van Riel, for kindly accepting to be part of this process and their critical reading of my thesis.

Finally, a Big thank you to all the past and present members of the lab!
Your scientific contributions are greatly appreciated and, more importantly, you made coming to work something to look forward to.

References

1. Takahashi, K. *et al.* Induction of pluripotent stem cells from adult human fibroblasts by defined factors. *Cell* **131**, 861–72 (2007).
2. Azevedo, F. A. C. *et al.* Equal numbers of neuronal and nonneuronal cells make the human brain an isometrically scaled-up primate brain. *J. Comp. Neurol.* **513**, 532–541 (2009).
3. Moser, E. I., Kropff, E. & Moser, M. B. Place cells, grid cells, and the brain's spatial representation system. *Annual Review of Neuroscience* vol. 31 69–89 (2008).
4. Prasad, S. & Galetta, S. L. Anatomy and physiology of the afferent visual system. in *Handbook of Clinical Neurology* vol. 102 3–19 (Elsevier, 2011).
5. Stroup, T. S., Alves, W. M., Hamer, R. M. & Lieberman, J. A. Clinical trials for antipsychotic drugs: design conventions, dilemmas and innovations. *Nat. Rev. Drug Discov.* **5**, 133–146 (2006).
6. Snyder, S. H., Banerjee, S. P., Yamamura, H. I. & Greenberg, D. Drugs, Neurotransmitters, and Schizophrenia. *Science (80-.)*. **184**, 1243–1253 (1974).
7. Creese, I., Burt, D. R. & Snyder, S. H. Dopamine receptor binding predicts clinical and pharmacological potencies of antischizophrenic drugs. *Science (80-.)*. **192**, 481–483 (1976).
8. Wang, T. *et al.* Large-scale targeted sequencing identifies risk genes for neurodevelopmental disorders. *Nat. Commun.* **11**, 4932 (2020).
9. Ripke, S. *et al.* Biological insights from 108 schizophrenia-associated genetic loci. *Nature* **511**, 421–427 (2014).
10. Stahl, E. A. *et al.* Genome-wide association study identifies 30 loci associated with bipolar disorder. *Nat. Genet.* **51**, 793–803 (2019).
11. de Vrij, F. M. *et al.* Candidate CSPG4 mutations and induced pluripotent stem cell modeling implicate oligodendrocyte progenitor cell dysfunction in familial schizophrenia. *Mol. Psychiatry* **24**, 757–771 (2019).
12. Marshall, C. R. *et al.* Contribution of copy number variants to schizophrenia from a genome-wide study of 41,321 subjects. *Nat. Genet.* **49**, 27–35 (2017).
13. Sullivan, P. F. The Genetics of Schizophrenia. *PLoS Med.* **2**, e212 (2005).
14. Steeds, H., Carhart-Harris, R. L. & Stone, J. M. Drug models of schizophrenia. *Ther. Adv. Psychopharmacol.* **5**, 43–58 (2015).
15. Harris, J. C. Animal models of neurodevelopmental disorders with behavioral phenotypes. *Curr. Opin. Psychiatry Publish Ah*, 87–93 (2020).
16. Niemi, M. E. K. *et al.* Common genetic variants contribute to risk of rare severe neurodevelopmental disorders. *Nature* **562**, 268–271 (2018).
17. Parenti, I., Rabaneda, L. G., Schoen, H. & Novarino, G. Neurodevelopmental Disorders: From Genetics to Functional Pathways. *Trends Neurosci.* **43**, 608–621 (2020).
18. Molnár, Z. & Clowry, G. Cerebral cortical development in rodents and primates. in *Progress in Brain Research* vol. 195 45–70 (Elsevier B.V., 2012).
19. Zilles, K., Palomero-Gallagher, N. & Amunts, K. Development of cortical folding during evolution and ontogeny. *Trends Neurosci.* **36**, 275–284 (2013).
20. Nowakowski, T. J., Pollen, A. A., Sandoval-Espinosa, C. & Kriegstein, A. R. Transformation of the

- Radial Glia Scaffold Demarcates Two Stages of Human Cerebral Cortex Development. *Neuron* **91**, 1219–1227 (2016).
21. Molnár, Z. *et al.* New insights into the development of the human cerebral cortex. *J. Anat.* **235**, 432–451 (2019).
22. Hansen, D. V., Lui, J. H., Parker, P. R. L. & Kriegstein, A. R. Neurogenic radial glia in the outer subventricular zone of human neocortex. *Nature* **464**, 554–561 (2010).
23. Hodge, R. D. *et al.* Conserved cell types with divergent features in human versus mouse cortex. *Nature* **573**, 61–68 (2019).
24. Oberheim, N. A., Wang, X., Goldman, S. & Nedergaard, M. Astrocytic complexity distinguishes the human brain. *Trends Neurosci.* **29**, 547–553 (2006).
25. Oberheim, N. A. *et al.* Uniquely hominid features of adult human astrocytes. *J. Neurosci.* **29**, 3276–87 (2009).
26. Amin, N. *et al.* A rare missense variant in RCL1 segregates with depression in extended families. *Mol. Psychiatry* **23**, 1120–1126 (2018).
27. Elkabetz, Y. *et al.* Human ES cell-derived neural rosettes reveal a functionally distinct early neural stem cell stage. *Genes Dev.* **22**, 152–165 (2008).
28. Dhara, S. K. & Stice, S. L. Neural differentiation of human embryonic stem cells. *Journal of Cellular Biochemistry* vol. 105 633–640 (2008).
29. Svendsen, C. N., Caldwell, M. A. & Ostenfeld, T. Human neural stem cells: Isolation, expansion and transplantation. in *Brain Pathology* vol. 9 499–513 (International Society of Neuropathology, 1999).
30. Schmidt, R. & Plath, K. The roles of the reprogramming factors Oct4, Sox2 and Klf4 in resetting the somatic cell epigenome during induced pluripotent stem cell generation. *Genome Biol.* **13**, 251 (2012).
31. Bock, C. *et al.* Reference Maps of Human ES and iPS Cell Variation Enable High-Throughput Characterization of Pluripotent Cell Lines. *Cell* **144**, 439–452 (2011).
32. Osafune, K. *et al.* Marked differences in differentiation propensity among human embryonic stem cell lines. *Nat. Biotechnol.* **26**, 313–315 (2008).
33. Choi, J. *et al.* A comparison of genetically matched cell lines reveals the equivalence of human iPSCs and ESCs. *Nat. Biotechnol.* **33**, 1173–1181 (2015).
34. Brennand, K. J. *et al.* Modelling schizophrenia using human induced pluripotent stem cells. *Nature* **473**, 221–5 (2011).
35. Gunhanlar, N. *et al.* A simplified protocol for differentiation of electrophysiologically mature neuronal networks from human induced pluripotent stem cells. *Mol. Psychiatry* **23**, 1336–1344 (2017).
36. Shi, Y., Kirwan, P., Smith, J., Robinson, H. P. C. & Livesey, F. J. Human cerebral cortex development from pluripotent stem cells to functional excitatory synapses. *Nat. Neurosci.* **15**, 477–86, S1 (2012).
37. Abud, E. M. *et al.* iPSC-Derived Human Microglia-like Cells to Study Neurological Diseases. *Neuron* **94**, 278–293.e9 (2017).
38. Kriks, S. *et al.* Dopamine neurons derived from human ES cells efficiently engraft in animal models of Parkinson's disease. *Nature* **480**, 547–551 (2011).
39. Schafer, S. T. *et al.* Pathological priming causes developmental gene network heterochronicity in autistic subject-derived neurons. *Nat. Neurosci.* **22**, 243–255 (2019).

40. Zhang, Y. *et al.* Rapid single-step induction of functional neurons from human pluripotent stem cells. *Neuron* **78**, 785–98 (2013).
41. Mossink, B. *et al.* Cadherin-13 is a critical regulator of GABAergic modulation in human stem-cell-derived neuronal networks. *Mol. Psychiatry* 1–18 (2021) doi:10.1038/s41380-021-01117-x.
42. García-León, J. A. *et al.* SOX10 Single Transcription Factor-Based Fast and Efficient Generation of Oligodendrocytes from Human Pluripotent Stem Cells. *Stem Cell Reports* **10**, 655–672 (2018).
43. Canals, I. *et al.* Rapid and efficient induction of functional astrocytes from human pluripotent stem cells. *Nat. Methods* **15**, 693–696 (2018).
44. Frega, M. *et al.* Neuronal network dysfunction in a model for Kleefstra syndrome mediated by enhanced NMDAR signaling. *Nat. Commun.* **10**, 4928 (2019).
45. García-León, J. A. *et al.* Generation of oligodendrocytes and establishment of an all-human myelinating platform from human pluripotent stem cells. *Nat. Protoc.* **15**, 3716–3744 (2020).
46. Kaur, R., Sidhu, P. & Singh, S. What failed BIA 10-2474 Phase I clinical trial? Global speculations and recommendations for future Phase I trials. *J. Pharmacol. Pharmacother.* **7**, 120 (2016).
47. van Esbroeck, A. C. M. *et al.* Activity-based protein profiling reveals off-target proteins of the FAAH inhibitor BIA 10-2474. *Science (80-.)*. **356**, 1084–1087 (2017).
48. Bonini, S. & Rasi, G. First-in-Human Clinical Trials — What We Can Learn from Tragic Failures. *N. Engl. J. Med.* **375**, 1788–1789 (2016).
49. Brøsen, K., Funck-Brentano, C., Kroemer, H. K., Pirmohamed, M. & Schwab, M. Open letter on access to the BIA 10-2474 clinical trial data. *Lancet* **389**, 156 (2017).
50. Rinaldi, C. & Wood, M. J. A. Antisense oligonucleotides: the next frontier for treatment of neurological disorders. *Nat. Rev. Neurol.* **14**, 9–21 (2018).
51. Roberts, T. C., Langer, R. & Wood, M. J. A. Advances in oligonucleotide drug delivery. *Nat. Rev. Drug Discov.* **19**, 673–694 (2020).
52. Finkel, R. S. *et al.* Nusinersen versus Sham Control in Infantile-Onset Spinal Muscular Atrophy. *N. Engl. J. Med.* **377**, 1723–1732 (2017).
53. Aartsma-Rus, A. & Corey, D. R. The 10th Oligonucleotide Therapy Approved: Golodirsen for Duchenne Muscular Dystrophy. *Nucleic Acid Ther.* **30**, 67–70 (2020).
54. Kim, J. *et al.* Patient-Customized Oligonucleotide Therapy for a Rare Genetic Disease. *N. Engl. J. Med.* **381**, 1644–1652 (2019).
55. Chi, X., Gatti, P. & Papoian, T. Safety of antisense oligonucleotide and siRNA-based therapeutics. *Drug Discov. Today* **22**, 823–833 (2017).
56. Dagli, A. I., Mueller, J. & Williams, C. A. *Angelman Syndrome*. *GeneReviews®* vol. 2 (University of Washington, Seattle, 1993).
57. Rotaru, D. C., Mientjes, E. J. & Elgersma, Y. Angelman Syndrome: From Mouse Models to Therapy. *Neuroscience* vol. 445 172–189 (2020).
58. Silva-Santos, S. *et al.* Ube3a reinstatement identifies distinct developmental windows in a murine Angelman syndrome model. *J. Clin. Invest.* **125**, 2069–2076 (2015).
59. Wolter, J. M. *et al.* Cas9 gene therapy for Angelman syndrome traps Ube3a-ATS long non-coding RNA. *Nature* **587**, 281–284 (2020).
60. Zhao, X. & Bhattacharyya, A. Human Models Are Needed for Studying Human Neurodevelopmental

- Disorders. *Am. J. Hum. Genet.* **103**, 829–857 (2018).
61. Owen, M. J., Sawa, A. & Mortensen, P. B. Schizophrenia. *Lancet* **388**, 86–97 (2016).
62. Del Barrio, V. Diagnostic and statistical manual of mental disorders. in *The Curated Reference Collection in Neuroscience and Biobehavioral Psychology* (American Psychiatric Association, 2016). doi:10.1016/B978-0-12-809324-5.05530-9.
63. van der Lee, A., de Haan, L. & Beekman, A. Schizophrenia in the Netherlands: Continuity of Care with Better Quality of Care for Less Medical Costs. (2016) doi:10.1371/journal.pone.0157150.
64. Marwaha, S. & Johnson, S. Schizophrenia and employment. *Soc. Psychiatry Psychiatr. Epidemiol.* **39**, 337–349 (2004).
65. Harrow, M. & Jobe, T. H. Does long-term treatment of schizophrenia with antipsychotic medications facilitate recovery? *Schizophr. Bull.* **39**, 962–965 (2013).
66. Bramness, J. G. *et al.* Amphetamine-induced psychosis - a separate diagnostic entity or primary psychosis triggered in the vulnerable? *BMC Psychiatry* **12**, 221 (2012).
67. Lieberman, J. A., Kane, J. M. & Alvir, J. Provocative tests with psychostimulant drugs in schizophrenia. *Psychopharmacology (Berl)*. **91**, 415–433 (1987).
68. Howes, O. D. & Kapur, S. The dopamine hypothesis of schizophrenia: version III—the final common pathway. *Schizophr. Bull.* **35**, 549–62 (2009).
69. Winton-Brown, T. T., Fusar-Poli, P., Ungless, M. A. & Howes, O. D. Dopaminergic basis of salience dysregulation in psychosis. *Trends in Neurosciences* vol. 37 85–94 (2014).
70. de Hoz, L. & Simons, M. The emerging functions of oligodendrocytes in regulating neuronal network behaviour. *BioEssays* **37**, 60–69 (2015).
71. Vasile, F., Dossi, E. & Rouach, N. Human astrocytes: structure and functions in the healthy brain. *Brain Struct. Funct.* **222**, 2017–2029 (2017).
72. Verkhratsky, A. & Nedergaard, M. Physiology of Astroglia. *Physiol. Rev.* **98**, 239–389 (2018).
73. Deemyad, T., Lüthi, J. & Spruston, N. Astrocytes integrate and drive action potential firing in inhibitory subnetworks. *Nat. Commun.* **9**, 1–13 (2018).
74. Kelly, S. *et al.* Widespread white matter microstructural differences in schizophrenia across 4322 individuals: results from the ENIGMA Schizophrenia DTI Working Group. *Mol. Psychiatry* (2017) doi:10.1038/mp.2017.170.
75. Proctor, D. T. *et al.* Axo-glial communication through neurexin-neuroligin signaling regulates myelination and oligodendrocyte differentiation. *Glia* (2015) doi:10.1002/glia.22875.
76. Bernstein, H.-G., Steiner, J., Guest, P. C., Dobrowolny, H. & Bogerts, B. Glial cells as key players in schizophrenia pathology: recent insights and concepts of therapy. *Schizophr. Res.* **161**, 4–18 (2015).
77. Jaffe, A. E. *et al.* Developmental and genetic regulation of the human cortex transcriptome illuminate schizophrenia pathogenesis. *Nat. Neurosci.* **21**, 1117–1125 (2018).
78. Gandal, M. J. *et al.* Transcriptome-wide isoform-level dysregulation in ASD, schizophrenia, and bipolar disorder. *Science (80-.)*. **362**, eaat8127 (2018).
79. Gandal, M. J. *et al.* Shared molecular neuropathology across major psychiatric disorders parallels polygenic overlap. *Science (80-.)*. **359**, 693–697 (2018).
80. Schork, A. J. *et al.* A genome-wide association study of shared risk across psychiatric disorders implicates gene regulation during fetal neurodevelopment. *Nat. Neurosci.* **22**, 353–361 (2019).

81. Lundgaard, I., Osório, M. J., Kress, B. T., Sanggaard, S. & Nedergaard, M. White matter astrocytes in health and disease. *Neuroscience* **276**, 161–173 (2014).
82. Simons, M. & Nave, K. A. Oligodendrocytes: Myelination and axonal support. *Cold Spring Harbor Perspectives in Biology* vol. 8 (2016).
83. Mighdoll, M. I., Tao, R., Kleinman, J. E. & Hyde, T. M. Myelin, myelin-related disorders, and psychosis. *Schizophr. Res.* **161**, 85–93 (2015).
84. Scholz, J., Klein, M. C., Behrens, T. E. J. & Johansen-Berg, H. Training induces changes in white-matter architecture. *Nat. Neurosci.* **12**, 1370–1371 (2009).
85. Sampaio-Baptista, C. *et al.* Motor skill learning induces changes in white matter microstructure and myelination. *J. Neurosci.* **33**, 19499–19503 (2013).
86. Hof, P. R. *et al.* Loss and altered spatial distribution of oligodendrocytes in the superior frontal gyrus in schizophrenia. *Biol. Psychiatry* **53**, 1075–1085 (2003).
87. Mitkus, S. N. *et al.* Expression of oligodendrocyte-associated genes in dorsolateral prefrontal cortex of patients with schizophrenia. *Schizophr. Res.* **98**, 129–138 (2008).
88. Åberg, K., Saetre, P., Jareborg, N. & Jazin, E. Human QKI, a potential regulator of mRNA expression of human oligodendrocyte-related genes involved in schizophrenia. *Proc. Natl. Acad. Sci. U. S. A.* **103**, 7482–7487 (2006).
89. Samartzis, L., Dima, D., Fusar-Poli, P. & Kyriakopoulos, M. White Matter Alterations in Early Stages of Schizophrenia: A Systematic Review of Diffusion Tensor Imaging Studies. *J. Neuroimaging* **24**, 101–110 (2014).
90. Denier, C. *et al.* Adult-onset vanishing white matter leukoencephalopathy presenting as psychosis. *Neurology* **68**, 1538–9 (2007).
91. Walterfang, M., Wood, S. J., Velakoulis, D., Copolov, D. & Pantelis, C. Diseases of White Matter and Schizophrenia-Like Psychosis. *Aust. New Zeal. J. Psychiatry* **39**, 746–756 (2005).
92. Dietz, A. G., Goldman, S. A. & Nedergaard, M. Glial cells in schizophrenia: a unified hypothesis. *The Lancet Psychiatry* **7**, 272–281 (2020).
93. McGue, M. & Gottesman, I. I. The genetic epidemiology of schizophrenia and the design of linkage studies. *Eur. Arch. Psychiatry Clin. Neurosci.* **240**, 174–181 (1991).
94. Cannon, T. D., Kaprio, J., Lönqvist, J., Huttunen, M. & Koskenvuo, M. The genetic epidemiology of schizophrenia in a Finnish twin cohort: A population-based modeling study. *Arch. Gen. Psychiatry* **55**, 67–74 (1998).
95. Gunter, C. Schizophrenia: Missing heritability found? *Nat. Rev. Neurosci.* **10**, 543 (2009).
96. Ran, F. A. *et al.* Genome engineering using the CRISPR-Cas9 system. *Nat. Protoc.* **8**, 2281–2308 (2013).
97. Lanciotti, R. S. *et al.* Genetic and serologic properties of Zika virus associated with an epidemic, Yap State, Micronesia, 2007. *Emerg. Infect. Dis.* **14**, 1232–1239 (2008).
98. Ritter, J. M., Martinez, R. B. & Zaki, S. R. Zika virus: Pathology from the pandemic. *Arch. Pathol. Lab. Med.* **141**, 49–59 (2017).
99. Anfasa, F. *et al.* Phenotypic Differences between Asian and African Lineage Zika Viruses in Human Neural Progenitor Cells. *mSphere* **2**, (2017).
100. Rothan, H. A. & Byrareddy, S. N. The epidemiology and pathogenesis of coronavirus disease

- (COVID-19) outbreak. *Journal of Autoimmunity* vol. 109 102433 (2020).
101. Meyerowitz-Katz, G. & Merone, L. A systematic review and meta-analysis of published research data on COVID-19 infection fatality rates. *Int. J. Infect. Dis.* **101**, 138–148 (2020).
 102. Varatharaj, A. *et al.* Neurological and neuropsychiatric complications of COVID-19 in 153 patients: a UK-wide surveillance study. *The Lancet Psychiatry* **7**, 875–882 (2020).
 103. Lechien, J. R. *et al.* Olfactory and gustatory dysfunctions as a clinical presentation of mild-to-moderate forms of the coronavirus disease (COVID-19): a multicenter European study. *Eur. Arch. Oto-Rhino-Laryngology* **277**, 2251–2261 (2020).
 104. Mao, L. *et al.* Neurologic Manifestations of Hospitalized Patients with Coronavirus Disease 2019 in Wuhan, China. *JAMA Neurol.* **77**, 683–690 (2020).
 105. Ellul, M. A. *et al.* Neurological associations of COVID-19. *Lancet Neurol.* **19**, 767–783 (2020).
 106. Moriguchi, T. *et al.* A first case of meningitis/encephalitis associated with SARS-Coronavirus-2. *Int. J. Infect. Dis.* **94**, 55–58 (2020).
 107. Poyiadji, N. *et al.* COVID-19-associated acute hemorrhagic necrotizing encephalopathy: Imaging features. *Radiology* vol. 296 E119–E120 (2020).
 108. Nalbandian, A. *et al.* Post-acute COVID-19 syndrome. *Nature Medicine* vol. 27 601–615 (2021).
 109. Schurink, B. *et al.* Articles Viral presence and immunopathology in patients with lethal COVID-19: a prospective autopsy cohort study. *The Lancet Microbe* **1**, e290–e299 (2020).
 110. Edén, A. *et al.* CSF Biomarkers in Patients With COVID-19 and Neurologic Symptoms: A Case Series. *Neurology* **96**, e294–e300 (2021).
 111. Bryce, B. *et al.* Massive transient damage of the olfactory epithelium associated with infection of sustentacular cells by SARS-CoV-2 in golden Syrian hamsters. *Brain. Behav. Immun.* **89**, 579–586 (2020).
 112. Riel, D. Van, Verdijk, R. & Kuiken, T. The olfactory nerve: A shortcut for influenza and other viral diseases into the central nervous system. *J. Pathol.* **235**, 277–287 (2015).
 113. Oberheim, N. A., Wang, X., Goldman, S. & Nedergaard, M. Astrocytic complexity distinguishes the human brain. *Trends Neurosci.* **29**, 547–53 (2006).
 114. Zhang, Y. *et al.* Purification and Characterization of Progenitor and Mature Human Astrocytes Reveals Transcriptional and Functional Differences with Mouse. *Neuron* **89**, 37–53 (2016).
 115. Diniz, L. P. *et al.* Astrocyte-induced Synaptogenesis Is Mediated by Transforming Growth Factor β Signaling through Modulation of d-Serine Levels in Cerebral Cortex Neurons. *J. Biol. Chem.* **287**, 41432–41445 (2012).
 116. Allen, N. J. & Barres, B. A. Glia - more than just brain glue. *Nature* vol. 457 675–677 (2009).
 117. Bélanger, M., Allaman, I. & Magistretti, P. J. Brain energy metabolism: Focus on Astrocyte-neuron metabolic cooperation. *Cell Metabolism* vol. 14 724–738 (2011).
 118. Macvicar, B. A. & Newman, E. A. Astrocyte regulation of blood flow in the brain. *Cold Spring Harb. Perspect. Biol.* **7**, 1–15 (2015).
 119. Abbott, N. J., Rönnbäck, L. & Hansson, E. Astrocyte–endothelial interactions at the blood–brain barrier. *Nat. Rev. Neurosci.* **7**, 41–53 (2006).
 120. Allen, N. J. & Eroglu, C. Cell Biology of Astrocyte-Synapse Interactions. *Neuron* vol. 96 697–708 (2017).

121. Astick, M. & Vanderhaeghen, P. From Human Pluripotent Stem Cells to Cortical Circuits. in *Current Topics in Developmental Biology* vol. 129 67–98 (Academic Press Inc., 2018).
122. Marchetto, M. C. N. *et al.* A model for neural development and treatment of rett syndrome using human induced pluripotent stem cells. *Cell* **143**, 527–539 (2010).
123. Miller, J. D. *et al.* Human iPSC-based modeling of late-onset disease via progerin-induced aging. *Cell Stem Cell* **13**, 691–705 (2013).
124. Lischka, F. W. *et al.* Neonatal mouse cortical but not isogenic human astrocyte feeder layers enhance the functional maturation of induced pluripotent stem cell-derived neurons in culture. *Glia* **66**, 725–748 (2018).
125. Caiazzo, M. *et al.* Direct Conversion of Fibroblasts into Functional Astrocytes by Defined Transcription Factors. *Stem Cell Reports* **4**, 25–36 (2015).
126. Sloan, S. A. *et al.* Human Astrocyte Maturation Captured in 3D Cerebral Cortical Spheroids Derived from Pluripotent Stem Cells. *Neuron* **95**, 779–790.e6 (2017).
127. Kondo, T. *et al.* Modeling Alexander disease with patient iPSCs reveals cellular and molecular pathology of astrocytes. *Acta Neuropathol. Commun.* **4**, 69 (2016).
128. di Domenico, A. *et al.* Patient-Specific iPSC-Derived Astrocytes Contribute to Non-Cell-Autonomous Neurodegeneration in Parkinson's Disease. *Stem Cell Reports* (2019) doi:10.1016/j.stemcr.2018.12.011.
129. Lundin, A. *et al.* Human iPS-Derived Astroglia from a Stable Neural Precursor State Show Improved Functionality Compared with Conventional Astrocytic Models. *Stem Cell Reports* **10**, 1030–1045 (2018).
130. Bayraktar, O. A. *et al.* Astrocyte layers in the mammalian cerebral cortex revealed by a single-cell in situ transcriptomic map. *Nat. Neurosci.* **23**, 1–10 (2020).
131. Booth, H. D. E. *et al.* RNA sequencing reveals MMP2 and TGFB1 downregulation in LRRK2 G2019S Parkinson's iPSC-derived astrocytes. *Neurobiol. Dis.* **129**, 56–66 (2019).
132. TCW, J. *et al.* An Efficient Platform for Astrocyte Differentiation from Human Induced Pluripotent Stem Cells. *Stem Cell Reports* **9**, 600–614 (2017).
133. Marvin, J. S. *et al.* An optimized fluorescent probe for visualizing glutamate neurotransmission. *Nat. Methods* **10**, 162–170 (2013).
134. Danbolt, N. C. Glutamate uptake. *Progress in Neurobiology* vol. 65 1–105 (2001).
135. Mederos, S., González-Arias, C. & Perea, G. Astrocyte–Neuron Networks: A Multilane Highway of Signaling for Homeostatic Brain Function. *Front. Synaptic Neurosci.* **10**, 45 (2018).
136. Pyka, M., Busse, C., Seidenbecher, C., Gundelfinger, E. D. & Faissner, A. Astrocytes are crucial for survival and maturation of embryonic hippocampal neurons in a neuron-glia cell-insert coculture assay. *Synapse* **65**, 41–53 (2011).
137. Clarke, L. E. & Barres, B. A. Emerging roles of astrocytes in neural circuit development. *Nat. Rev. Neurosci.* **14**, 311–321 (2013).
138. Tang, X. *et al.* Astroglial cells regulate the developmental timeline of human neurons differentiated from induced pluripotent stem cells. *Stem Cell Res.* **11**, 743–757 (2013).
139. Garcia, V. J. *et al.* Huntington's Disease Patient-Derived Astrocytes Display Electrophysiological Impairments and Reduced Neuronal Support. *Front. Neurosci.* **13**, (2019).

140. Hedegaard, A. *et al.* Pro-maturational Effects of Human iPSC-Derived Cortical Astrocytes upon iPSC-Derived Cortical Neurons. *Stem Cell Reports* **15**, 38–51 (2020).
141. Krencik, R. *et al.* Systematic Three-Dimensional Coculture Rapidly Recapitulates Interactions between Human Neurons and Astrocytes. *Stem Cell Reports* **9**, 1745–1753 (2017).
142. Rusakov, D. A. & Lehre, K. P. Perisynaptic asymmetry of glia: New insights into glutamate signalling. *Trends in Neurosciences* vol. 25 492–494 (2002).
143. Marvin, J. S. *et al.* An optimized fluorescent probe for visualizing glutamate neurotransmission. *Nat. Methods* **10**, 162–170 (2013).
144. Frega, M., Tedesco, M., Massobrio, P., Pesce, M. & Martinoia, S. Network dynamics of 3D engineered neuronal cultures: a new experimental model for in-vitro electrophysiology. *Sci. Rep.* **4**, 5489 (2014).
145. Colombo, J. A., Härtig, W., Lipina, S. & Bons, N. Astroglial interlaminar processes in the cerebral cortex of prosimians and Old World monkeys. *Anat. Embryol. (Berl)*. **197**, 369–376 (1998).
146. Yuan, S. H. *et al.* Cell-Surface Marker Signatures for the Isolation of Neural Stem Cells, Glia and Neurons Derived from Human Pluripotent Stem Cells. *PLoS One* **6**, e17540 (2011).
147. Windrem, M. S. *et al.* Neonatal chimerization with human glial progenitor cells can both remyelinate and rescue the otherwise lethally hypomyelinated shiverer mouse. *Cell Stem Cell* **2**, 553–65 (2008).
148. Frega, M. *et al.* Rapid Neuronal Differentiation of Induced Pluripotent Stem Cells for Measuring Network Activity on Micro-electrode Arrays. *J. Vis. Exp.* (2017) doi:10.3791/54900.
149. Bologna, L. L. *et al.* Investigating neuronal activity by SPYCODE multi-channel data analyzer. *Neural Networks* **23**, 685–697 (2010).
150. Van Buggenhout, G. & Fryns, J.-P. Angelman syndrome (AS, MIM 105830). *Eur. J. Hum. Genet.* **17**, 1367–1373 (2009).
151. LaSalle, J. M., Reiter, L. T. & Chamberlain, S. J. Epigenetic regulation of UBE3A and roles in human neurodevelopmental disorders. *Epigenomics* **7**, 1213–1228 (2015).
152. Judson, M. C. *et al.* GABAergic Neuron-Specific Loss of Ube3a Causes Angelman Syndrome-Like EEG Abnormalities and Enhances Seizure Susceptibility. *Neuron* **90**, 56–69 (2016).
153. Chamberlain, S. J. & Lalande, M. Neurodevelopmental disorders involving genomic imprinting at human chromosome 15q11–q13. *Neurobiol. Dis.* **39**, 13–20 (2010).
154. Noor, A. *et al.* 15q11.2 Duplication Encompassing Only the UBE3A Gene Is Associated with Developmental Delay and Neuropsychiatric Phenotypes. *Hum. Mutat.* **36**, 689–693 (2015).
155. Rougeulle, C., Cardoso, C., Fontés, M., Colleaux, L. & Lalande, M. An imprinted antisense RNA overlaps UBE3A and a second maternally expressed transcript. *Nat. Genet.* **19**, 15–16 (1998).
156. Yamasaki, K. *et al.* Neurons but not glial cells show reciprocal imprinting of sense and antisense transcripts of Ube3a. *Hum. Mol. Genet.* **12**, 837–847 (2003).
157. Daneman, R. & Prat, A. The Blood–Brain Barrier. *Cold Spring Harb. Perspect. Biol.* **7**, a020412 (2015).
158. Stanurova, J. *et al.* Angelman syndrome-derived neurons display late onset of paternal UBE3A silencing. *Sci. Rep.* **6**, 30792 (2016).
159. Elgersma, Y. A molecular tightrope. *Nature* **526**, 50–51 (2015).
160. Meng, L., Person, R. E. & Beaudet, A. L. Ube3a-ATS is an atypical RNA polymerase II transcript that represses the paternal expression of Ube3a. doi:10.1093/hmg/dds130.

161. Burette, A. C. *et al.* Subcellular organization of UBE3A in neurons. *J. Comp. Neurol.* **525**, 233–251 (2017).
162. Sun, J. *et al.* UBE3A Regulates Synaptic Plasticity and Learning and Memory by Controlling SK2 Channel Endocytosis. *Cell Rep.* **12**, 449–461 (2015).
163. Egawa, K. *et al.* Decreased tonic inhibition in cerebellar granule cells causes motor dysfunction in a mouse model of angelman syndrome. *Sci. Transl. Med.* **4**, (2012).
164. van Woerden, G. M. *et al.* Rescue of neurological deficits in a mouse model for Angelman syndrome by reduction of α CaMKII inhibitory phosphorylation. *Nat. Neurosci.* **10**, 280–282 (2007).
165. Avagliano Trezza, R. *et al.* Loss of nuclear UBE3A causes electrophysiological and behavioral deficits in mice and is associated with Angelman syndrome. *Nat. Neurosci.* **22**, 1235–1247 (2019).
166. Fink, J. J. *et al.* Disrupted neuronal maturation in Angelman syndrome-derived induced pluripotent stem cells. *Nat. Commun.* **8**, 15038 (2017).
167. Meng, L. *et al.* Towards a therapy for Angelman syndrome by targeting a long non-coding RNA. *Nature* **518**, 409–412 (2015).
168. Wang, T. *et al.* Large-scale targeted sequencing identifies risk genes for neurodevelopmental disorders. *Nat. Commun.* **11**, 4932 (2020).
169. Friedman, J. M. *et al.* Genomic newborn screening: public health policy considerations and recommendations. *BMC Med. Genomics* **10**, 9 (2017).
170. Toonen, L. J. A. *et al.* Intracerebroventricular Administration of a 2'-O-Methyl Phosphorothioate Antisense Oligonucleotide Results in Activation of the Innate Immune System in Mouse Brain. *Nucleic Acid Ther.* **28**, 63–73 (2018).
171. Owen, M. J., Sawa, A. & Mortensen, P. B. Schizophrenia. *Lancet* **6736**, 1–12 (2016).
172. Polderman, T. J. C. *et al.* Meta-analysis of the heritability of human traits based on fifty years of twin studies. *Nat. Genet.* **47**, 702–709 (2015).
173. Ripke, S. *et al.* Biological insights from 108 schizophrenia-associated genetic loci. *Nature* **511**, 421–427 (2014).
174. Sullivan, P. F., Daly, M. J. & O'Donovan, M. Genetic architectures of psychiatric disorders: the emerging picture and its implications. *Nat. Rev. Genet.* **13**, 537–51 (2012).
175. Rees, E. *et al.* Analysis of copy number variations at 15 schizophrenia-associated loci. *Br. J. Psychiatry* **204**, 108–14 (2014).
176. Marshall, C. *et al.* A contribution of novel CNVs to schizophrenia from a genome-wide study of 41,321 subjects. *bioRxiv* (2016) doi:10.1101/040493.
177. Szatkiewicz, J. P. *et al.* Copy number variation in schizophrenia in Sweden. *Mol. Psychiatry* **19**, 762–773 (2014).
178. Purcell, S. M. *et al.* A polygenic burden of rare disruptive mutations in schizophrenia. *Nature* **506**, 185–190 (2014).
179. Takata, A., Ionita-Laza, I., Gogos, J. A., Xu, B. & Karayiorgou, M. De Novo Synonymous Mutations in Regulatory Elements Contribute to the Genetic Etiology of Autism and Schizophrenia. *Neuron* **89**, 940–947 (2016).
180. Xu, B. *et al.* De novo gene mutations highlight patterns of genetic and neural complexity in schizophrenia. *Nat. Genet.* **44**, 1365–9 (2012).

181. Fromer, M. *et al.* De novo mutations in schizophrenia implicate synaptic networks. *Nature* **506**, 179–184 (2014).
182. Sekar, A. *et al.* Schizophrenia risk from complex variation of complement component 4. *Nature* **530**, 177–183 (2016).
183. Nave, K.-A. & Ehrenreich, H. Myelination and oligodendrocyte functions in psychiatric diseases. *JAMA psychiatry* **71**, (2014).
184. Goudriaan, A. *et al.* Specific glial functions contribute to Schizophrenia susceptibility. *Schizophr. Bull.* **40**, (2014).
185. Fields, R. D. White matter in learning, cognition and psychiatric disorders. *Trends in Neurosciences* vol. 31 361–370 (2008).
186. Paus, T., Keshavan, M. & Giedd, J. N. Why do many psychiatric disorders emerge during adolescence? *Nat. Rev. Neurosci.* **9**, 947–57 (2008).
187. Terwisscha Van Scheltinga, A. F. *et al.* Genetic schizophrenia risk variants jointly modulate total brain and white matter volume. *Biol. Psychiatry* **73**, 525–531 (2013).
188. van den Heuvel, M. P. *et al.* Abnormal rich club organization and functional brain dynamics in schizophrenia. *JAMA psychiatry* **70**, 783–92 (2013).
189. Voineskos, A. N. *et al.* Diffusion tensor tractography findings in schizophrenia across the adult lifespan. *Brain* **133**, 1494–504 (2010).
190. Chavarria-Siles, I. *et al.* Myelination-related genes are associated with decreased white matter integrity in schizophrenia. *Eur. J. Hum. Genet.* **24**, 1–6 (2015).
191. Duncan, L. E. *et al.* Pathway analyses implicate glial cells in schizophrenia. *PLoS One* **9**, e89441 (2014).
192. Chang, Y. S. *et al.* Reciprocal white matter alterations due to 16p11.2 chromosomal deletions versus duplications. *Hum. Brain Mapp.* **37**, 2833–2848 (2016).
193. Owen, J. P. *et al.* Aberrant white matter microstructure in children with 16p11.2 deletions. *J. Neurosci.* **34**, 6214–23 (2014).
194. Exome Aggregation Consortium *et al.* Analysis of protein-coding genetic variation in 60,706 humans. *bioRxiv* (2015) doi:10.1101/030338.
195. Exome Variant Server, NHLBI GO Exome Sequencing Project (ESP), Seattle, WA. <http://evs.gs.washington.edu/EVS/> (2013).
196. Abecasis, G. R. *et al.* A map of human genome variation from population-scale sequencing. *Nature* **467**, 1061–73 (2010).
197. Consortium, T. G. of the N. Whole-genome sequence variation, population structure and demographic history of the Dutch population. *Nat. Genet.* **46**, 818–825 (2014).
198. Hofman, A. *et al.* The rotterdam study: 2014 objectives and design update. *Eur. J. Epidemiol.* **28**, 889–926 (2013).
199. Dekker, J., Peen, J., Gardien, R., de Jonghe, F. & Wijdenes, W. Urbanisation and psychiatric admission rates in The Netherlands. *Int. J. Soc. Psychiatry* **43**, 235–46 (1997).
200. Wierdsma, A. I., Van Marle, P. D. & Mulder, C. L. Aantallen en patronen van inbewaringstellingen en rechterlijke machtigingen in Maastricht, Groningen en Rotterdam: Bijdrage van stedelijke problematiek aan regionale verschillen in Bopz-maatregelen. *Tijdschr. Psychiatr.* **52**, 143–153 (2010).

201. Escamilla, M. *et al.* A schizophrenia gene locus on chromosome 17q21 in a new set of families of Mexican and central american ancestry: evidence from the NIMH Genetics of schizophrenia in latino populations study. *Am. J. Psychiatry* **166**, 442–9 (2009).
202. Vieland, V. J., Walters, K. A., Azaro, M., Brzustowicz, L. M. & Lehner, T. The value of regenotyping older linkage data sets with denser marker panels. *Hum. Hered.* **78**, 9–16 (2014).
203. Timpl, R. *et al.* Structure and function of laminin LG modules. *Matrix Biology* vol. 19 309–317 (2000).
204. Xu, B. *et al.* Exome sequencing supports a de novo mutational paradigm for schizophrenia. *Nat. Genet.* **43**, 1–6 (2011).
205. Rujescu, D. *et al.* Disruption of the neurexin 1 gene is associated with schizophrenia. *Hum. Mol. Genet.* **18**, 988–96 (2009).
206. Kirov, G. *et al.* Comparative genome hybridization suggests a role for NRXN1 and APBA2 in schizophrenia. *Hum. Mol. Genet.* **17**, 458–465 (2008).
207. Kelley, L. A. & Sternberg, M. J. E. Protein structure prediction on the Web: a case study using the Phyre server. *Nat. Protoc.* **4**, 363–71 (2009).
208. Zhang, Y. I-TASSER server for protein 3D structure prediction. *BMC Bioinformatics* **9**, 40 (2008).
209. Miller, M. T. *et al.* The crystal structure of the α -neurexin-1 extracellular region reveals a hinge point for mediating synaptic adhesion and function. *Structure* **19**, 767–78 (2011).
210. Chen, F., Venugopal, V., Murray, B. & Rudenko, G. The structure of neurexin 1 α reveals features promoting a role as synaptic organizer. *Structure* **19**, 779–89 (2011).
211. Holm, L. & Rosenström, P. Dali server: conservation mapping in 3D. *Nucleic Acids Res.* **38**, W545-9 (2010).
212. Burg, M. A., Nishiyama, A. & Stallcup, W. B. A central segment of the NG2 proteoglycan is critical for the ability of glioma cells to bind and migrate toward type VI collagen. *Exp. Cell Res.* **235**, 254–64 (1997).
213. Tillet, E., Gentil, B., Garrone, R. & Stallcup, W. B. NG2 proteoglycan mediates beta1 integrin-independent cell adhesion and spreading on collagen VI. *J. Cell. Biochem.* **86**, 726–36 (2002).
214. Stallcup, W. B. The NG2 proteoglycan: past insights and future prospects. *J. Neurocytol.* **31**, 423–35 (2003).
215. Nishiyama, A., Lin, X. & Stallcup, W. B. Generation of Truncated Forms of the NG2 Proteoglycan by Cell Surface Proteolysis. **6**, 1819–1832 (1995).
216. Sakry, D. *et al.* Oligodendrocyte Precursor Cells Modulate the Neuronal Network by Activity-Dependent Ectodomain Cleavage of Glial NG2. *PLoS Biol.* **12**, e1001993 (2014).
217. Stallcup, W. B. & Dahlin-Huppe, K. Chondroitin sulfate and cytoplasmic domain-dependent membrane targeting of the NG2 proteoglycan promotes retraction fiber formation and cell polarization. *J. Cell Sci.* **114**, 2315–2325 (2001).
218. Obacz, J. *et al.* Endoplasmic reticulum proteostasis in glioblastoma - From molecular mechanisms to therapeutic perspectives. *Science Signaling* vol. 10 (2017).
219. Clayton, B. L. L. & Popko, B. Endoplasmic reticulum stress and the unfolded protein response in disorders of myelinating glia. *Brain Res.* **1648**, 594–602 (2016).
220. Back, S. A., Khan, R., Gan, X., Rosenberg, P. A. & Volpe, J. J. A new Alamar Blue viability assay to rapidly quantify oligodendrocyte death. *J. Neurosci. Methods* **91**, 47–54 (1999).

221. Bergles, D. E. & Richardson, W. D. Oligodendrocyte development and plasticity. *Cold Spring Harb. Perspect. Biol.* **8**, (2016).
222. Najm, F. J. *et al.* Transcription factor-mediated reprogramming of fibroblasts to expandable, myelinogenic oligodendrocyte progenitor cells. *Nat. Biotechnol.* **31**, 426–433 (2013).
223. White, T. *et al.* Spatial characteristics of white matter abnormalities in schizophrenia. *Schizophr. Bull.* **39**, 1077–86 (2013).
224. Birey, F. *et al.* Genetic and Stress-Induced Loss of NG2 Glia Triggers Emergence of Depressive-like Behaviors through Reduced Secretion of FGF2. *Neuron* **88**, 941–956 (2015).
225. Lee, S. H. *et al.* Genetic relationship between five psychiatric disorders estimated from genome-wide SNPs. *Nat. Genet.* **45**, 984–94 (2013).
226. O'Donovan, M. C. & Owen, M. J. The implications of the shared genetics of psychiatric disorders. *Nat. Med.* **22**, 1214–1219 (2016).
227. Pluschke, G. *et al.* Molecular cloning of a human melanoma-associated chondroitin sulfate proteoglycan. *Proc. Natl. Acad. Sci. U. S. A.* **93**, 9710–5 (1996).
228. Riccardo, F. *et al.* CSPG4-specific immunity and survival prolongation in dogs with oral malignant melanoma immunized with human CSPG4 DNA. *Clin. Cancer Res.* **20**, 3753–62 (2014).
229. Geldres, C. *et al.* T lymphocytes redirected against the chondroitin sulfate proteoglycan-4 control the growth of multiple solid tumors both in vitro and in vivo. *Clin. Cancer Res.* **20**, 962–71 (2014).
230. Adzhubei, I. A. *et al.* A method and server for predicting damaging missense mutations. *Nat. Methods* **7**, 248–9 (2010).
231. Lee, M. K. *et al.* Human alpha-synuclein-harboring familial Parkinson's disease-linked Ala-53 --> Thr mutation causes neurodegenerative disease with alpha-synuclein aggregation in transgenic mice. *Proc. Natl. Acad. Sci. U. S. A.* **99**, 8968–73 (2002).
232. Wen, Z. *et al.* Synaptic dysregulation in a human iPS cell model of mental disorders. *Nature* **515**, 414–418 (2014).
233. Bigdeli, T. B. *et al.* Genome-wide association study reveals greater polygenic loading for schizophrenia in cases with a family history of illness. *Am. J. Med. Genet. Part B Neuropsychiatr. Genet.* **171**, 276–289 (2016).
234. Lin, S. & Bergles, D. E. Synaptic signaling between GABAergic interneurons and oligodendrocyte precursor cells in the hippocampus. *Nat. Neurosci.* **7**, 24–32 (2004).
235. Orduz, D. *et al.* Interneurons and oligodendrocyte progenitors form a structured synaptic network in the developing neocortex. *Elife* **4**, (2015).
236. Zonouzi, M. *et al.* GABAergic regulation of cerebellar NG2 cell development is altered in perinatal white matter injury. *Nat. Neurosci.* **18**, 674–82 (2015).
237. Balia, M. *et al.* Postnatal down-regulation of the GABAA receptor $\gamma 2$ subunit in neocortical NG2 cells accompanies synaptic-to-extrasynaptic switch in the GABAergic transmission mode. *Cereb. Cortex* **25**, 1114–23 (2015).
238. Maldonado, P. P., Vélez-Fort, M., Levavasseur, F. & Angulo, M. C. Oligodendrocyte precursor cells are accurate sensors of local K⁺ in mature gray matter. *J. Neurosci.* **33**, 2432–42 (2013).
239. Lin, W. & Popko, B. Endoplasmic reticulum stress in disorders of myelinating cells. *Nat. Neurosci.* **12**, 379–85 (2009).

240. Zalesky, A. *et al.* Disrupted axonal fiber connectivity in schizophrenia. *Biol. Psychiatry* **69**, 80–89 (2011).
241. Davis, K. L. *et al.* White matter changes in schizophrenia: evidence for myelin-related dysfunction. *Arch. Gen. Psychiatry* **60**, 443–456 (2003).
242. Andreasen, N. C. *et al.* Progressive brain change in schizophrenia: A prospective longitudinal study of first-episode schizophrenia. *Biol. Psychiatry* **70**, 672–679 (2011).
243. Gonzalez-Burgos, G., Cho, R. Y. & Lewis, D. A. Alterations in Cortical Network Oscillations and Parvalbumin Neurons in Schizophrenia. *Biol. Psychiatry* **77**, 1031–1040 (2015).
244. Marín, O. Developmental timing and critical windows for the treatment of psychiatric disorders. *Nature Medicine* vol. 22 1229–1238 (2016).
245. Stedehouder, J. & Kushner, S. A. Myelination of parvalbumin interneurons: A parsimonious locus of pathophysiological convergence in schizophrenia. *Mol. Psychiatry* **22**, 4–12 (2017).
246. First, M., Gibbon, M. & Spitzer, R. Structured Clinical Interview for DSM-IV Axis II Personality Disorders (SCID-II). *Am. Psychiatr. Press. Inc.* (1997).
247. Hoffmann, K. & Lindner, T. H. easyLINKAGE-Plus - Automated linkage analyses using large-scale SNP data. *Bioinformatics* **21**, 3565–3567 (2005).
248. Loohuis, L. M. O. *et al.* Genome-wide burden of deleterious coding variants increased in schizophrenia. *Nat. Commun.* **6**, 7501 (2015).
249. Warlich, E. *et al.* Lentiviral Vector Design and Imaging Approaches to Visualize the Early Stages of Cellular Reprogramming. *Mol. Ther.* **19**, 782–789 (2011).
250. Monaco, M. C. G. *et al.* Progenitor-derived Oligodendrocyte Culture System from Human Fetal Brain. *J. Vis. Exp.* (2012) doi:10.3791/4274.
251. Huang, G. N. *et al.* STIM1 carboxyl-terminus activates native SOC, I(crac) and TRPC1 channels. *Nat. Cell Biol.* **8**, 1003–1010 (2006).
252. Stoppini, L., Buchs, P. A. & Muller, D. A simple method for organotypic cultures of nervous tissue. *J. Neurosci. Methods* **37**, 173–82 (1991).
253. Koppelmans, V. *et al.* Global and focal white matter integrity in breast cancer survivors 20 years after adjuvant chemotherapy. *Hum. Brain Mapp.* **35**, 889–99 (2014).
254. Ikram, M. A. *et al.* The Rotterdam Scan Study: design and update up to 2012. *Eur. J. Epidemiol.* **26**, 811–24 (2011).
255. Smith, S. M. *et al.* Advances in functional and structural MR image analysis and implementation as FSL. in *NeuroImage* vol. 23 (2004).
256. Smith, S. M. Fast robust automated brain extraction. *Hum. Brain Mapp.* **17**, 143–155 (2002).
257. Andersson, J. L. R., Jenkinson, M. & Smith, S. *Non-linear registration aka Spatial normalisation FMRIB Technical Report TR07JA2. In Practice* (2007).
258. Rueckert, D. *et al.* Nonrigid registration using free-form deformations: application to breast MR images. *IEEE Trans. Med. Imaging* **18**, 712–721 (1999).
259. Mori, S. *et al.* Stereotaxic white matter atlas based on diffusion tensor imaging in an ICBM template. *Neuroimage* **40**, 570–582 (2008).
260. White, T., Schmidt, M. & Karatekin, C. White matter ‘potholes’ in early-onset schizophrenia: a new approach to evaluate white matter microstructure using diffusion tensor imaging. *Psychiatry Res.*

- 174, 110–115 (2009).
261. Smith, S. M. *et al.* Tract-based spatial statistics: Voxelwise analysis of multi-subject diffusion data. *Neuroimage* **31**, 1487–1505 (2006).
262. Varatharaj, A. *et al.* Neurological and neuropsychiatric complications of COVID-19 in 153 patients: a UK-wide surveillance study. *The Lancet Psychiatry* **7**, 875–882 (2020).
263. Harapan, B. N. & Yoo, H. J. Neurological symptoms, manifestations, and complications associated with severe acute respiratory syndrome coronavirus 2 (SARS-CoV-2) and coronavirus disease 19 (COVID-19). *J. Neurol.* **2**, (2021).
264. Guadarrama-Ortiz, P. *et al.* Neurological Aspects of SARS-CoV-2 Infection: Mechanisms and Manifestations. *Front. Neurol.* **11**, 1–14 (2020).
265. Solomon, I. H. *et al.* Neuropathological Features of Covid-19. *N. Engl. J. Med.* (2020) doi:10.1056/nejmc2019373.
266. Pennisi, M. *et al.* Sars-cov-2 and the nervous system: From clinical features to molecular mechanisms. *Int. J. Mol. Sci.* **21**, 1–21 (2020).
267. Zou, L. *et al.* SARS-CoV-2 Viral Load in Upper Respiratory Specimens of Infected Patients. *N. Engl. J. Med.* **382**, 1175–1177 (2020).
268. Sia, S. F. *et al.* Pathogenesis and transmission of SARS-CoV-2 in golden hamsters. *Nature* **583**, 834–838 (2020).
269. Meinhardt, J. *et al.* Olfactory transmucosal SARS-CoV-2 invasion as a port of central nervous system entry in individuals with COVID-19. *Nat. Neurosci.* **24**, 168–175 (2021).
270. Matschke, J. *et al.* Neuropathology of patients with COVID-19 in Germany: a post-mortem case series. *Lancet Neurol.* **19**, 919–929 (2020).
271. Schurink, B. *et al.* Viral presence and immunopathology in patients with lethal COVID-19: a prospective autopsy cohort study. *The Lancet Microbe* **1**, e290–e299 (2020).
272. Neumann, B. *et al.* Cerebrospinal fluid findings in COVID-19 patients with neurological symptoms. *J. Neurol. Sci.* **418**, (2020).
273. Destras, G. *et al.* Systematic SARS-CoV-2 screening in cerebrospinal fluid during the COVID-19 pandemic. *The Lancet Microbe* **1**, e149 (2020).
274. Dobrindt, K. *et al.* Common genetic variation in humans impacts in vitro susceptibility to SARS-CoV-2 infection. *Stem Cell Reports* **16**, 1–14 (2021).
275. Pellegrini, L. *et al.* SARS-CoV-2 Infects the Brain Choroid Plexus and Disrupts the Blood-CSF Barrier in Human Brain Organoids. *Cell Stem Cell* **27**, 951-961.e5 (2020).
276. Zhang, B. Z. *et al.* SARS-CoV-2 infects human neural progenitor cells and brain organoids. *Cell Res.* **30**, 928–931 (2020).
277. Bullen, C. K. *et al.* Infectability of human BrainSphere neurons suggests neurotropism of SARS-CoV-2. *ALTEX* **37**, 665–671 (2020).
278. Wang, C. *et al.* ApoE-Isoform-Dependent SARS-CoV-2 Neurotropism and Cellular Response. *Cell Stem Cell* **28**, 331-342.e5 (2021).
279. Song, E. *et al.* Neuroinvasion of SARS-CoV-2 in human and mouse brain. *J. Exp. Med.* **218**, (2021).
280. Ramani, A. *et al.* SARS -CoV-2 targets neurons of 3D human brain organoids . *EMBO J.* **39**, 1–14 (2020).

281. Jacob, F. *et al.* Human Pluripotent Stem Cell-Derived Neural Cells and Brain Organoids Reveal SARS-CoV-2 Neurotropism Predominates in Choroid Plexus Epithelium. *Cell Stem Cell* **27**, 937-950.e9 (2020).
282. Gunhanlar, N. *et al.* A simplified protocol for differentiation of electrophysiologically mature neuronal networks from human induced pluripotent stem cells. *Mol. Psychiatry* (2017) doi:10.1038/mp.2017.56.
283. Schrauwen, E. J. A. *et al.* The Multibasic Cleavage Site in H5N1 Virus Is Critical for Systemic Spread along the Olfactory and Hematogenous Routes in Ferrets. *J. Virol.* **86**, 3975–3984 (2012).
284. Shinya, K. *et al.* Subclinical Brain Injury Caused by H5N1 Influenza Virus Infection. *J. Virol.* **85**, 5202–5207 (2011).
285. Bodewes, R. *et al.* Pathogenesis of influenza A/H5N1 virus infection in ferrets differs between intranasal and intratracheal routes of inoculation. *Am. J. Pathol.* **179**, 30–36 (2011).
286. Park, C. H. *et al.* The invasion routes of neurovirulent A/Hong Kong/483/97 (H5N1) influenza virus into the central nervous system after respiratory infection in mice. *Arch. Virol.* **147**, 1425–1436 (2002).
287. Jang, H. *et al.* Highly pathogenic H5N1 influenza virus can enter the central nervous system and induce neuroinflammation and neurodegeneration. *Proc. Natl. Acad. Sci. U. S. A.* **106**, 14063–14068 (2009).
288. Shinya, K. *et al.* Systemic Dissemination of H5N1 Influenza A Viruses in Ferrets and Hamsters after Direct Intragastric Inoculation. *J. Virol.* **85**, 4673–4678 (2011).
289. Siegers, J. Y. *et al.* Viral Factors Important for Efficient Replication of Influenza A Viruses in Cells of the Central Nervous System. *J. Virol.* **93**, 1–12 (2019).
290. Ng, Y. P. *et al.* Avian influenza H5N1 virus induces cytopathy and proinflammatory cytokine responses in human astrocytic and neuronal cell lines. *Neuroscience* (2010) doi:10.1016/j.neuroscience.2010.04.013.
291. Pringproa, K. *et al.* Tropism and induction of cytokines in human embryonic-stem cells-derived neural progenitors upon inoculation with highly-pathogenic avian H5N1 influenza virus. *PLoS One* **10**, 1–14 (2015).
292. Lin, X. *et al.* Insights into human astrocyte response to H5N1 infection by microarray analysis. *Viruses* **7**, 2618–2640 (2015).
293. Van Riel, D. *et al.* Evidence for influenza virus CNS invasion along the olfactory route in an immunocompromised infant. *J. Infect. Dis.* **210**, 419–423 (2014).
294. Shinya, K. *et al.* Avian influenza virus intranasally inoculated infects the central nervous system of mice through the general visceral afferent nerve. *Arch. Virol.* **145**, 187–195 (2000).
295. Casez, O. *et al.* Teaching Neurolmages: SARS-CoV-2-Related Encephalitis: MRI Pattern of Olfactory Tract Involvement. *Neurology* **96**, e645–e646 (2021).
296. Vandervorst, F. *et al.* Encephalitis associated with the SARS-CoV-2 virus: A case report. *Interdiscip. Neurosurg. Adv. Tech. Case Manag.* **22**, 0–2 (2020).
297. Yang, L. *et al.* A Human Pluripotent Stem Cell-based Platform to Study SARS-CoV-2 Tropism and Model Virus Infection in Human Cells and Organoids. *Cell Stem Cell* **27**, 125-136.e7 (2020).
298. Jacob, F. *et al.* Human Pluripotent Stem Cell-Derived Neural Cells and Brain Organoids Reveal

- SARS-CoV-2 Neurotropism Predominates in Choroid Plexus Epithelium. *Cell Stem Cell* (2020) doi:10.1016/j.stem.2020.09.016.
299. Vanderheiden, A. *et al.* Type I and Type III Interferons Restrict SARS-CoV-2 Infection of Human Airway Epithelial Cultures. *J. Virol.* **94**, 1–16 (2020).
300. Blanco-Melo, D. *et al.* Imbalanced Host Response to SARS-CoV-2 Drives Development of COVID-19. *Cell* **181**, 1036-1045.e9 (2020).
301. Del Valle, D. M. *et al.* An inflammatory cytokine signature predicts COVID-19 severity and survival. *Nat. Med.* **26**, 1636–1643 (2020).
302. van Riel, D. *et al.* Temporal kinetics of RNAemia and associated systemic cytokines in hospitalized COVID-19 patients. *bioRxiv* (2020) doi:10.1101/2020.12.17.423376.
303. Chen, L. *et al.* Scoring cytokine storm by the levels of MCP-3 and IL-8 accurately distinguished COVID-19 patients with high mortality. *Signal Transduct. Target. Ther.* **5**, 8–10 (2020).
304. Benameur, K. *et al.* Encephalopathy and encephalitis associated with cerebrospinal fluid cytokine alterations and coronavirus disease, atlanta, georgia, usa, 2020. *Emerg. Infect. Dis.* **26**, 2016–2021 (2020).
305. Park, C. H. *et al.* Persistence of viral RNA segments in the central nervous system of mice after recovery from acute influenza A virus infection. *Vet. Microbiol.* **97**, 259–268 (2003).
306. Jang, H. *et al.* Inflammatory effects of highly pathogenic H5N1 influenza virus infection in the CNS of mice. *J. Neurosci.* **32**, 1545–1559 (2012).
307. Kroeze, E. V., Bauer, L., Caliendo, V. & Riel, D. van. In Vivo Models to Study the Pathogenesis of Extra-Respiratory Complications of Influenza A Virus Infection. *Viruses* 2021, Vol. 13, Page 848 **13**, 848 (2021).
308. Mak, G. C. K. *et al.* Influenza A(H5N1) Virus Infection in a Child with Encephalitis Complicated by Obstructive Hydrocephalus. *Clin. Infect. Dis.* **66**, 136–139 (2018).
309. Gambotto, A., Barratt-Boyes, S. M., de Jong, M. D., Neumann, G. & Kawaoka, Y. Human infection with highly pathogenic H5N1 influenza virus. *Lancet* **371**, 1464–1475 (2008).
310. Lamers, M. M. *et al.* SARS-CoV-2 productively infects human gut enterocytes. *Science* (80-.). **3**, 50–54 (2020).
311. Lamers, M. M. *et al.* Human airway cells prevent SARS-CoV-2 multibasic cleavage site cell culture adaptation 1 2. *bioRxiv* (2021).
312. Rimmelzwaan, G. F., Baars, M., Claas, E. C. J. & Osterhaus, A. D. M. E. Comparison of RNA hybridization, hemagglutination assay, titration of infectious virus and immunofluorescence as methods for monitoring influenza virus replication in vitro. *J. Virol. Methods* (1998) doi:10.1016/S0166-0934(98)00071-8.
313. Trujillo, C. A. *et al.* Complex Oscillatory Waves Emerging from Cortical Organoids Model Early Human Brain Network Development. *Cell Stem Cell* **0**,.
314. Negoro, T., Okura, H. & Matsuyama, A. Induced Pluripotent Stem Cells: Global Research Trends. *Biores. Open Access* **6**, 63–73 (2017).
315. Pasteuning-Vuhman, S., de Jongh, R., Timmers, A. & Pasterkamp, R. J. Towards Advanced iPSC-based Drug Development for Neurodegenerative Disease. *Trends Mol. Med.* **27**, 263–279 (2020).
316. Schweitzer, J. S. *et al.* Personalized iPSC-Derived Dopamine Progenitor Cells for Parkinson's

- Disease. *N. Engl. J. Med.* **382**, 1926–1932 (2020).
317. Bhutani, K. *et al.* Whole-genome mutational burden analysis of three pluripotency induction methods. *Nat. Commun.* **7**, 10536 (2016).
318. D'Antonio, M. *et al.* Insights into the Mutational Burden of Human Induced Pluripotent Stem Cells from an Integrative Multi-Omics Approach. *Cell Rep.* **24**, 883–894 (2018).
319. Halliwell, J., Barbaric, I. & Andrews, P. W. Acquired genetic changes in human pluripotent stem cells: origins and consequences. *Nat. Rev. Mol. Cell Biol.* **21**, 715–728 (2020).
320. Ohi, Y. *et al.* Incomplete DNA methylation underlies a transcriptional memory of somatic cells in human iPS cells. *Nat. Cell Biol.* **13**, 541–549 (2011).
321. Marchetto, M. C. N. *et al.* Transcriptional signature and memory retention of human-induced pluripotent stem cells. *PLoS One* **4**, e7076 (2009).
322. Kim, K. *et al.* Epigenetic memory in induced pluripotent stem cells. *Nature* **467**, 285–290 (2010).
323. Rouhani, F. *et al.* Genetic Background Drives Transcriptional Variation in Human Induced Pluripotent Stem Cells. *PLoS Genet.* **10**, e1004432 (2014).
324. Panopoulos, A. D. *et al.* Aberrant DNA Methylation in Human iPSCs Associates with MYC-Binding Motifs in a Clone-Specific Manner Independent of Genetics. *Cell Stem Cell* **20**, 505–517.e6 (2017).
325. Hendriks, W. T., Warren, C. R. & Cowan, C. A. Genome Editing in Human Pluripotent Stem Cells: Approaches, Pitfalls, and Solutions. *Cell Stem Cell* **18**, 53–65 (2016).
326. Dominguez, A. A., Lim, W. A. & Qi, L. S. Beyond editing: repurposing CRISPR–Cas9 for precision genome regulation and interrogation. *Nat. Rev. Mol. Cell Biol.* **17**, 5–15 (2016).
327. Schrode, N. *et al.* Synergistic effects of common schizophrenia risk variants. *Nat. Genet.* **51**, 1475–1485 (2019).
328. Madison, J. M. *et al.* Characterization of bipolar disorder patient-specific induced pluripotent stem cells from a family reveals neurodevelopmental and mRNA expression abnormalities. *Mol. Psychiatry* **20**, 703–717 (2015).
329. Stockholm, D. *et al.* The Origin of Phenotypic Heterogeneity in a Clonal Cell Population In Vitro. *PLoS One* **2**, e394 (2007).
330. Prakash Bangalore, M., Adhikarla, S., Mukherjee, O. & Panicker, M. M. Genotoxic Effects of Culture Media on Human Pluripotent Stem Cells. *Sci. Rep.* **7**, 42222 (2017).
331. Chen, Y.-H. & Pruett-Miller, S. M. Improving single-cell cloning workflow for gene editing in human pluripotent stem cells. *Stem Cell Res.* **31**, 186–192 (2018).
332. Ehrlich, M. *et al.* Rapid and efficient generation of oligodendrocytes from human induced pluripotent stem cells using transcription factors. *Proc. Natl. Acad. Sci.* 201614412 (2017) doi:10.1073/PNAS.1614412114.
333. Yoon, S.-J. *et al.* Reliability of human cortical organoid generation. *Nat. Methods* **16**, 75–78 (2019).
334. Giandomenico, S. L. *et al.* Cerebral organoids at the air–liquid interface generate diverse nerve tracts with functional output. *Nat. Neurosci.* **22**, 669–679 (2019).
335. Lancaster, M. a *et al.* Cerebral organoids model human brain development and microcephaly. *Nature* **501**, 373–379 (2013).
336. Zafeiriou, M. P. *et al.* Developmental GABA polarity switch and neuronal plasticity in Bioengineered Neuronal Organoids. *Nat. Commun.* **11**, (2020).

337. Qian, X. *et al.* Generation of human brain region-specific organoids using a miniaturized spinning bioreactor. *Nat. Protoc.* **13**, 565–580 (2018).
338. Miura, Y. *et al.* Generation of human striatal organoids and cortico-striatal assembloids from human pluripotent stem cells. *Nat. Biotechnol.* **38**, 1421–1430 (2020).
339. Xiang, Y. *et al.* hESC-Derived Thalamic Organoids Form Reciprocal Projections When Fused with Cortical Organoids. *Cell Stem Cell* **24**, 487-497.e7 (2019).
340. Shi, Y. *et al.* Vascularized human cortical organoids (vOrganoids) model cortical development in vivo. *PLOS Biol.* **18**, e3000705 (2020).
341. Song, L. *et al.* Functionalization of Brain Region-specific Spheroids with Isogenic Microglia-like Cells. *Sci. Rep.* **9**, 11055 (2019).
342. Pellegrini, L. *et al.* Human CNS barrier-forming organoids with cerebrospinal fluid production. *Science (80-.).* **369**, eaaz5626 (2020).
343. Quadrato, G. *et al.* Cell diversity and network dynamics in photosensitive human brain organoids. *Nature* **545**, 48–53 (2017).
344. Lancaster, M. A. *et al.* Guided self-organization and cortical plate formation in human brain organoids. *Nat. Biotechnol.* **35**, 659–666 (2017).
345. Volpato, V. & Webber, C. Addressing variability in iPSC-derived models of human disease: guidelines to promote reproducibility. *Dis. Model. Mech.* **13**, (2020).
346. Hoffman, G. E., Schrodde, N., Flaherty, E. & Brennand, K. J. New considerations for hiPSC-based models of neuropsychiatric disorders HHS Public Access. *Mol Psychiatry* **24**, 49–66 (2019).
347. DeBoever, C. *et al.* Large-Scale Profiling Reveals the Influence of Genetic Variation on Gene Expression in Human Induced Pluripotent Stem Cells. *Cell Stem Cell* **20**, 533-546.e7 (2017).
348. Cuomo, A. S. E. *et al.* Single-cell RNA-sequencing of differentiating iPS cells reveals dynamic genetic effects on gene expression. *Nat. Commun.* **11**, 810 (2020).
349. Bonder, M. J. *et al.* Identification of rare and common regulatory variants in pluripotent cells using population-scale transcriptomics. *Nat. Genet.* **53**, 313–321 (2021).
350. Mitchell, J. *et al.* Mapping genetic effects on cellular phenotypes with “cell villages”. *bioRxiv* 2020.06.29.174383 (2020) doi:10.1101/2020.06.29.174383.
351. Sanjana, N. E., Shalem, O. & Zhang, F. Improved vectors and genome-wide libraries for CRISPR screening. *Nature Methods* vol. 11 783–784 (2014).
352. Horlbeck, M. A. *et al.* Compact and highly active next-generation libraries for CRISPR-mediated gene repression and activation. *Elife* **5**, (2016).
353. Potting, C. *et al.* Genome-wide CRISPR screen for PARKIN regulators reveals transcriptional repression as a determinant of mitophagy. *Proc. Natl. Acad. Sci.* **115**, E180–E189 (2018).
354. Tian, R. *et al.* CRISPR Interference-Based Platform for Multimodal Genetic Screens in Human iPSC-Derived Neurons. *Neuron* **104**, 239-255.e12 (2019).
355. Gordon, A. *et al.* Long-term maturation of human cortical organoids matches key early postnatal transitions. *Nat. Neurosci.* **24**, 331–342 (2021).
356. Kanton, S. *et al.* Organoid single-cell genomic atlas uncovers human-specific features of brain development. *Nature* **574**, 418–422 (2019).
357. Fiddes, I. T. *et al.* Human-Specific NOTCH2NL Genes Affect Notch Signaling and Cortical

- Neurogenesis. *Cell* **173**, 1356-1369.e22 (2018).
358. Trujillo, C. A. *et al.* Reintroduction of the archaic variant of NOVA1 in cortical organoids alters neurodevelopment. *Science* (80-.). **371**, eaax2537 (2021).
359. Mayer, S. *et al.* Multimodal Single-Cell Analysis Reveals Physiological Maturation in the Developing Human Neocortex. *Neuron* **102**, 143-158.e7 (2019).
360. Miccoli, B. *et al.* High-Density Electrical Recording and Impedance Imaging With a Multi-Modal CMOS Multi-Electrode Array Chip. *Front. Neurosci.* **13**, 641 (2019).
361. Weinreb, C., Rodriguez-Fraticelli, A., Camargo, F. D. & Klein, A. M. Lineage tracing on transcriptional landscapes links state to fate during differentiation. *Science* (80-.). **367**, eaaw3381 (2020).
362. Durens, M. *et al.* High-throughput screening of human induced pluripotent stem cell-derived brain organoids. *J. Neurosci. Methods* **335**, 108627 (2020).
363. Qian, X. *et al.* Probabilistic cell typing enables fine mapping of closely related cell types in situ. *Nat. Methods* **17**, 101–106 (2020).
364. Wu, Q. *et al.* Organ-on-a-chip: recent breakthroughs and future prospects. *Biomed. Eng. Online* **19**, 9 (2020).
365. Low, L. A., Mummery, C., Berridge, B. R., Austin, C. P. & Tagle, D. A. Organs-on-chips: into the next decade. *Nat. Rev. Drug Discov.* **20**, 345–361 (2021).
366. Vatine, G. D. *et al.* Human iPSC-Derived Blood-Brain Barrier Chips Enable Disease Modeling and Personalized Medicine Applications. *Cell Stem Cell* **24**, 995-1005.e6 (2019).
367. Rifès, P. *et al.* Modeling neural tube development by differentiation of human embryonic stem cells in a microfluidic WNT gradient. *Nat. Biotechnol.* **38**, 1265–1273 (2020).
368. le Feber, J., Postma, W., de Weerd, E., Weusthof, M. & Rutten, W. L. C. Barbed channels enhance unidirectional connectivity between neuronal networks cultured on multi electrode arrays. *Front. Neurosci.* **9**, 412 (2015).
369. Sarkar, A. *et al.* Efficient Generation of CA3 Neurons from Human Pluripotent Stem Cells Enables Modeling of Hippocampal Connectivity In Vitro. *Cell Stem Cell* **22**, 684-697.e9 (2018).
370. Karzbrun, E., Kshirsagar, A., Cohen, S. R., Hanna, J. H. & Reiner, O. Human brain organoids on a chip reveal the physics of folding. *Nat. Phys.* **14**, 515–522 (2018).
371. Shin, H. *et al.* 3D high-density microelectrode array with optical stimulation and drug delivery for investigating neural circuit dynamics. *Nat. Commun.* **12**, 492 (2021).
372. Trujillo, C. A. *et al.* Complex Oscillatory Waves Emerging from Cortical Organoids Model Early Human Brain Network Development. *Cell Stem Cell* **25**, 558-569.e7 (2019).

